NTNU – Trondheim
Norwegian University of
Science and Technology

Wake flow behind a curved cylinder

Tor Huse Knudsen

Marine Technology (2-year)
Submission date: June 2014
Supervisor: Håvard Holm, IMT
Co-supervisor: Bjørnar Pettersen, IMT
Tale Fjell Egeberg, MARINTEK

Norwegian University of Science and Technology
Department of Marine Technology

MASTER THESIS IN MARINE HYDRODYNAMICS

SPRING 2014

FOR

STUD. TECH. Tor Huse Knudsen

Wake flow behind a curved cylinder

Work description

The student is going to compare the flow around a curved circular cylinder as shown below, with the results from a DNS study. The student should use approved measurement techniques to get comparable data to the DNS study.

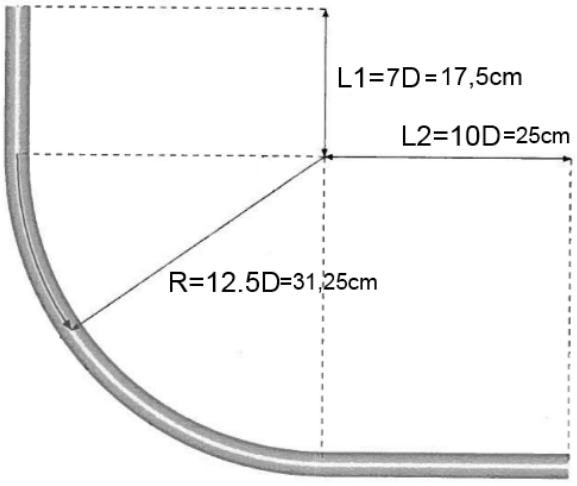

D=2,5cm

Scope of work

- Become familiar with the wake behind a cylinder
- Measure the velocity fields and velocity points in the wake behind the convex cylinder with reasonable non-intrusive methods
- Compare the velocity fields in the wake behind the convex cylinder with a previous DNS analysis and theory

The report shall be written in English and edited in the format of a report. It is supposed that Department of Marine Technology, NTNU, can use the results freely in its research work, unless otherwise agreed upon, by referring to the student's work. The thesis should be submitted 10.06.2014.

Co-supervisors: Professor Bjørnar Pettersen

Forsker Jan Hendrik Visscher

Sivilingeniør Tale Fjell Egeberg

Stipendiat José Gallardo

Førsteamanuensis Håvard Holm

Supervisor

1 Sammendrag

Denne masteroppgaven undersøker strømningen rundt en bøyd sirkulær sylinder ved et Reynoldstall på 3900 i vann ved hjelp av måleteknikken Particle Image Velocimetry (PIV) i en sirkulasjonsvanntank. Modellen som er brukt er en sirkulær sylinder som er bøyd i en kvartsirkel med en forlengelse i hver ende av kvartsirkelen. Innstrømningen er 90° på den ene forlengelsen av sylinderen, og den andre forlengelsen peker i samme retning som vannet strømmer. Gallardo et al (2014) [6] har gjennomført et numerisk eksperiment med Direct Numerical Simulation (DNS) med samme Reynoldstall, og et lignende modelloppsett. Resultatene i denne oppgaven stemmer kvalitativt godt overens med resultatene til Gallardo et al (2014) [6] når det gjelder gjennomsnittlig hastighetsfelt, hastighetsfluktuasjoner, Strouhalstall og virvlene i vaken. Resirkuleringslengden for PIV forsøket er lenger enn det Gallardo et al (2014) [6] har funnet, sannsynligvis på grunn av forskjeller mellom det numeriske oppsettet og det eksperimentelle oppsettet.

Laser Doppler Velocimetry (LDV) ble også brukt for å måle hastighetsfeltet bak sylinderen, men ga feilaktige resultat. Det er anbefalt å undersøke grensene for når LDV kan brukes med hensyn til nedre hastighet og retning.

2 Abstract

This thesis reports the result of an experiment measuring the wake flow behind a curved circular cylinder at Re=3900 in water. The measurement technique used was Particle Image Velocimetry (PIV). The cylinder is a convex configuration with a quarter of a ring with a straight elongation of the cylinder in each end. It was mounted with one of the elongations perpendicular to the incoming flow, and the other elongation pointing downstream. Many of the trends in the results of this thesis are in good agreement with the results by Gallardo et al (2014) [6], such as the velocity fluctuations, average flow fields and vortex dislocations. The recirculation length measured in this thesis was longer than the results by Gallardo et al (2014) [6], probably due to the difference between the numerical setup and the experimental setup.

Laser Doppler Velocimetry (LDV) measurements were also used, but gave inaccurate results. Further work will be to examine the measurement limits for the LDV in the Circulation Water Tunnel (CWT) with respect to direction and velocity magnitude.

3 Acknowledgement

I would like to thank my supervisor Håvard Holm, my co-supervisors Jan Hendrik Visscher, Tale Fjell Egeberg and José Gallardo. You have all inspired me and helped me discussing my results and the problems I have encountered. I would also like to thank HiB and NTNU department of Marine Technology for the opportunity to learn and educate myself in a very interesting scientific field. Although this thesis has at some points been frustrating, I have enjoyed the work of writing this thesis and conducting these experiments.

-Tor Huse Knudsen

Content

4 Nomenclature

PIV: Particle Image Velocimetry

SPIV: Stereoscopic Particle Image Velocimetry

LDV: Laser Doppler Velocimetry

DNS: Direct Numerical Simulation

v: $1{,}004*10^{-6}$ m^2/s

Re: Reynolds number $Re = \frac{U \times D}{\nu}$

St: Strouhal number $St = \frac{f \times D}{U}$

U_0: Incoming velocity of the flow. Also written U0

V: Velocity in y-direction

W: Velocity in z-direction

L: Length scale

D: Diameter of cylinder

f_{st}: Vortex shedding frequency

ω_z : Vorticity around the z-axis, also written omega-z

Reynold stress: Average of velocity fluctuations in y-direction times velocity fluctuations in x-direction. $\rho\overline{uv}$.

rms: Root-mean square values. The square root of the average of the velocity fluctuations squared. $\sqrt{\overline{u'^2}}$

ms: Mean-square values. Average velocity fluctuations squared $\overline{u'^2}$

ms: Unit, milliseconds

v': velocity fluctuations from the mean value V. This applies also for u' and w'

SNR: Signal to Noise Ratio

M_0: The lateral magnification

X, Y: For PIV, the coordinates on the image sensing element

x, y: For PIV, the coordinates on the light sheet

Z_0: For PIV, Distance from the lens to the image sensing element

z_0: For PIV, Distance from the lightsheet to the lens

f: For PIV, the focal length

d_p: The mean diameter of the particles

d_τ: Diameter of a particle on the image plane

d_s: Diffraction diameter

D_a: Diameter of the lens apparature

λ: For PIV and LDV, the wavelength of the light

d_a: Diameter of the abberated image of a point source

δ_z: Thickness of the focused plane

Δz_0: Thickness of the light sheet

N_s: Mean number of particles in a resolution cell

C: Mean number of particles per unit volume

D_I: Length scale of the interrogation window

F_i: In plane correlation factor

F_o: Out of plane correlation factor

A_I: Area of the interrogation window

c: The speed of light

f: For LDV, frequency

n: For LDV, refractive index

$\overrightarrow{r_d}$: For LDV, an unit vector along the observation axis

f_p: The frequency emitted by a tracer particle

CWT: The Circulation Water Tunnel at NTNU

X_b: The x value for the downstream cylinder wall at a given depth

5 Introduction

The flow around a circular cylinder is one of the fundamental fluid flow problems. Much research has been done and are being done on the topic, and new phenomena are being discovered. The flow around a curved circular cylinder can give valuable information even at low Reynolds numbers, as many effects for low Reynolds number flows can be seen for flows with high Reynolds numbers. The information can help in understanding and calculating of the forces on and the flow around other curved equipment important for the marine industry such as mooring lines, curved risers and pipelines.

The experimental setup in this thesis is shown in Figure 13 with a curved circular cylinder at Re=3900. The flow around a cylinder at Re around 3900 has been the subject to some research, and gives a good foundation for further research. This setup is similar to that of Gallardo et al (2014) [6]. The results in this thesis will be compared with Gallardo et al (2014) [6] and other relevant publications and articles.

Particle Image Velocimetry (PIV) is a measurement technique that samples the instantaneous velocity field, is non-intrusive, and gives a relatively large field of view. This makes PIV an effective experimental technique, not only for validation of numerical simulations such as Computational Fluid Dynamics (CFD), but also for independent experiments on the flow with a complexity surpassing the capacity of Direct Numerical Simulation (DNS).

6.1 Theory and literature review on the flow past a circular cylinder

6.1.1 Flow past a circular cylinder

A flow around a circular cylinder can be split in three parts, a boundary layer, a free shear layer and a wake behind the cylinder. Figure 1 and Figure 2 show an example of boundary layer, free shear layer and wake. Here δ means the boundary layer thickness, u means velocity inside the boundary layer and U_0 the flow speed outside the boundary layer.

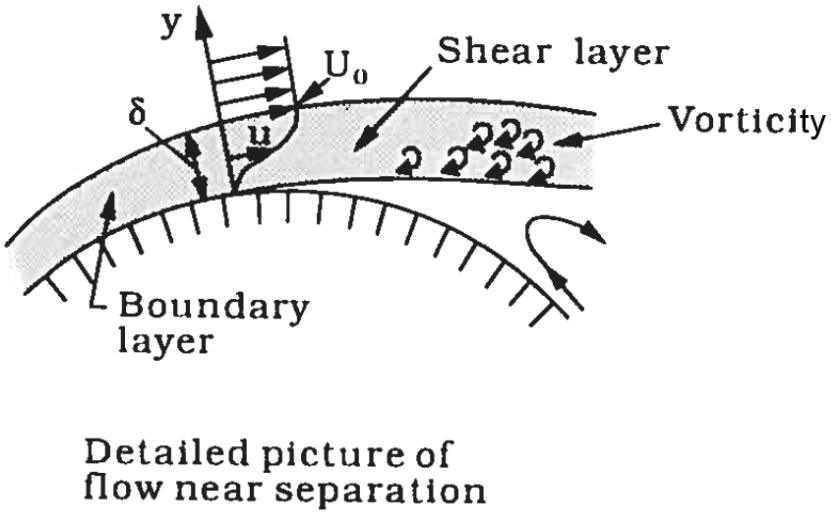

Figure 1: Boundary layer and structure of the flow near the cylinder. δ is the boundary layer thickness, u the velocity in the boundary layer, dependent of y, U_0 the incoming flow velocity. From Sumer and Fredsøe (1997) [17].

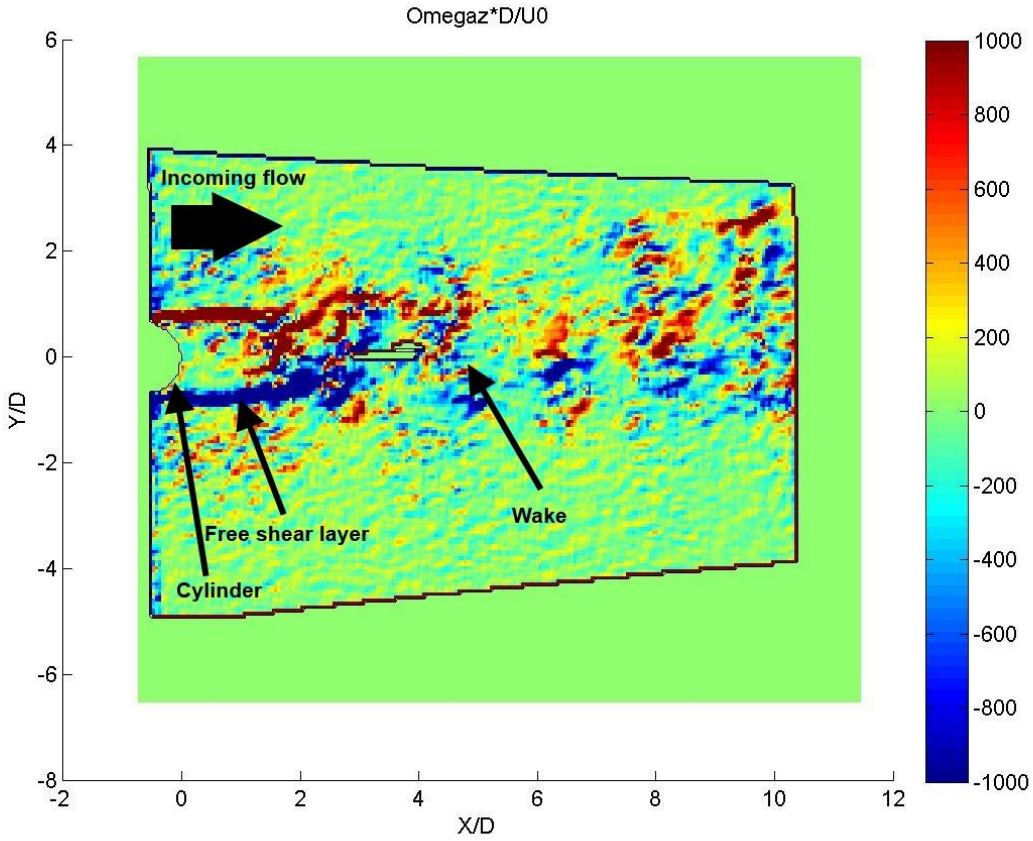

Figure 2: Instantaneous vorticity for a curved circular cylinder at Re=3900 and curvature of 12,5D at a depth of Z=10D after the start of curvature. The cylinder is marked with a black line. Red is positive values of vorticity and blue is negative values of vorticity. The flow is from left to right, and the free shear layer and wake are marked with arrows.

The first experimental observations of the periodic phenomena vortex shedding was done by Strouhal [16], and since then, the different physical aspects of flow around a cylinder has been studied in more detail.

There are many dimensionless numbers that can be of interest for a flow around a circular cylinder, but in this thesis Reynolds number (Re) and Strouhal number (St) are the most relevant, since vortex shedding and other flow phenomena on a circular cylinder are dependent on these dimensionless numbers.

Reynolds number (Re)

The Reynolds number is the ratio between inertia forces and viscous forces, and the vortex shedding is dependent on this number. For the case of the circular straight cylinder, the Re becomes

$$Re = \frac{U \times D}{\nu}$$

Here U is the free stream speed of the flow, D is the diameter of the cross section of the cylinder, and ν is the kinematic viscosity. For other flow configurations, the characteristic length scale replaces D. This may give a local Re at different locations of a curved circular cylinder.

This speed dependent dimensionless number is often used to characterize the flow in different categories, and different viscous flow phenomena such as turbulence and Strouhal number seems dependent on this dimensionless number.

Strouhal number (St)

The Strouhal number is the non-dimensional vortex shedding frequency and is defined as

$$St = \frac{f \times D}{U}$$

where f is the vortex shedding frequency.

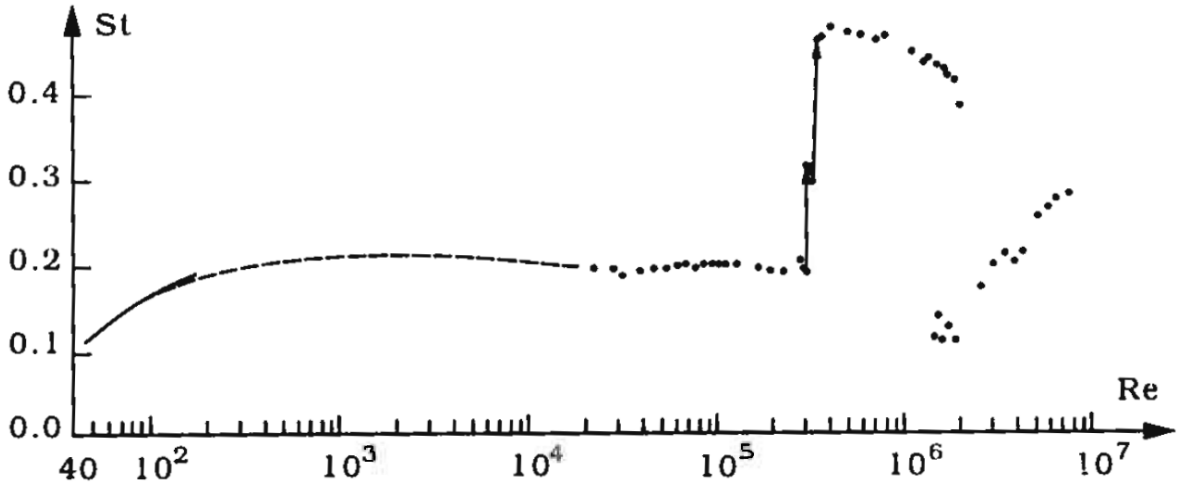

Figure 3: Strouhal number dependence of Reynolds number on a straight circular cylinder, from the book of Fredsøe and Sumer [17] page 10.

Figure 3 shows a graph over the development of the Strouhal number with increasing Reynolds number. Numerous experiments and articles has led up to this graph, for instance Roshko [15] who investigated this for Re=40 to Re=10 000.

6.1.2 Boundary layer

The boundary layer on a cylinder is the shear layer that exists on the surface of the cylinder before the separation point (see Figure 1). The friction between the cylinder surface and the flow is the driving force for the vorticity in the boundary layer, and the width of the boundary layer increases as the flow moves towards the separation point.

If Re is higher than $3{,}5*10^5$ transition to turbulence occurs in the boundary layer. Turbulence occurs first at the separation point, and moves towards the stagnation point as Re is further increased. The boundary layer is fully turbulent on one side of the cylinder at about $Re=1{,}5*10^6$, the side that is fully turbulent is alternating as the vortices shed, and fully turbulent at $Re=4{,}5*10^6$. As the boundary layers become turbulent on both sides, the separation is delayed, and the separation point moves towards the aft of the cylinder (see Figure 4). This leads to a jump in St from 0,21 to 0,45 [17] as shown in Figure 3. The pressure on the aft part of the cylinder increases, and the drag force decreases even though the viscous friction increases due to turbulence, as the separation point moves towards the aft of the cylinder [17]. The flow separates from the cylinder surface when the radial gradient of the tangential velocity is zero or

$$\frac{\partial u}{\partial y} = 0$$

Here *u* is the tangential velocity and *y* is in the radial direction. At the cylinder surface, the velocity is always zero due to the no-slip boundary condition. When the boundary layer becomes turbulent, the boundary layer thickness on the cylinder surface is reduced [11]. This may lead to a greater influence from the flow outside the boundary layer on the flow at the cylinder surface. This may again lead to the delayed separation of the flow. The increased mixing of momentum which is a property of turbulence, will also lead to a delayed separation of the flow, White [19].

An estimation of the turbulent boundary layer thickness along a flat plate from White (1991) [19] is $\frac{\delta}{x} = \frac{0{,}16}{Re_x^{1/7}}$. Here it is assumed that the boundary layer thickness (δ) is zero at the location the fluid starts to flow along the plate. *x* is the distance from the edge of the plate.

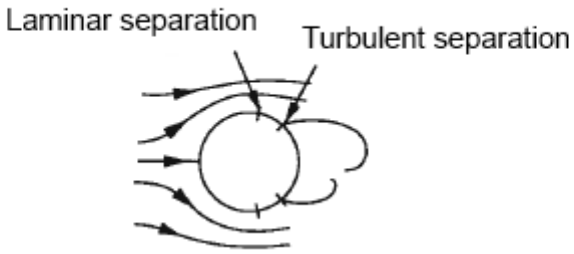

Figure 4: Turbulent and laminar separation point on a 2D cylinder, from the book of Fredsøe and Sumer [17] page 12.

Vorticity

Vorticity describe the rotation of the flow. In the flow past a bluff body, vorticity is generated from the boundary layer and is then fed into the wake. The vorticity tensor is defined as

$$\Omega_{ij} = \begin{bmatrix} 0 & \frac{1}{2}(\frac{dU}{dy} - \frac{dV}{dx}) & \frac{1}{2}(\frac{dU}{dz} - \frac{dW}{dx}) \\ \frac{1}{2}(\frac{dV}{dx} - \frac{dU}{dy}) & 0 & \frac{1}{2}(\frac{dV}{dz} - \frac{dW}{dy}) \\ \frac{1}{2}(\frac{dW}{dx} - \frac{dU}{dz}) & \frac{1}{2}(\frac{dW}{dy} - \frac{dV}{dz}) & 0 \end{bmatrix} = \frac{1}{2}\begin{bmatrix} 0 & \omega_z & \omega_y \\ -\omega_z & 0 & \omega_x \\ -\omega_y & -\omega_x & 0 \end{bmatrix}$$

This gives the vorticity vector $\overrightarrow{\omega_z}$

$$\overrightarrow{\omega_z} = \frac{dV}{dx} - \frac{dU}{dy}$$

Here ω_z is the vorticity around an axis in the z-direction, *U* and *V* is the velocity in x- and y-direction. Vorticity is a measurement of the rotation of the fluid.

6.1.3 Free shear layer

The free shear layer is the part of the flow extending from the separation point to the shedding of the vortices. This is a shear layer between the flow from outside the near wake and the retarded flow behind the cylinder. A vortex will increase its vorticity as it moves downstream, until the vortex from the other side of the cylinder has enough vorticity to cut off the new supply of vorticity bearing fluid Perry et al (1982) [11]. This is when the vortex is shed from the cylinder and it continues to travel downstream.

Dong et al (2006) [5] conducted simulations of a straight cylinder with DNS at Re=3900 and PIV experiments at Re=4000. In this study they came up with a free shear layer length of 1,65D for the simulation and 1,74D for the experiment. The definition of the end of the free shear layer was when the average vorticity was 8% of the maximum vorticity magnitude. The length was measured as shown in Figure 5.

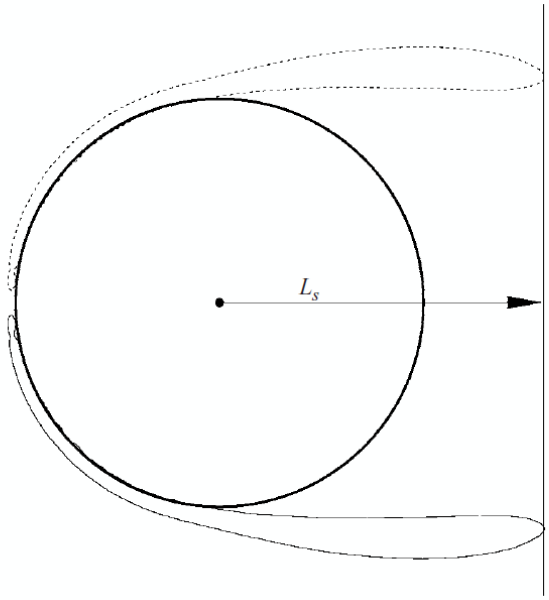

Figure 5: The definition length of the free shear layer, Dong et al (2006) [5]. The free shear layer length should be symmetric and the average vorticity field should be anti-symmetric. L_s is the effective shear layer length measured from the center of the cylinder cross section. The definition of the end of the free shear layer was when the average vorticity was 8% of the maximum vorticity magnitude. Taken at Re=4000.

6.1.4 Wake

The wake is the part of the flow affected by the cylinder that is downstream of the free shear layers. It is characterized by a vortex street convected downstream by the flow.

Anatol Roshko [15] studied the transition from laminar flow to turbulent flow in the wake of a cylinder. He found that the wake was laminar at 40<Re<150, the transition from laminar to turbulent was 150<Re<300, and for higher Re the wake was completely turbulent. Roshko also measured a periodic vortex shedding for very high Re in the wake of a circular cylinder.

6.1.5 Vortex dislocations

In the study on three dimensional structures in the wake of a circular cylinder Mansy et al [8] found vortex dislocations appearing over the whole span of the cylinder wake for a straight circular cylinder. Attempts were made to trigger the three dimensional structures by strips of tape with high surface roughness and tubes, but failed. The three dimensional effects were vortex-cells ending within the measured area, giving a dislocation in the vortex sheet. Vortex dislocations were also found behind a curved circular cylinder with a vertical extension by Gallardo et al (2014) [6] as seen in Figure 6. A discontinuity of the vortex cell is observed, and the vortices split. These vortex dislocations were not observed for a configuration without the vertical extension (Gallardo et al (2011) [7] and Miliou et al (2007) [9]). The vortex dislocations are associated with different St at the straight part of the cylinder and the curved part of the cylinder.

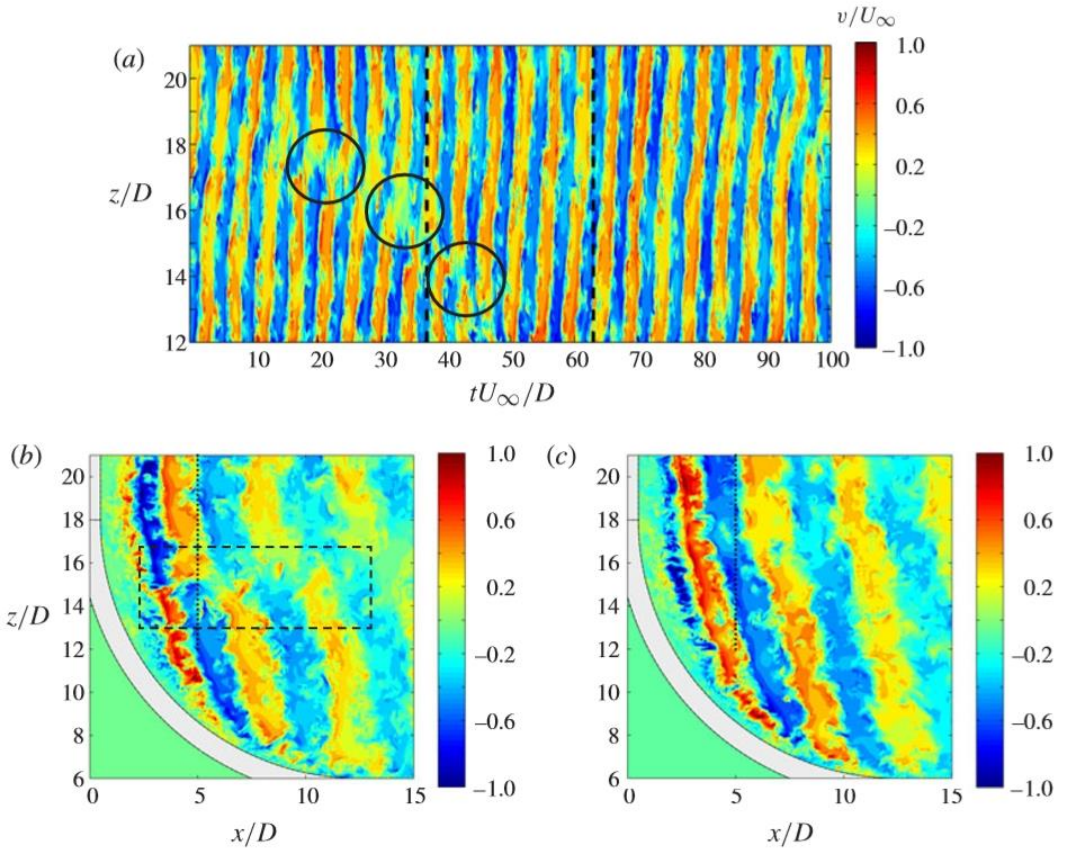

Figure 6: (a) Time evolution of the cross-stream velocity *v* along a vertical line located at the centreplane at y/D=0 and x/D=5. (b) Snapshot of the cross-stream velocity *v* at the centreplane depicting vortex splitting at $tU_\infty 7D = 37$. (c) Snapshot of the cross-stream velocity v at the centreplane at $tU_\infty 7D = 63$. Vortex splitting or vortex dislocations seen in (a) and (b). From Gallardo et al (2014) [6].

6.1.6 End conditions

The end conditions of the cylinder are an important aspect of an experiment on a circular cylinder in a flow. It is assumed that many experiments throughout the history have spreading in the measurements due to lack of control over the end conditions of the experiment. Prasad and Williamson (1997) [13] wrote a paper on how the end effects influence the wake vortex shedding patterns over a long span length. They also demonstrated that it is possible to induce parallel shedding, oblique shedding and vortex dislocations over a large range of Reynolds number. Parallel shedding is when the vortex is shed at the same time, and is transported downstream as a straight line parallel to the cylinder. Oblique vortex shedding is when the vortex is shed as a line not parallel to the cylinder, and not necessarily straight. If the endplates on each side were inclined in the same direction their experiments show that it induces an oblique vortex shedding over the whole span. They found that they could make the shedding angle up to 15 degrees with the right inclination of the end plates. Their experiments showed that even small inclinations of the endplates in the same direction can give oblique vortex shedding. They also found that parallel shedding can be induced by inclining the leading edge of both endplates inwards. The results were based on experiments on cylinders with a length of 40, 80 and 200 diameters.

6.1.7 Splitter plate

Bearman (1964) [3] conducted some experiments on blunt bodies fitted with splitter plates to examine the influence of splitter plates on the flow behind bluff bodies. A splitter plate is a plate attached to the aft of the cylinder parallel to the free stream direction. The Re range he used was $1{,}4*10^5$-$2{,}56*10^5$. It had long been known that splitter plates would reduce drag and sometimes suppress vortex shedding [3]. The hot wire technique was used to measure the flow. Another finding was that endplates reduced the three dimensionality of the flow. He found that the splitter plates reduced the three-dimensionality of the flow significantly and that it reduced the base pressure coefficient by half. It was also found that the endplates increased the base pressure coefficient marginally for the midsection of the body. The end plates did not influence the two dimensionality much if the splitter plates attached had a length of 1,5 D.

6.1.8 Inclined cylinder

S. E. Ramberg [14] wrote an article on the effects on yaw and finite length of a cylinder at $130<Re<1000$. He saw that the formation region of the vortices l_f measured in the free stream direction was increasing with increasing inclination angle at this Re range. He also looked into different end conditions, and concluded that the results were very sensitive to the end conditions, especially for the low Reynolds numbers.

In H.F. Wang's [18] article from 2010 they tested an inclined cylinder at 15, 30 and 45 degrees at a Reynolds number of 7 200. They saw that the intensity of the backflow downstream of the cylinder decreased as the inclination angle of the cylinder increased. The absolute value of the spanwise velocity increased behind the cylinder, with positive values in the middle of the wake, and negative values on the sides with increasing inclination angle. This trend was constant as the flow developed downstream. They also found that the peak in the power spectral density functions became broader for a cylinder inclined 45 degrees than for a cylinder without inclination, meaning a wider span of Strouhal frequencies. The root-mean-square values for these experiments changed as the inclination angles increased. In general, the rms of u decreased, the rms of v increased, and the rms of w decreased, to some extent.

6.1.9 Curved cylinder

Simulations using two curved cylinder configurations were carried out by Miliou et al (2007) [9] for Re=100 and Re=500 for a setup shown in Figure 7.

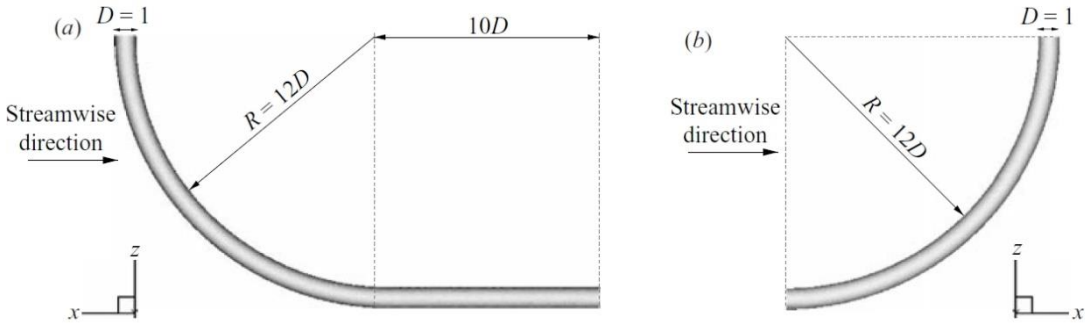

Figure 7: The setup used by Miliou et al (2007) [9]. (a) Definition of convex configuration; a ten diameter extension is included. (b) definition of a concave configuration.

They found that for a convex configuration, the vortex shedding from the upper part of the cylinder drove the rest of the vortex shedding for the curved cylinder at a dominant shedding frequency, even though the shedding frequency should be different due to the change of sectional Re along the cylinder span. In the case of concave configuration with the stagnation point on the inside of the curvature, no vortex shedding was detected.

Miliou et al (2007) [9] also found that an axial flow along the downstream side of the convex cylinder changed the flow conditions for the cylinder from bluff to slender at an inclination angle of around 60 degrees to the horizontal plane. This was for Re=100. An effect of this was less vigorous vortex shedding, although the shedding was synchronic with the upper part of the cylinder. A downstream flow at the stagnation face of the cylinder was also measured on the convex cylinder.

Gallardo et al (2014) [6] conducted a DNS simulation on a curved convex cylinder at Re=3900 in 2013. They extended the work by Miliou et al (2007) [9] toward turbulent water dynamics. Among the new features found was a small updraft close to the cylinder surface downstream of the cylinder. They also found vortex dislocations behind the cylinder. The primary vortex shedding was lost at the lower part of the cylinder, replaced by many tinier structures. The high amplitude fluctuations in the free shear layers were out of phase for the middle sections of the curved part of the cylinder in the simulation, and it is suggested that it is due to the axial secondary flows preventing interaction between the free shear layers. This is similar to the effects of what a splitter plate would give.

Another finding in Gallardo et al (2014) [6] was that the peak in the spectre showing the frequencies of the v component of the flow velocity (Figure 8) was higher as the measurement points were approaching the vertical part of the pipe, except at z/D=18. The Strouhal frequencies were slightly changing at different depth. There is also observed a peak at the third harmonic of the Strouhal frequency. This third harmonic is also observed in numerical studies for straight circular cylinders at Re=3900 by Parnaudeau et al (2008) [10].

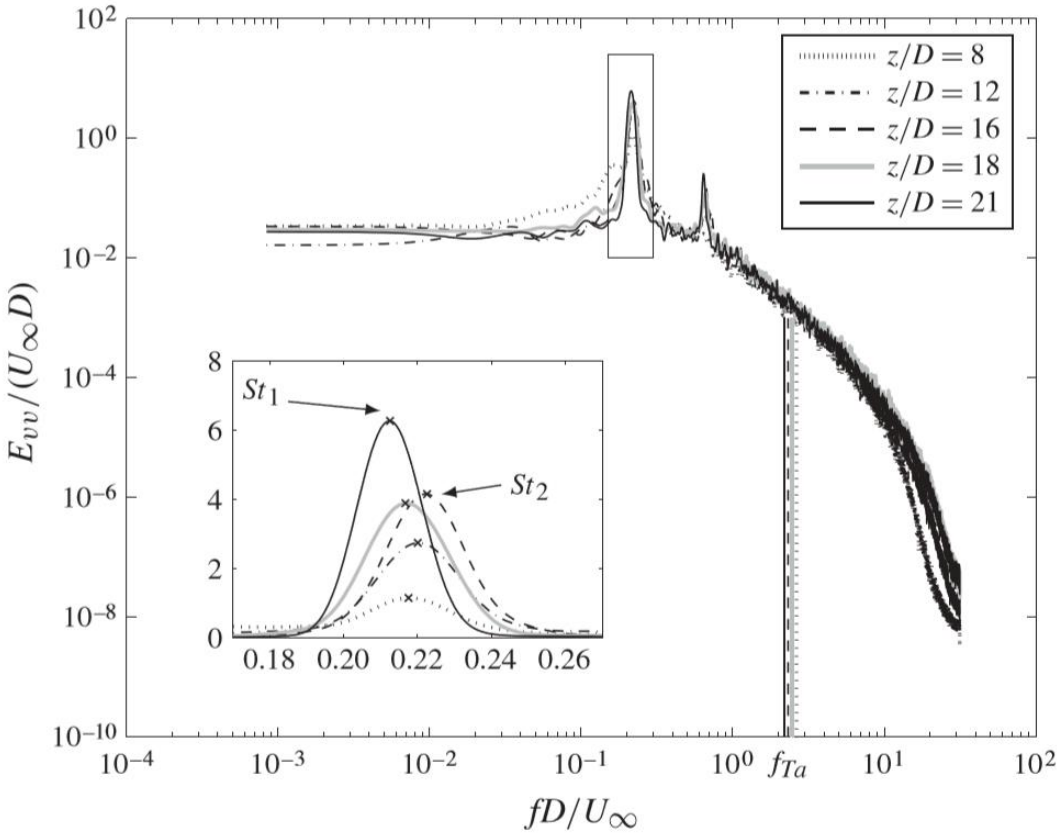

Figure 8: From Gallardo et al (2014) [6]. Frequency spectra at different depths 5D behind a curved circular cylinder based on the cross stream velocity *v*.

Gallardo et al (2014) [6] also examined the average velocity field behind the curved cylinder, the results are shown in Figure 9 and Figure 10. A light updraft was observed close to the cylinder surface in the upper part of the curved cylinder. A region with downdraft was observed by the lower part of the curved cylinder surface. The recirculation region behind the cylinder was also observed. This recirculation region decreased in strength as the lower part of the cylinder was approached, and vanished with a pointed end shape at around 9 diameter after the curvature of the cylinder started. The recirculation length, i.e. the length from the cylinder wall to where the mean streamwise velocity changes sign, was approximately 0,5D longer for the curved cylinder compared with a straight cylinder by Parnaudeau et al (2008) [10]. The recirculation region was preceded by a field with nearly zero mean velocity near the cylinder wall.

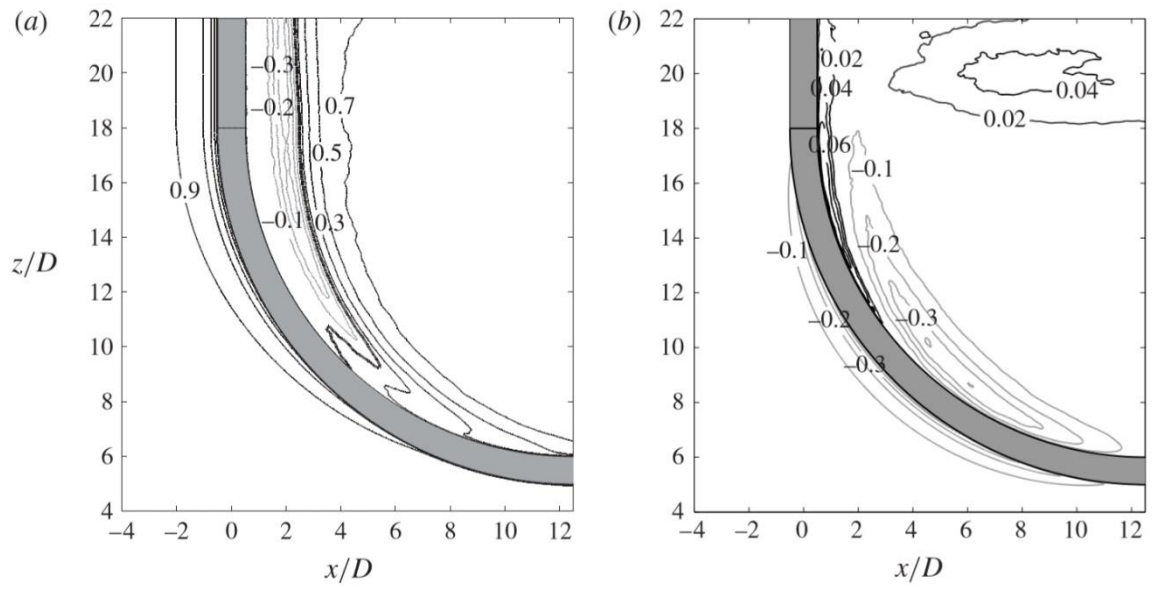

Figure 9: From Gallardo et al (2014) [6]. Mean velocity plots of the flow field in the centreplane behind a circular curved cylinder. (a) time averaged streamwise velocity U, where the thick line depicts the mean recirculation region. (b) time averaged vertical velocity W.

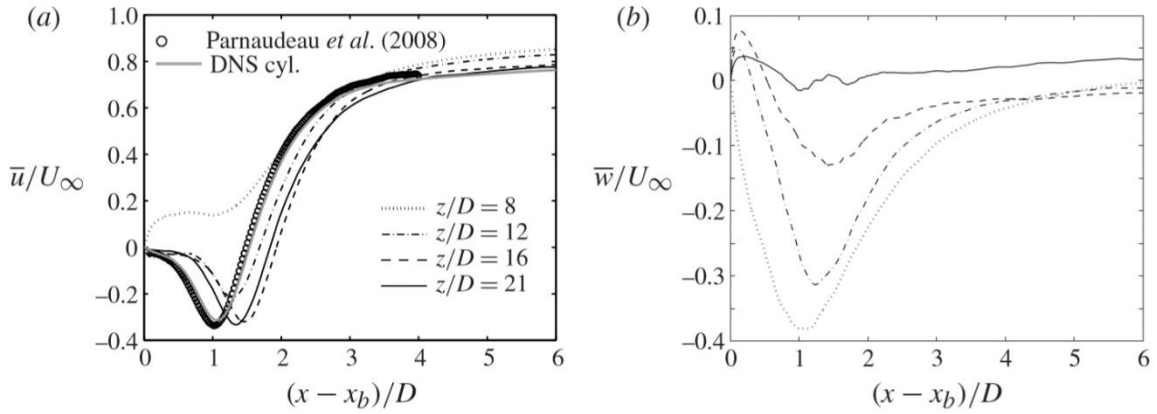

Figure 10: From Gallardo et al (2014) [6]. Lineplots of the average flow velocity behind a curved circular cylinder at different depths downstream of the cylinder. Compared to the results by Parnaudeau et al (2008) [10]. (a) Average streamwise velocity U downstream of the cylinder in the centreplane. (b) Average vertical velocity W downstream of the cylinder in the centreplane.

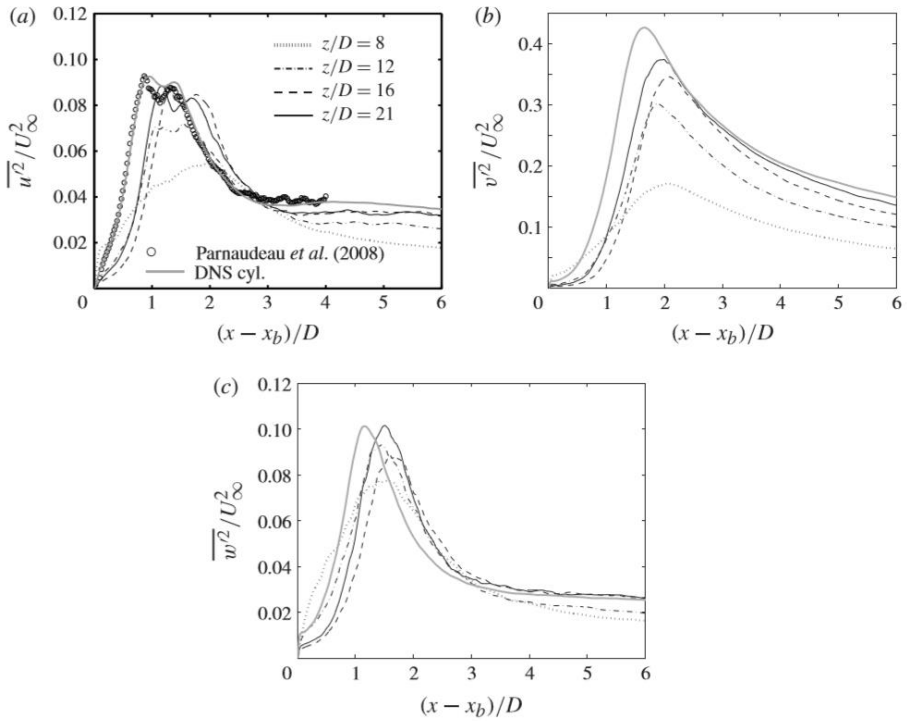

Figure 11: From Gallardo et al (2014) [6]. Mean square values of the centre plane in the wake downstream of a curved circular cylinder at z/D=8, z/D=12, z/D=16 and z/D=21. Compared to the results by Parnaudeau et al (2008) [10]. (a) Mean square values of the streamwise velocity fluctuations u'. (b) Mean square values of the cross-stream velocity fluctuations v'. (c) Mean square values of the vertical velocity fluctuations w'.

The mean square velocities behind the curved circular cylinder with a curvature radius of 12,5D were investigated by Gallardo et al (2014) [6]. The results are shown as in Gallardo et al (2014) [6] in Figure 11. For the streamwise velocity fluctuations a double peak was obtained which also was obtained by the experiment by Parnaudeau et al (2008) [10], and Gallardo et al (2011) [7], both on a straight circular cylinder. The first of the two peaks are displaced downstream compared with the straight cylinder, similar to the displacement of the average velocity profiles. This first peak of streamwise fluctuations define the vortex formation length. As the depth increases the $\overline{u}^2$ peaks decrease in intensity to $\sim 0{,}05 U_\infty^2$ at z/D=8. At this depth the mean square of the velocity fluctuations experience one broad peak only. The strength of the vortex shedding is depicted by the profiles of $\overline{v}^2$ in Figure 11. The velocity fluctuations in $\overline{v}^2$ are strongest on the midspan of the straight cylinder, although the maximum value of $\overline{v}^2$ are ~12% lower compared to the maximum value downstream of the straight circular cylinder obtained in Gallardo et al (2011) [7]. The maxima of $\overline{v}^2$ decrease slowly as the depth increases and at z/D=8 the maxima experiences a substantial decrease to ~0.17. This is less than half of the maxima at the straight part of the cylinder, and implies the suppression of both the vortex formation and the recirculation region. Despite the strong downdraft from the mean velocity profiles seen in Figure 10, the maxima of the $\overline{w}^2$ profile at z/D=8 are the lowest measured maxima. The highest peak is measured at the midspan of the straight cylinder, and is also the depth that give the smallest average w velocity. The peak was measured as $\sim 0.1 U/U_0$ which is the same magnitude as seen in the flow past a straight cylinder. This result shows that the level of fluctuations in vertical direction is related to the strength of the vortex shedding rather than the strength of the vertical velocity. The difference between the straight cylinder and the midspan of the straight part of the curved cylinder is a shift downstream of ~0,5D of the peak.

6.2 Theory behind the PIV and LDV measurements

PIV uses two pictures of illuminated particles that follow the flow to calculate a velocity field, while LDV uses the Doppler Effect from laser beams to calculate the velocity in a point. Both measurement techniques are non-intrusive. The information in the following chapter with subchapters except 6.2.10 are taken from [1].

6.2.1 Introducing parameters for PIV

The pictures are mapped through a lens onto an image plane according to

$$\begin{pmatrix} X \\ Y \end{pmatrix} = M_0 \begin{pmatrix} x \\ y \end{pmatrix}$$

Where x and y are the coordinates in the light sheet, X and Y are coordinates on the image-sensing element and M_0 is the lateral magnification.

$$M_0 = {Z_0}/{z_0}$$

Where z_0 is the object distance from the lightsheet to the lens and Z_0 is the image distance from the lens to the image sensing element.

The focal length is calculated from Gauss lens law

$$\frac{1}{Z_0} + \frac{1}{z_0} = \frac{1}{f}$$

Where f is then focal length.

The distance a particle has traveled between two pictures are approximated as a straight line. Then $(v_{px}, v_{py}) \cong \frac{(\Delta x_p, \Delta y_p)}{\Delta t} = \frac{(\Delta X_p, \Delta Y_p)}{M_0 \Delta t}$

and v_{px}, v_{py} are the speed of the particle in x- and y- direction. d_p is the mean diameter of the particles. The diameter of a particle on the image plane is calculated from

$$d_\tau \cong (M_0^2 d_p^2 + d_s^2 + d_a^2)^{1/2}$$

The diffraction diameter is d_s.

$$d_s = 2{,}44(1 + M_0) f^{\#} \lambda$$

$$f^{\#} = f/D_a$$

Where f is the f-number of the lens, D_a is the diameter of the lens apparature, λ is the wavelength of light and d_a is the diameter of the abberated image of a point source.

The depth of field of the image (focus) is given by

$$\delta z \cong 4\left(1 + \frac{1}{M_0}\right)^2 f^{\#^2} \lambda$$

Where δ_z is the thickness of the focused plane. $f^{\#}$ and M_0 is chosen properly so the focus thickness is greater than the light sheet thickness. $\delta z > \Delta z$

A map of the actual particle displacement will then be

$$\begin{pmatrix}\Delta X_p\\ \Delta Y_p\end{pmatrix} = M_0\begin{pmatrix}\Delta x_p\\ \Delta y_p\end{pmatrix} + M_0\begin{pmatrix}x_p/z_0\\ y_p/z_0\end{pmatrix}\Delta z_p$$

Where the $_p$ denote the particle position. If we approximate this solution for 2-D flow it appears as

$$\begin{pmatrix}\Delta X_p\\ \Delta Y_p\end{pmatrix} \cong M_0\begin{pmatrix}\Delta x_p\\ \Delta y_p\end{pmatrix}$$

The mean number of particles in a resolution cell is given by

$$N_S = C\Delta z_o \frac{\pi d_\tau^2}{4M_0^2}$$

Where C is the mean number of particles per unit volume.

If $N_S \ll 1$ the particles in the picture seldom overlap. This is the case for *low source density.*

A rough estimate of C is

$$C \cong \frac{m/\rho_p}{\frac{\pi}{6}d_p^3 V}$$

Where V is the total flow volume in the facility.

6.2.2 Uncertainty regarding the vector placement

The displacement vector is put to the center of each interrogation window, although the particle displacement may not have its center in this center. The rms difference between an arbitrary particle image and the vector placement are $\frac{D_I}{\sqrt{12}}$ where D_I is the length scale of the interrogation window. For N_I particle images in the interrogation window the rms difference are $\frac{D_I}{\sqrt{12N_I}}$. That means that the average error of the vector placement will be $\frac{1}{\sqrt{12N_I}}$.

6.2.3 Optimizing Δt and C (time interval between picture pairs and mean number of particles per unit volume)

The equation 8.88 provides the design rules for optimal conditions for a PIV measurement.

$$N_I > 10,\ |\Delta X| < \frac{1}{4}D_I,\ |\Delta z| < \frac{1}{4}\Delta z_0,\ M_0|\Delta \boldsymbol{u}|\Delta t < d_\tau \quad \text{eq.1}$$

Additionally the pixel resolution of a particle should be $2-4$ pixels. D_I is optimized during the interrogation, and the only variables left to adjust are then C and Δt. Δt is easily changed and well known, compared to C. To change C you will have to change the amount of particles in the water, and it may be difficult to withdraw particles from the water. C is also hard to define, but the earlier equation shows how it can be roughly estimated. One way to ensure you have the right amount of particles is to have a very small time delay, typically minimum. Add tracer particles while monitoring the valid detection rate. When the valid detection rate is near 100% there should be no further particles added to the fluid.

When the right amount of particles is added to the fluid the time delay should be increased stepwise towards the target value. This will lead to a loss of correlation and particle loss in-plane (F_I) and out-of-plane (F_O). If the number of data drops below an acceptable level, tracer particles should be added

to increase the number of valid data. With increasing time delay the computed velocity field will become smoother and with less noise and spurious vectors.

6.2.4 Loss of particles in plane and out of plane

If the two pictures are taken at the exactly same time, the particles will be in the same place in both pictures for all interrogation windows. But if the pictures are taken with a time delay, some particles will be lost, and some particles will be added due to the fluid motion. This makes the correlation between the two pictures more difficult, and invalid vectors may occur. F_I is the rate of particles not lost in-plane and F_O is the rate of particles not lost out-of-plane. F_I can be kept close to one and not less than 0,75 by having a larger second frame than first frame, but the F_O cannot be changed much unless you change the thickness of the laser sheet. The time delay should be taken so the average displacement in out of plane is less than a quarter of the light sheet thickness (eq.1) to avoid out of plane loss of correlation.

6.2.5 Calibration and mapping

It is important that a particle is mapped to the same point in physical space from the two different cameras in Stereographic PIV. This is done by calibrating the cameras with pictures of a target. The target has crosses at the same X and Y position at both sides and a thickness. This target is put into the fluid at the area you want to gather information and aligned with the laser sheet. Then the target is translated so that the visible plane for one camera is in the middle of the laser sheet. The camera is then focused on the target, both with the focus ring and a Scheimpflüg angle. The target is translated back in the middle of the laser sheet and a picture is taken. This should be repeated for both cameras. These pictures make it possible to map a particle in the physical space. The pictures are dewarped onto an image plane and compared. Two pictures taken at the exactly same instant from the two cameras are used to make a vector field by cross-correlation, this is called a disparity map. If the calibration is done perfect, there will be no trend in the disparity map, only random noise. A perfect calibration is very difficult to obtain, and small misalignments either in rotation or translation can have influence on the disparity map and the vector field from the experiment. By applying a disparity correction and subtract the eventual trend seen in the disparity map, the effects of the misalignment between the target and the laser sheet can nearly be eliminated.

6.2.6 Tank cleanliness and traces particles

The tank and the fluid should be clean before conducting a PIV experiment, both of other particles and algae. The algae production can be kept low by maintaining chemistry in the water so it will be inhabitable for algae. Algae in the fluid will lead to a background glow. Other particles may have a non-favorable size, form and reflecting properties. These should be filtered away before adding tracer particles.

When tracer particles are added a stirring device should be applied in the tank to avoid settling of the particles between the experiments.

6.2.7 Image pre-processing

Before processing the images into vector fields the images can be pre-processed to increase the quality of the images. The background of the particles may be bright, and this may cause bad correlation between the pictures. This may be eliminated in several different ways. One is to take a picture with no particles in the tank, and subtract this picture from the series of pictures, or to take an average over all the pictures and subtract this from the series of pictures.

Objects hit by the laser often end up as bright shapes in the image. This may influence the correlation greatly, and it is advised to zero out the gray levels of objects outside the flow, or pixels containing substantial wall flare. This may be done at the same time as the background removal.

6.2.8 Displacement interrogation

PIV use statistical methods to track groups of particles. The images are divided into interrogation windows, and are space-time cross correlated to see the displacement between the two pictures. The interrogation window in the second frame is larger and overlapping to ensure that the effect of in plane motion on the correlation is minimized. The dimension of the interrogation windows are often in a square: $A_I = D_{Ix} \times D_{Iy}$. The correlation plot of the field for a double frame, single pulse recording should have one high peak of correlation for the actual displacement of the particles. This peak is located at the coordinates of how much the first image should be shifted to overlap the second image. False correlation peaks will occur where particle images from different particles overlap. The correct correlation peak should be N times higher than the false ones, since nearly all particles will correlate, where N is the number of particles shared in both frames. Loss of particles in plane and out of plane will lead to a loss of correlation, as will addition of particles in and out of plane. This is the reason for a larger interrogation window for the second frame to minimize the loss of in-plane correlation.

6.2.9 Pixel locking

Pixel locking is when the displacement calculated in each interrogation cell is locked to the displacement of single pixels. This will result in a bias error between the measured velocity and the actual velocity. If the image of one particle only covers one pixel, or does not get any gray levels in adjacent pixels, the measured displacement of this particle will only be integers of pixels. This pixel locking can be avoided if there is many pixels in one interrogation window, so an average of these pixel displacement can be made.

6.2.10 Doppler effect

The information in this chapter are taken from [4]

When a wave is emitted from a moving source or observed by a moving observer a Doppler effect is experienced on the observed wave frequency. This effect will increase the frequency if the observer and source are getting closer, and decrease if the distance between the source and observer is increasing. This effect is used by the LDV to calculate flow velocities.

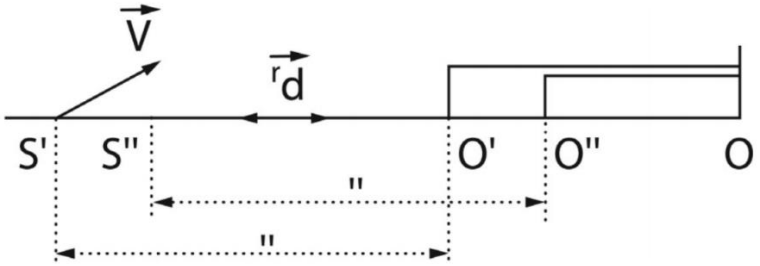

Figure 3.2. *Doppler effect: mobile source, fixed observer*

Figure 12: From Boutier et al (2012) [4]. S' is the particle at time instant t' and moves to S'' at instant t'+T_p, with $T_p=1/f_p$. f_p is the frequency emitted from the particle. The observer is located in O. O' and O'' are the position of the wave front for the wave emitted from the particle when it has its position at S' and S''. $\vec{V}$ is the velocity of the vector and $\vec{r}_d$ is a unit vector along the observation axis.

From observations on Figure 12 one can see that $\overline{S'O} = \frac{tc}{n}$ and $\overline{S'S''} = \vec{V}\vec{r_d}T_p$

where c is the speed of light, t is a time interval and n is the refraction index in the medium. A second peak emitted a time T_p later than S' is at O'' after the time interval t, then $\overline{S''O''} = \frac{(t-T_p)c}{n}$.

The wavelength observed is then O''O

$$\overline{O''O} = \overline{O''S''} + \overline{S''S'} + \overline{S'O} = T_p\left(cn^{-1} - \vec{V}\vec{r}_d\right) = f^{-1}cn^{-1}$$

The detected frequency is then

$$f = \frac{1 - \frac{\vec{V}\vec{r}_0 n}{c}}{1 - \frac{\vec{V}\vec{r}_d n}{c}}$$

Since V/c is very small even for extreme systems the expression can be simplified to

$$f = f_0\left\{1 - \frac{\vec{V}\cdot(\vec{r}_0 - \vec{r}_d)n}{c}\right\}$$

To use this to measure a velocity in a flow one can use laser beams reflected of particles in the flow. The fringe velocimeter technique uses two laser beams with a distinct propagation direction that cross inside the volume of measurement. These two laser beams are reflected with a different light frequency, f_1 and f_2. These two frequencies lead to another observed frequency

$$f_{D3} = |f(\vec{r}_1) - f(\vec{r}_2)| = \frac{|\vec{V}(\vec{r}_2 - \vec{r}_1)|n}{\lambda_0}$$

This can be used to calculate the speed in the flow.

7 Experimental setup

The experiments were conducted in the Circulating Water Tunnel (CWT) at NTNU Department of Marine Technology, and the model was designed by Tor Huse Knudsen and built by MARINTEK. The model was fixed to a frame to prevent vibrations and movement while installed. The cylinder was installed in two manners. One is shown in Figure 13 where the straight part of the cylinder is vertical, this setup was used for the centreline measurements and for the LDV measurements. The other setup was with the setup depicted in Figure 13 rotated 90° around the axis of the incoming flow, leading to the same configuration, but a different field of view. The downstream part of the cylinder was held fixed by steel rods fixed to the model frame. In some of the measurements these rods shadowed the laser, but never in the critical regions.

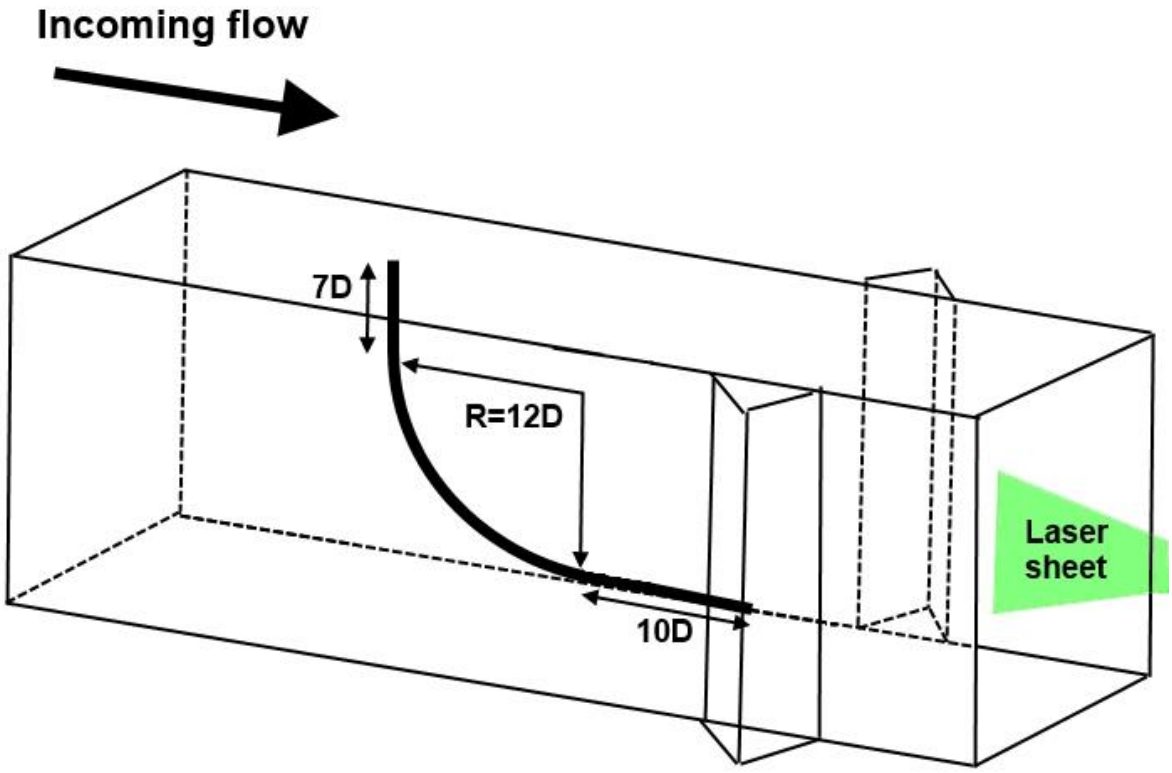

Figure 13: The experimental setup. The cameras are mounted one on each side. Pictures are taken through the prisms for the centreline measurements, and for the cross-section measurements one camera is mounted by a prism and one through the tank wall perpendicular to the flow direction. The LDV was mounted through the tank wall perpendicular to the wall.

The Re used was 3900, the diameter of the cylinder was 25mm and the free stream speed of the water was 0,1566 $^{m}/_{s}$. The free stream speed was measured by LDV. The coordinate system used is x in the free flow direction, z is vertical pointing upwards and y pointing to the left when facing in the free flow direction. There are some differences in this experimental setup and the setup used in Gallardo et al (2014) [6]. The length between the tank bottom and the lower part of the curved cylinder are 1D shorter in this experiment and the vertical extension in the upper part of the cylinder are 1D longer than for Gallardo et al (2014) [6]. This was done to increase the visible parts of the circular curved cylinder, and it is assumed that it has minor impact on the measurements. The upper and lower part of the control volume are free slip surfaces in Gallardo et al (2014) [6], and no slip surfaces in the PIV experiment. This may have an impact on the results due to boundary layers from

the tank surfaces. The size of the boundary layer length δ is approximately $\delta = 0{,}095m$ calculated from the approximate distance the water has traveled along the tank wall before the model appears.

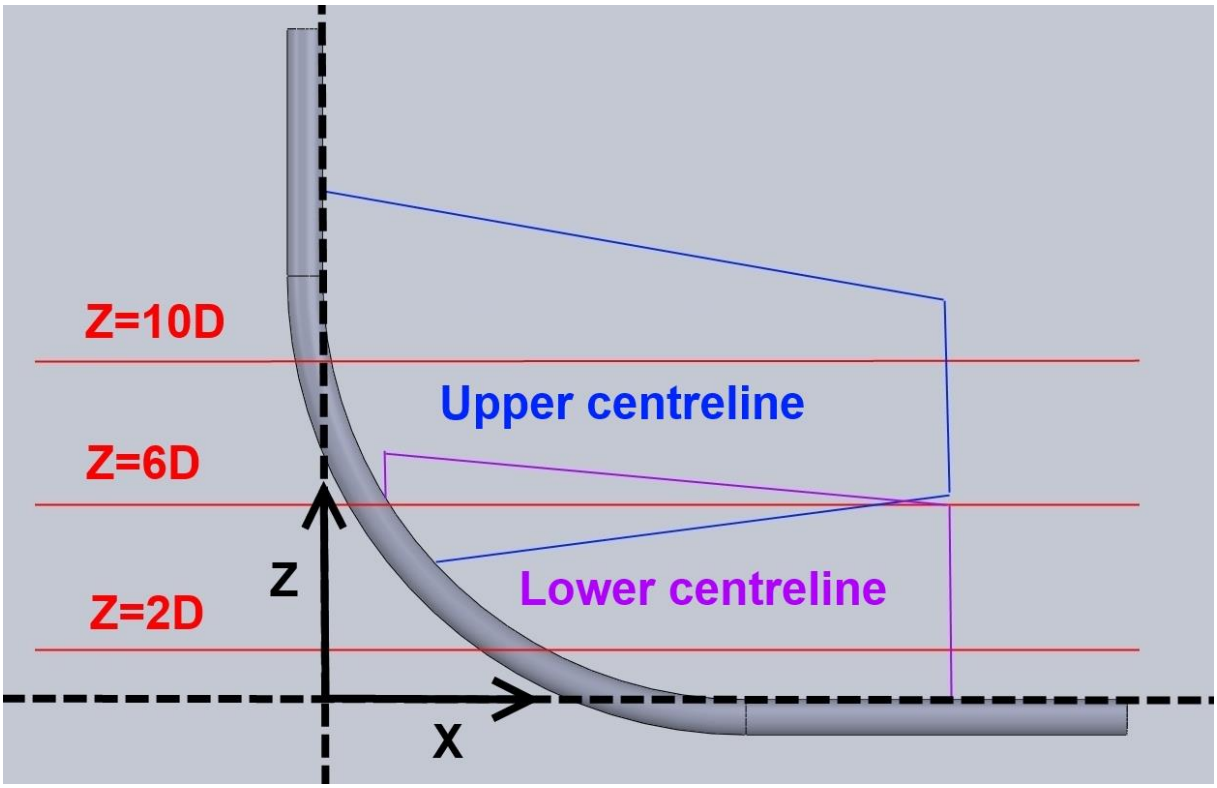

Figure 14: The five measurement regions for this experiment. Upper centreline plane, lower centreline plane, and in the x-y-plane at Z=2D, Z=6D and Z=10D.

The flow was measured in five different regions as shown in Figure 14. Two measurement regions were taken in the center plane downstream of the cylinder, and three cross-sectional measurements were made.

8 Results and discussion

In this chapter the results from the experiment conducted as a part of this thesis is going to be presented and discussed with relevant literature, in particular the numerical study by Gallardo et al (2014) [6]. The present experiment is in good qualitative agreement with the PIV experiment by Assi et al (2014) [2], even though the measurements by Assi et al (2014) [2] were taken 1D out of the centreline plane and at Re=1000. The sampling speed of the measurements were 11 samples per vortex shedding cycle, and the time window of the measurements were 90 vortex shedding cycles.

8.1 Free stream velocity

The free stream velocity was calculated from Re=3900 for this experiment as 0,1566$^{m}/_{s}$. The frequency of the engine of the circulation water tank were adjusted until the average LDV measurement over 120 seconds was at the correct speed. The engine frequency was recorded at the right flow velocity, and used for each run. A LDV measurement of the average flow speed was taken as a validation of the engine frequency for each run.

8.2 Layouts of the plots

The plots are separated into active measurement points and masked measurement points, where the masked measurement points always give the value zero. The masked and active measurement points are separated with a black line as seen in Figure 15.

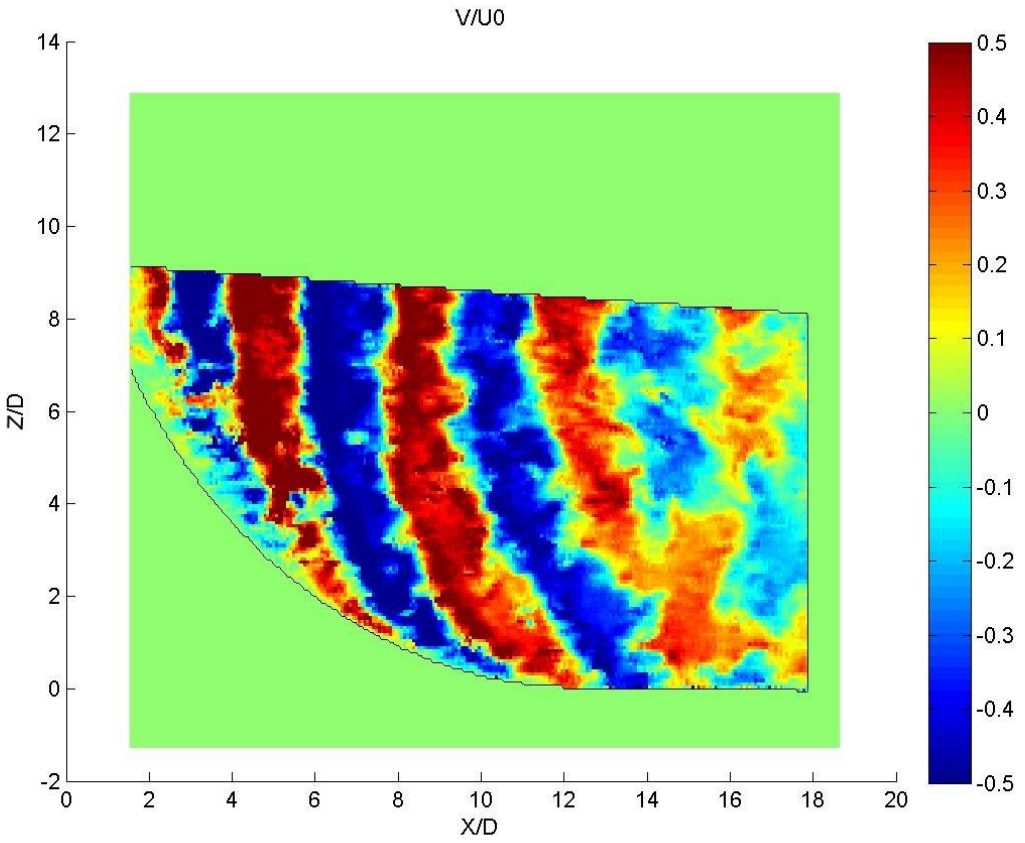

Figure 15: A typical plot of the instantaneous velocity field. The plots are divided into two parts, with and without data. These two parts are separated by a black line. The two boundaries of the part with data are the pipe and the borders of the pictures containing the PIV measurement.

The masked measurement points can be the boundaries of the field of view from both cameras, the pipe wall and invalid measurement points

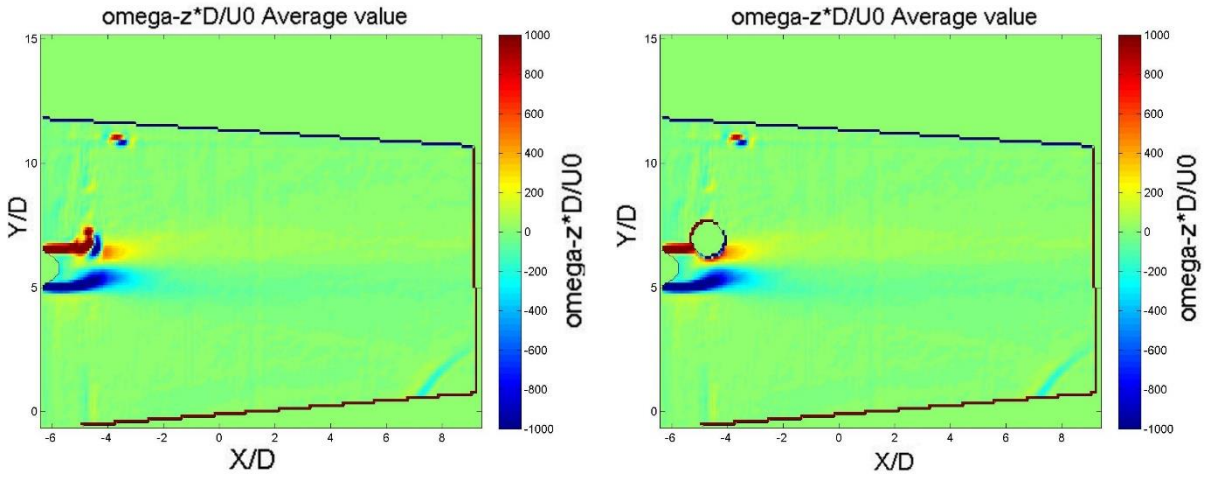

Figure 16: Left: Average vorticity at Z=2D. Right: Average vorticity at Z=2D with a masking of a spot in the free shear layer with much background light.

Figure 16 shows the average vorticity at Z=2D. The plot shows clear deviations of what is expected from such a flow field. These deviations are caused by the background of the pictures. If this background is bright, the particles in the bright spots will make a smaller contrast with the background. The background subtraction necessary to get a picture of only the particles will then make constant black spots. The black spots differ in strength, and in Figure 16 there are two strong black spots and several weaker lines. One spot is in the free shear layer, and is masked in the picture on the right hand side, the other is in the top part of the picture and is located outside of the wake. The weaker lines that we can see is one diagonal in the lower right corner, and two lines perpendicular to the incoming flow on the left hand side of the pictures. These lines give a small irregularity, but does not give much noise in the plot. The physical reason for the lines and the black spots are areas in the flow field were the cameras are unable to register the particles in the flow. Reasons for this may be that parts of the flow field are not illuminated by the laser sheet. There can also be rips, marks and damages on the transparent tank wall being illuminated by the diffracted laser light or other light sources. Algae emitting light, or equipment fitted on the tank wall or the model itself reflecting light from the diffracted laser light or other light sources can also be reasons for difficulties in registering illuminated particles. Another typical black spot for all the plots will be on and very close to the cylinder surface, since the model is reflecting light. The masked plots will be used in this thesis, the mask is plotted the same way as the boundaries of the flow.

8.3 Velocity profiles and fields

Figure 17 show the average value of U/U_0 in the centreplane behind the upper part of the curved cylinder. There is a recirculation region behind the cylinder that decreases in strength as one approaches the lower part of the cylinder. This is in agreement with Wang et al (2011) [18] for straight cylinders with increasing inclination angles. The local inclination angle of the curved cylinder cause a cross flow component on the cylinder equal to $U_n = Ucos(\theta)$ where θ is the local inclination angle. This gives a lower cross flow velocity as the depth increases. A minor cause for the decrease in strength of the recirculation region may be because the bluffness of the body is decreased as the inclination angle increases making the body appear more streamlined. A trend in the wake is that the average flow approaches the incoming flow as the flow continues downstream. This is in agreement with the numerical experiment of Gallardo et al (2014) [6], although the recirculation bubble comes ~0.4D farther downstream for the PIV experiment in the CWT, leading to a longer recirculation region. The reason for this may be the boundary layer from the tank wall interacting with the vertical extension of the cylinder, giving an oblique inflow velocity on the vertical extension. This may again influence the vortex shedding angle behind the curved cylinder that may be of importance for the velocity field. Figure 18 show the average value of U/U_0 in the centreline on the lower part of the curved cylinder. Here there is also a recirculation region present downstream of the cylinder. This recirculation region is slightly stronger and larger than for Figure 17 at the same places in the flow field. This is probably due to a slight misalignment of the laser sheet compared to the centreplane in Figure 17, especially in the lower areas of the plot. This leads to an average measurement of the recirculation region that is slightly weaker where the laser sheet and the centreplane is not totally coinciding (more under error sources). The contours near the recirculation region in Figure 18 also have a characteristic double spike as the recirculation region breaks down at around 9D below the start of curvature on the cylinder. This is in good agreement with the numerical experiments by Gallardo et al (2014) [6]. Figure 19 shows a line plot of the mean velocity at Z=8D. It shows that the recirculation bubble has a smaller amplitude, and that the bubble has its peak at around 0,4D downstream of the location obtained by Gallardo et al (2014) [6]. The velocity in x-direction in the experimental results has an increase of the velocity gradient downstream of X/D=10, and this implies that the measurements downstream of X/D=10 are inaccurate.

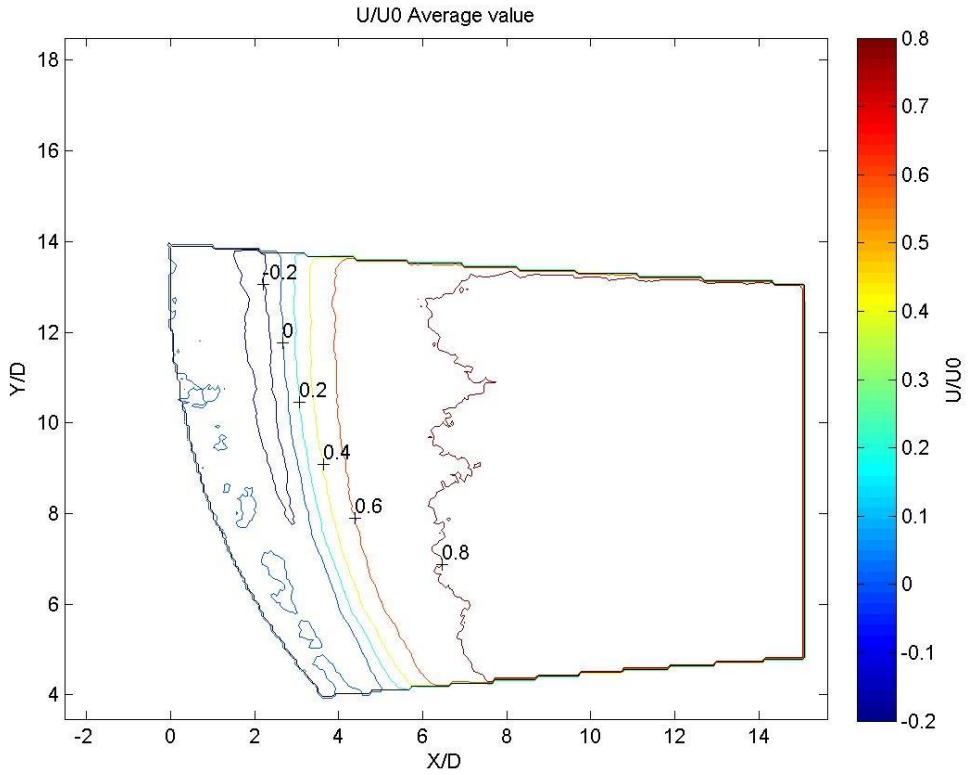

Figure 17: Average value U/U0 at the centreline on the upper part of the cylinder.

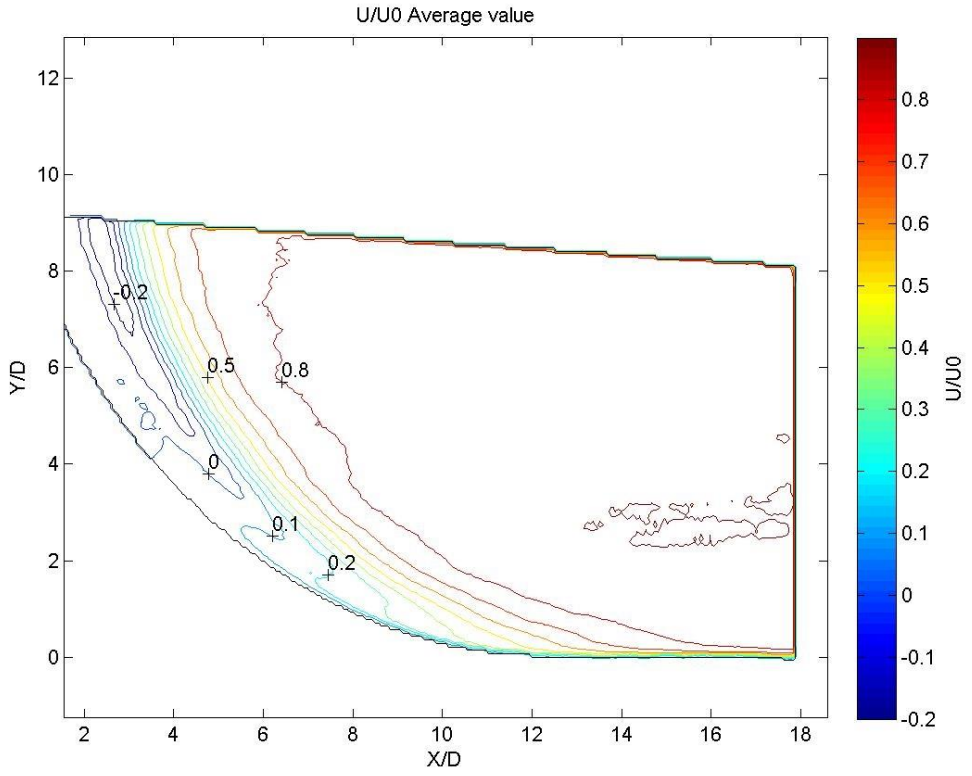

Figure 18: U/U0 average value in the center plane at the lower part of the cylinder.

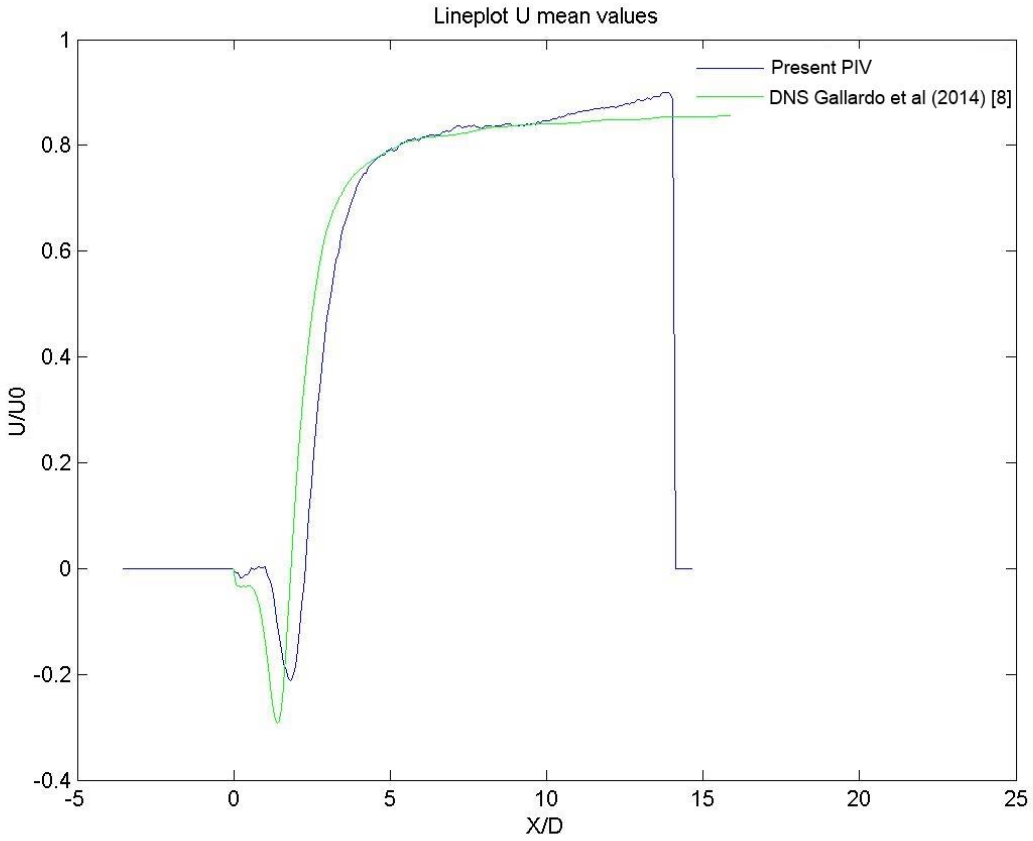

Figure 19: Comparison between the experiment by Tor (2014) and Gallardo et al (2014) [6]. Line-plot of U velocity at Z=8D.

In Figure 20 and Figure 21 the average value of W/U_0 are plotted on the wake of the upper part of the cylinder. From 1D after curvature to around 7D after curvature, a small updraft is measured close to the curved cylinder surface. This updraft has a small amplitude and covers a small region. Gallardo et al (2014) [6] also found this updraft in his numerical experiments, but over a slightly larger area and with a larger amplitude. The measured values and area of updraft may be smaller than the real values due to the reflection of laser light at the cylinder surface, the size of the interrogation windows and misalignment of the laser sheet. An area of downdraft is located downstream of the cylinder surface. This downdraft is located over the whole span of the cylinder and is of much larger amplitude than the updraft. As the cylinder wake proceeds downstream the velocity in z-direction approaches zero. In Figure 22 one can see that the amplitude of the updraft is much higher for the numerical results than for the experimental results. The peak in downdraft for the experiments are slightly larger and has its peak around 0,4D downstream of the locations obtained by Gallardo et al (2014) [6].

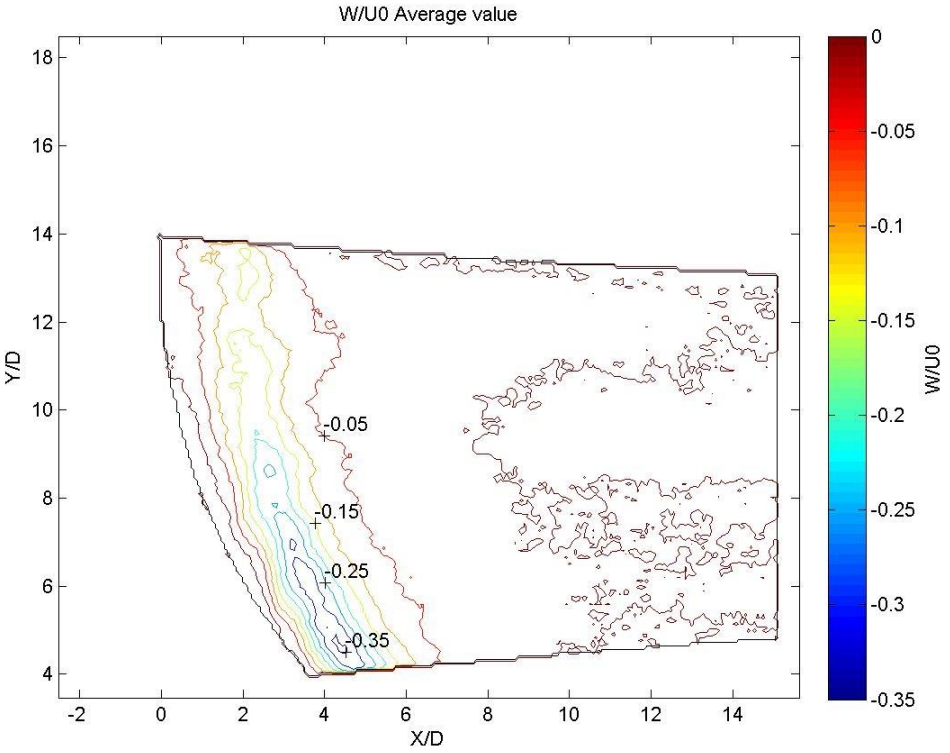

Figure 20: Average value of W/U0 at the centreline on the upper part of the cylinder.

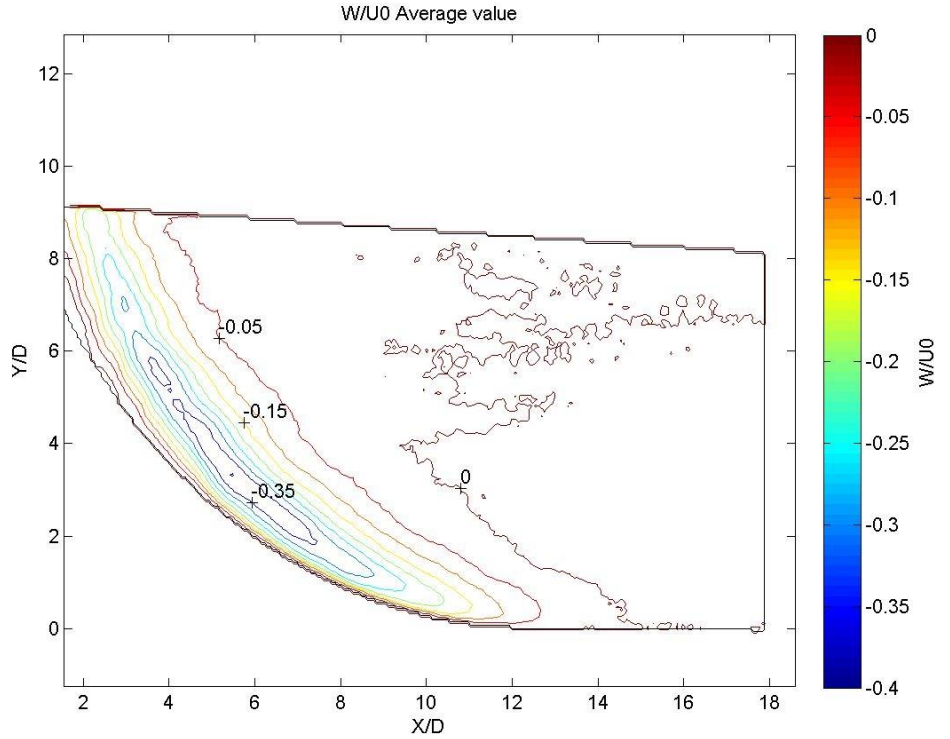

Figure 21: W/U0 at the centreline at the lower part of the cylinder.

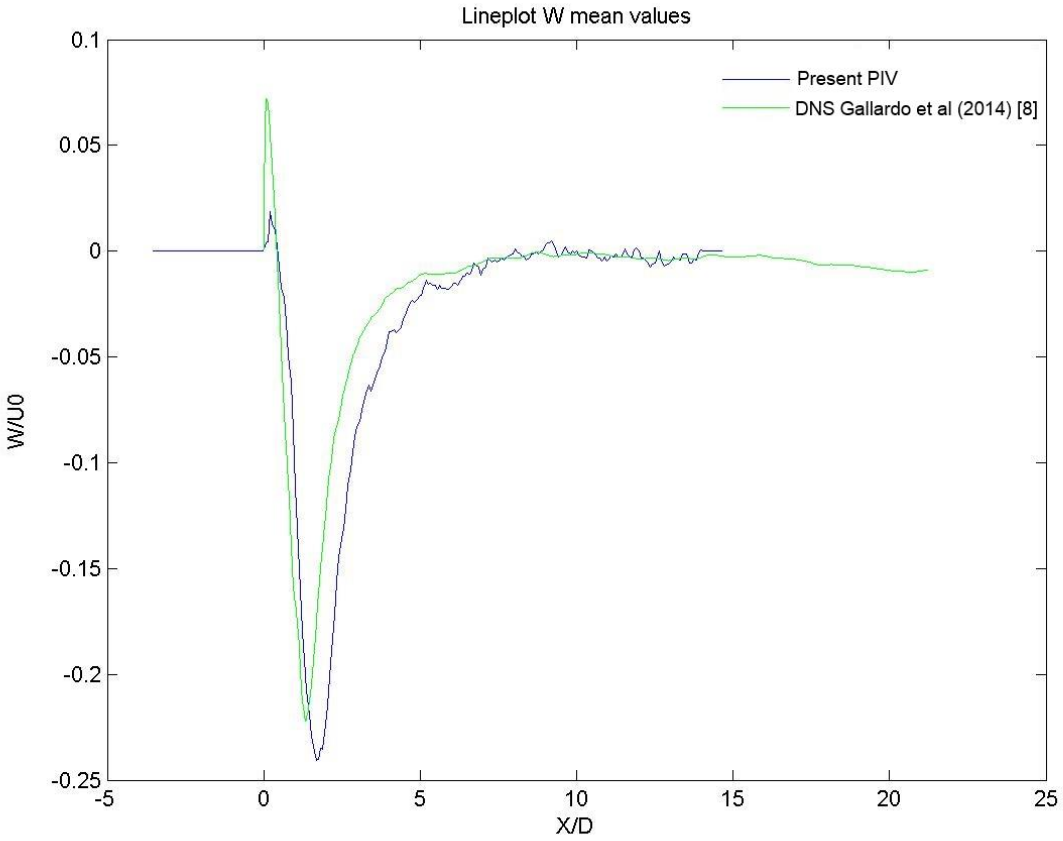

Figure 22: Comparison between the experiment by Tor (2014) and Gallardo et al (2014) [6]. Lineplot of W velocity at 4D after curvature.

8.4 Velocity fluctuations

Figure 23, Figure 27 and Figure 31 are graphs over the mean square values of the velocity fluctuations at Z=10D, Z=6D and Z=2D. The mean square values have their maxima a distance downstream from the cylinder wall around where the vortex shedding takes place, and decreases downstream of this maxima. Close to the cylinder surface the gradient of the velocity fluctuations are slightly increasing with increasing depth. A reason for this may be a smaller and suppressed recirculation region and vortex shedding. This is in good agreement with the results of Gallardo et al (2014) [6]. The distance traveled by a particle over a timestep is approximated as a straight line with constant speed. The PIV measurements were sampled ~ 11 times per vortex shedding cycle where each sample is an average velocity over a timestep of 5ms. Gallardo et al (2014) [6] used 240 non-averaged samples per vortex shedding cycle. The resolution of the PIV in time and space may have difficulties catching the turbulent fluctuations in the wake, leading to lower values of the velocity fluctuations.

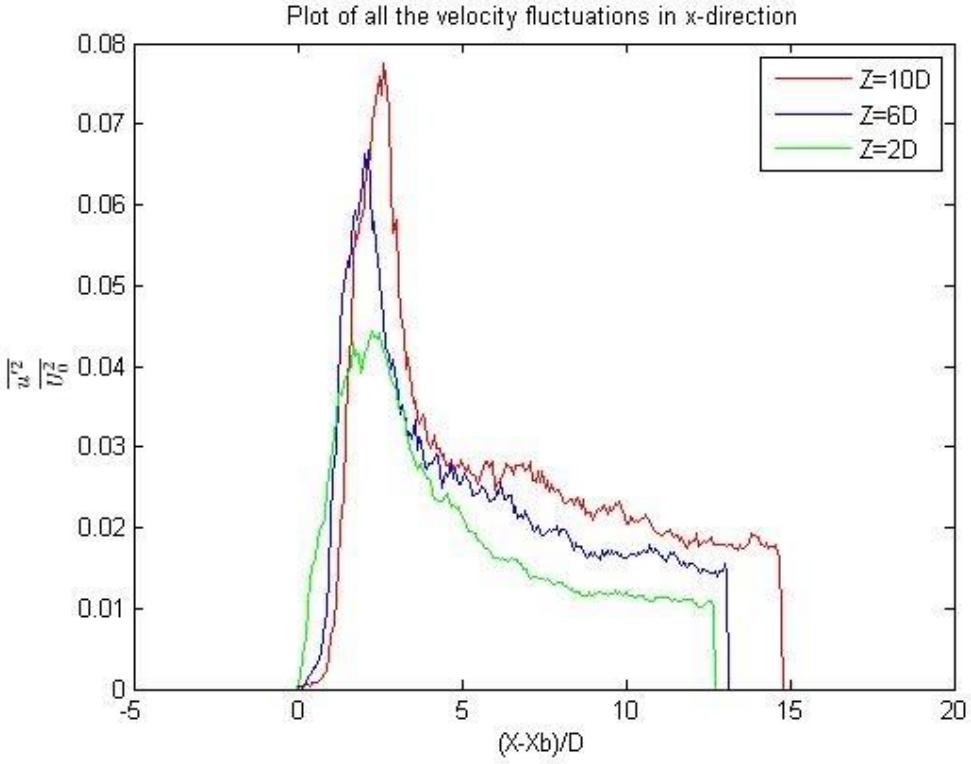

Figure 23: The mean square values of the velocity fluctuations in x-direction for Z=10D, Z=6D and Z=2D. u' represent the velocity fluctuations.

The mean square values of the U velocity have a lower amplitude as the depth increases. The decrease in amplitude may come from a suppression of the recirculation region and vortex shedding, leading to weaker velocity fluctuations. It may also come from an inclining of the vortex shedding axis giving smaller fluctuations due to vortex shedding on the U velocity, and greater fluctuations due to vortex shedding on the W velocity. A reason for the slight increase in gradient close to the cylinder

surface may be due to a weaker or non-existing recirculation region behind the cylinder, and that the cylinder is transferring from a bluff body to a streamlined body as the inclination angle increases.

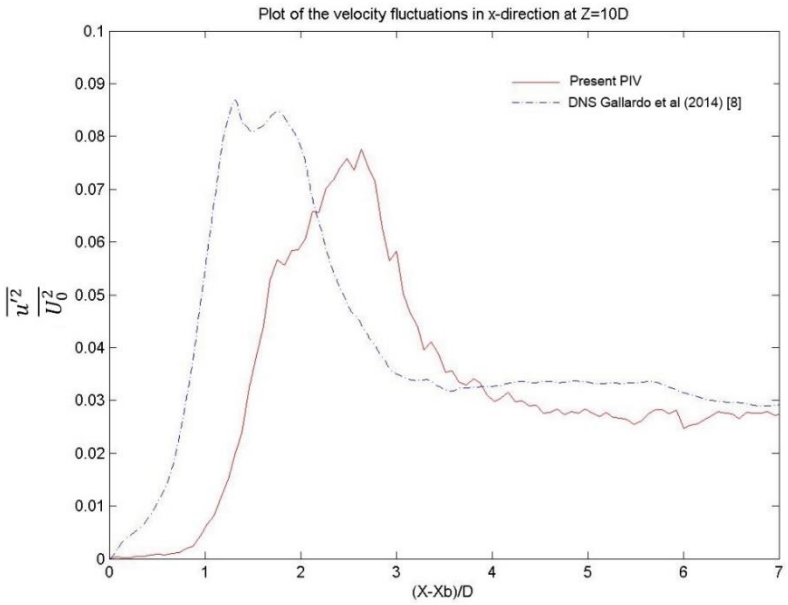

Figure 24: Lineplot of the mean square of the velocity fluctuations in x-direction at the centreline at Z=10D. The measurements are compared with data from Gallardo et al (2014) [6] with similar flow conditions. u' represent the velocity fluctuations.

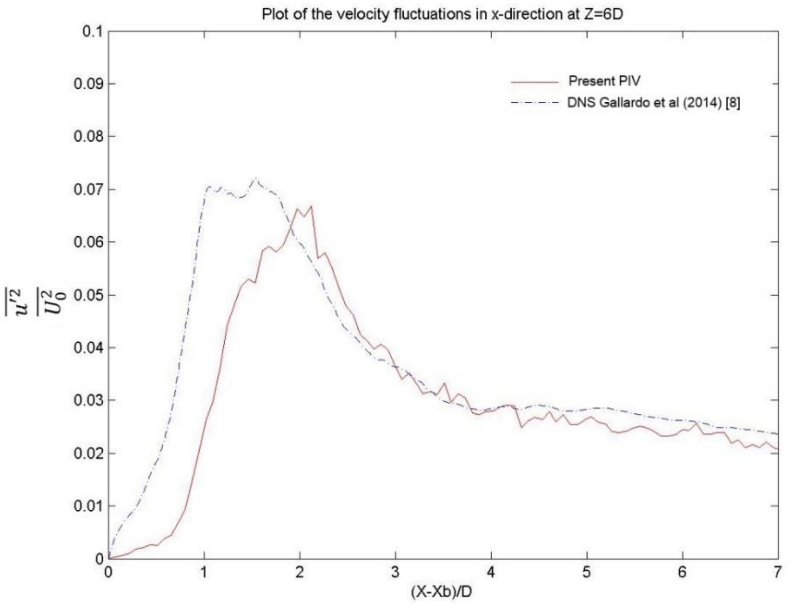

Figure 25: Lineplot of the mean square of the velocity fluctuations in x-direction at the centreline at Z=6D. The measurements are compared with data from Gallardo et al (2014) [6] with similar flow conditions. u' represent the velocity fluctuations.

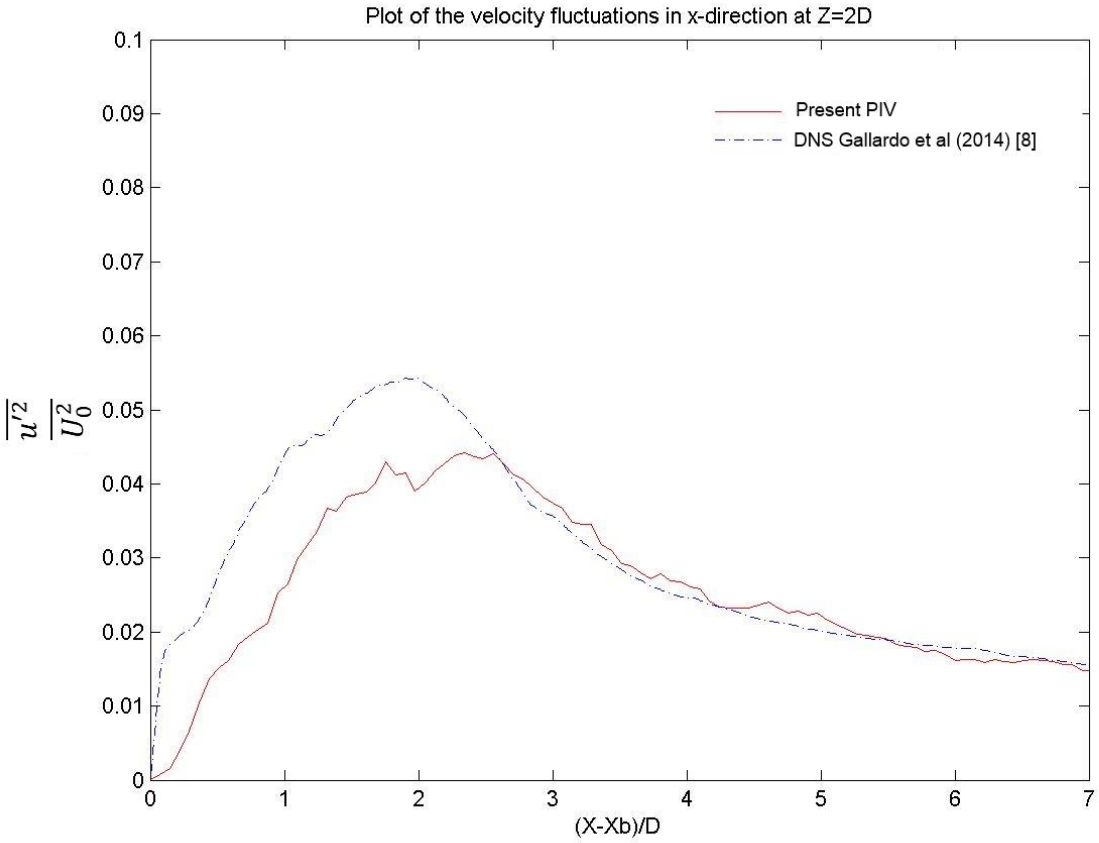

Figure 26: Lineplot of the mean square of the velocity fluctuations in x-direction at the centreline at Z=2D. The measurements are compared with data from Gallardo et al (2014) [6] with similar flow conditions. u' represent the velocity fluctuations.

From Figure 24, Figure 25 and Figure 26 it is evident that the peak of the squared velocity fluctuations from the PIV experiment are translated $\sim 0{,}5D$ downstream compared to the DNS analysis done by Gallardo et al (2014) [6]. Although the peaks have about the same width and similar trends, the double-peak seen in Figure 24 and Figure 25 for the numerical study by Gallardo et al (2014) [6] are not evident in the measurements done with PIV. The peaks of the square of the velocity fluctuations are also slightly lower for the PIV measurements compared to the Numerical studies in Figure 24, Figure 25 and Figure 26. This may come from the time and spatial resolution of the PIV measurements.

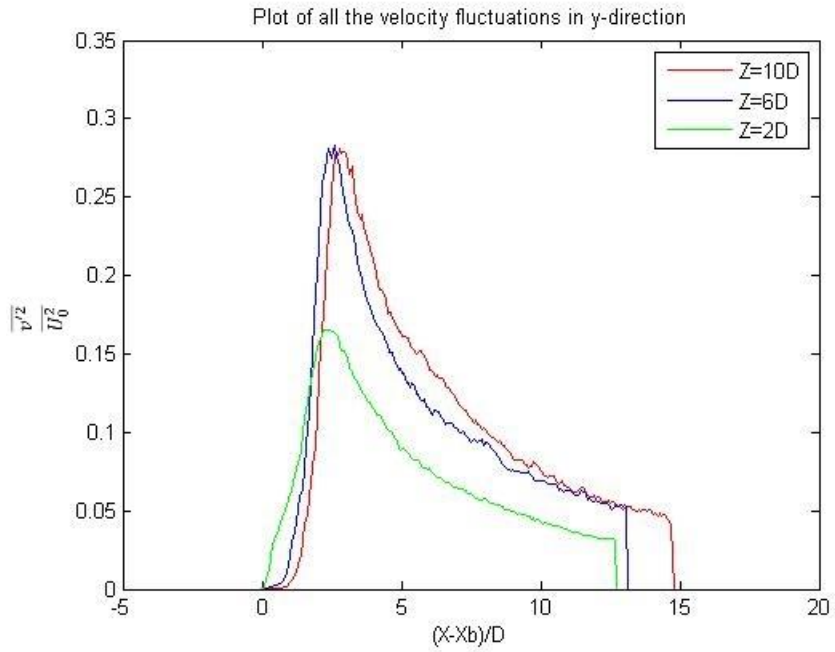

Figure 27: The mean square values of the velocity fluctuations in y-direction downstream of the cylinder for Z=10D, Z=6D and Z=2D. v' represent the velocity fluctuations.

The mean square values of the velocity fluctuations on the V velocity (Figure 27) show a significant drop in amplitude of maxima at Z=2D. A reason for this may be a loss in periodicity, a suppression of the vortex formation and recirculation region of the flow at Z=2D compared to Z=6D and Z=10D. The maxima of the $\bar{v}^2$ plots for Z=10D and Z=6D are also of the same magnitude. This suggests that the amplitude of the instantaneous V velocity exceededs the limit for the detectable velocity out of plane of the PIV experiment. The reason for this limit is the laser sheet thickness. The particle must travel a distance less than the laser sheet thickness in the time step between the frames in a picture pair. If the flow speed exceeds this limit, no particles will appear on both frames of the picture pairs, and no velocity can be calculated. The velocity vectors are then interpolated from the neighbouring vectors giving the same magnitude as the maximum velocity that is measurable. The peak of the mean square of the velocity fluctuations are closer to the cylinder surface as the depth increases. This is also in agreement with Gallardo et al (2014) [6].

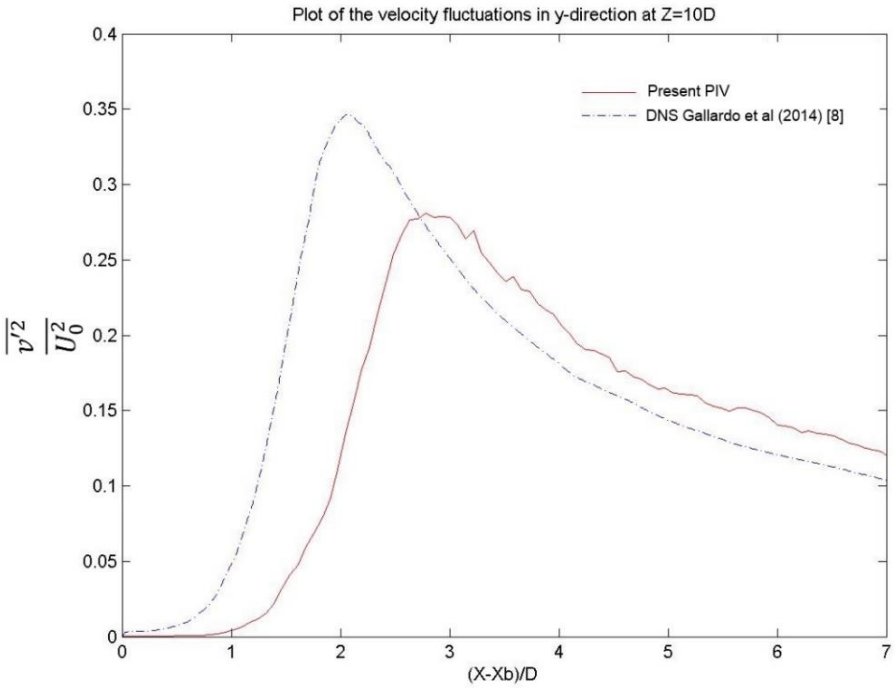

Figure 28: Lineplot of the mean square of the velocity fluctuations in y-direction at the centreline downstream of the cylinder at Z=10D. The measurements are compared with data from Gallardo et al (2014) [6] with similar flow conditions. v' represent the velocity fluctuations.

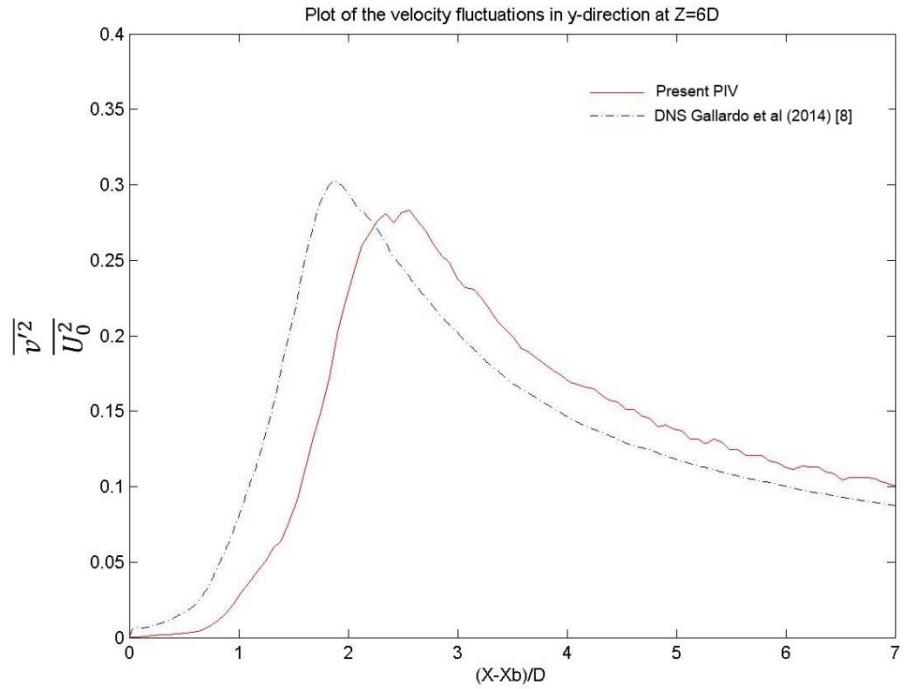

Figure 29: Lineplot of the mean square of the velocity fluctuations in y-direction downstream of the cylinder at the centreline at Z=6D. The measurements are compared with data from Gallardo et al (2014) [6] with similar flow conditions. v' represent the velocity fluctuations.

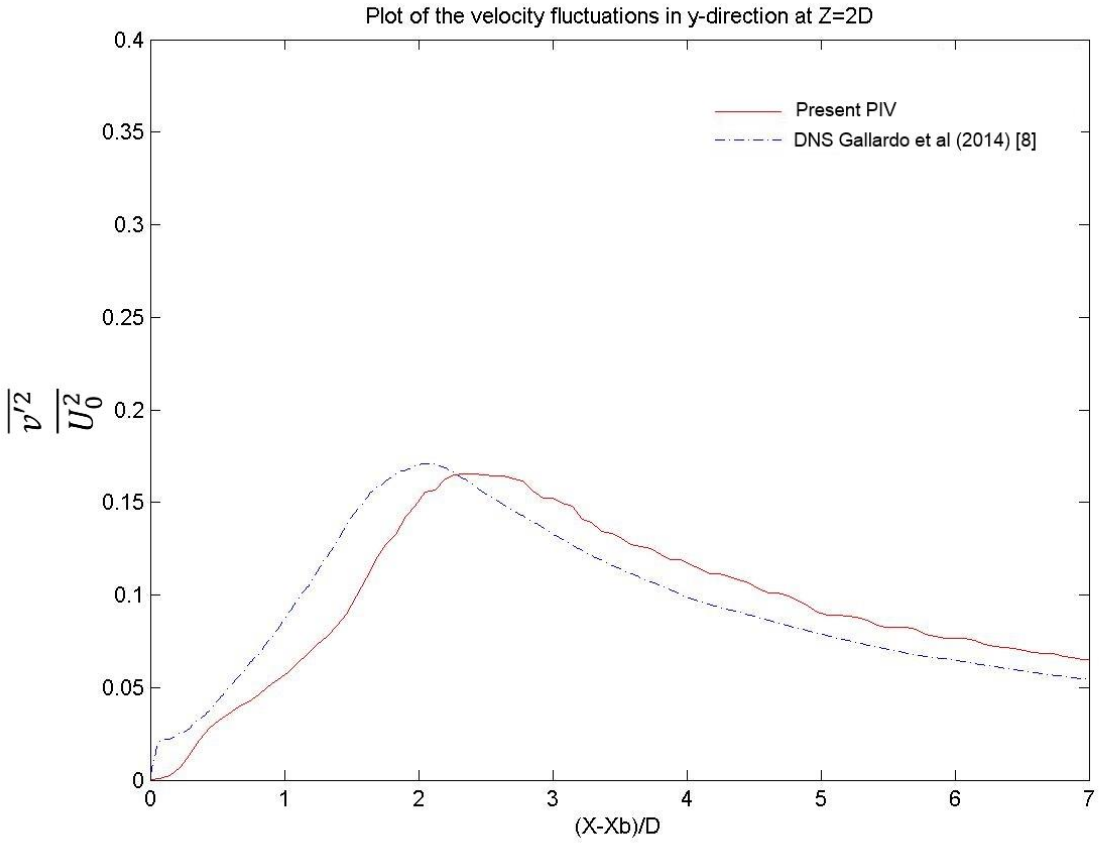

Figure 30: Lineplot of the mean square of the velocity fluctuations in y-direction at the centreline downstream of the cylinder at Z=2D. The measurements are compared with data from Gallardo et al (2014) [6] with similar flow conditions. v' represent the velocity fluctuations.

The maxima of $\bar{v}^2$ at Z=10D were lower compared to Gallardo et al (2014) [6]. The magnitude of the maxima for Z=2D and Z=6D are in good agreement with the numerical experiment by Gallardo et al (2014) [6], and the same trends can be seen in the plots for the experimental and numerical study. The peak of the mean square values for PIV are downstream of the numerical results from Gallardo et al (2014) [6] for Figure 28, Figure 29 and Figure 30.

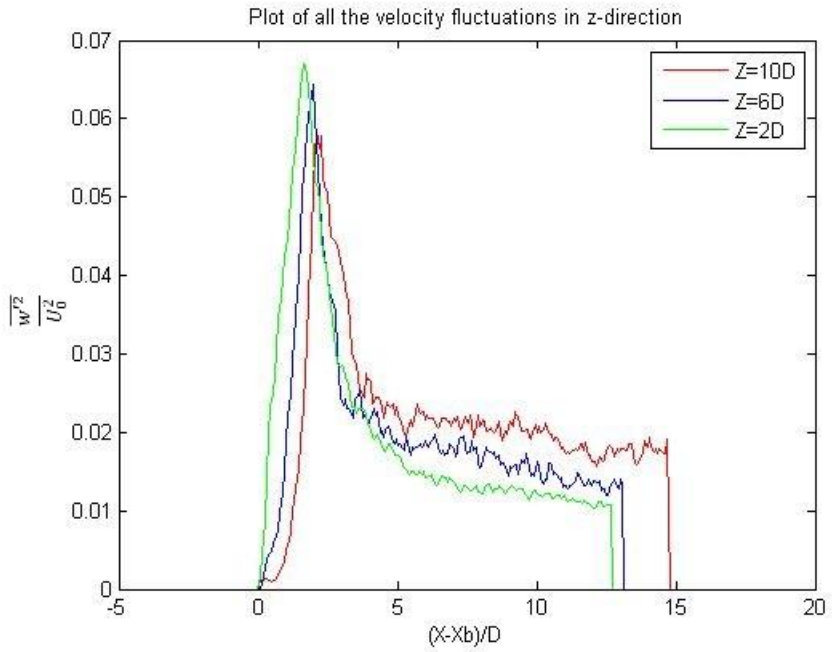

Figure 31: The mean square values of the velocity fluctuations in z-direction downstream of the cylinder for Z=10D, Z=6D and Z=2D. w' represent the velocity fluctuations.

In Figure 31 one can see that the maxima of the $\frac{\overline{w'^2}}{U_0^2}$ are slightly higher as the depth increases, and that the maxima appears slightly closer to the cylinder surface. This may come from an inclination of the vortex shedding axis leading to higher fluctuations from vortex shedding in the z-direction that is closer to the cylinder surface. The increasing values of $\overline{w}^2$ with increasing depth are not in agreement with Gallardo et al (2014) [6]. This be an effect of the resolution in time and space for PIV being too coarse to catch the turbulent fluctuations associated with the vortex shedding. Since the vortex shedding is supressed as the depth increases, the effect of not being able to catch the turbulent fluctuations will decrease as the depth increases. The driving force of the fluctuations will then be the downdraft. In Figure 32, Figure 33 and Figure 34 it is evident that the peaks from the PIV experiments are shifted downstream compared to the peaks from the numerical studies, but less at increasing depth. The difference between the plots are decreasing with increasing depth, and the same trends can be seen for both the experimental and numerical study.

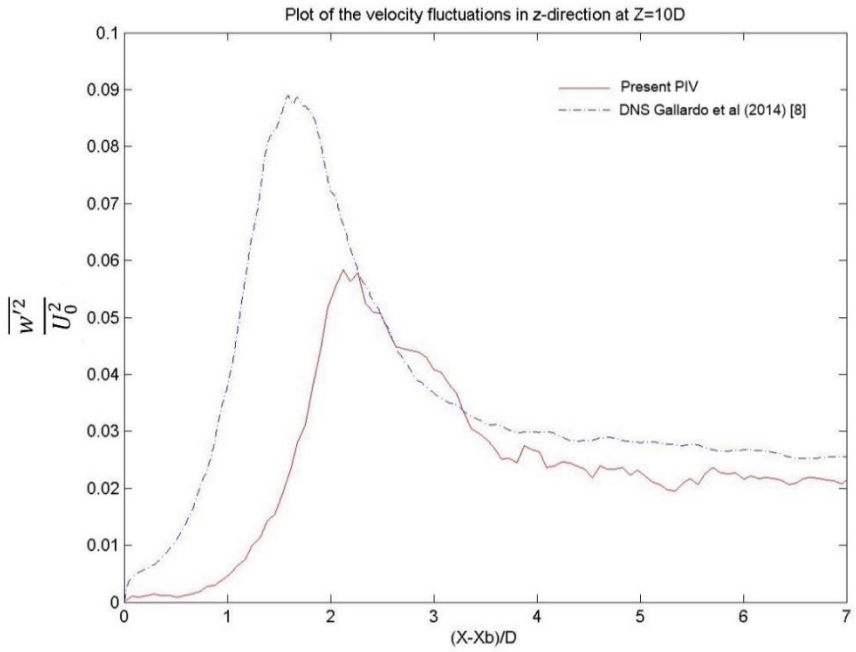

Figure 32: Lineplot of the mean square of the velocity fluctuations in z-direction downstream of the cylinder at the centreline at Z=10D. The measurements are compared with data from Gallardo et al (2014) [6] with similar flow conditions. w' represent the velocity fluctuations.

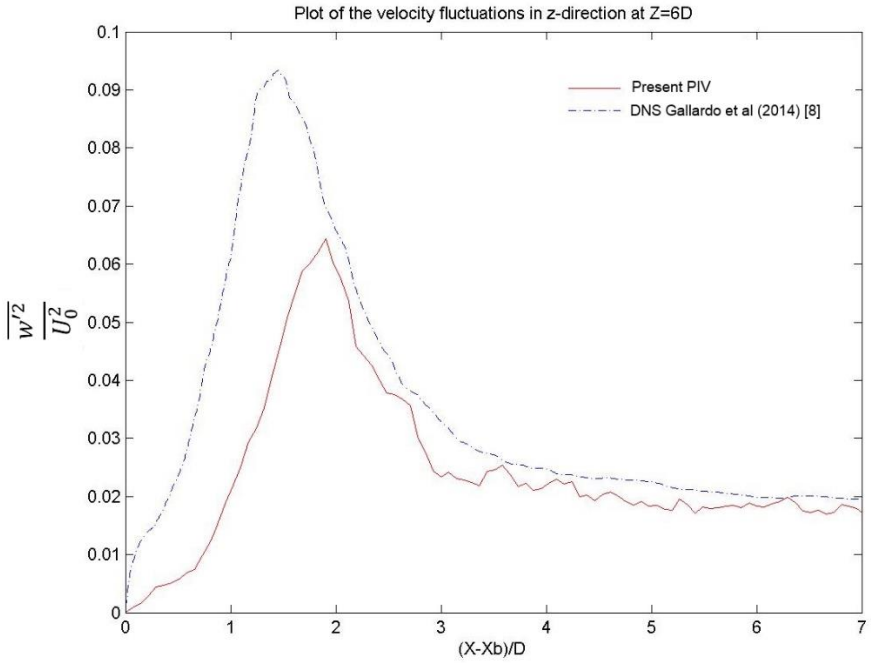

Figure 33: Lineplot of the mean square of the velocity fluctuations in z-direction downstream of the cylinder at the centreline at Z=6D. The measurements are compared with data from Gallardo et al (2014) [6] with similar flow conditions. w' represent the velocity fluctuations.

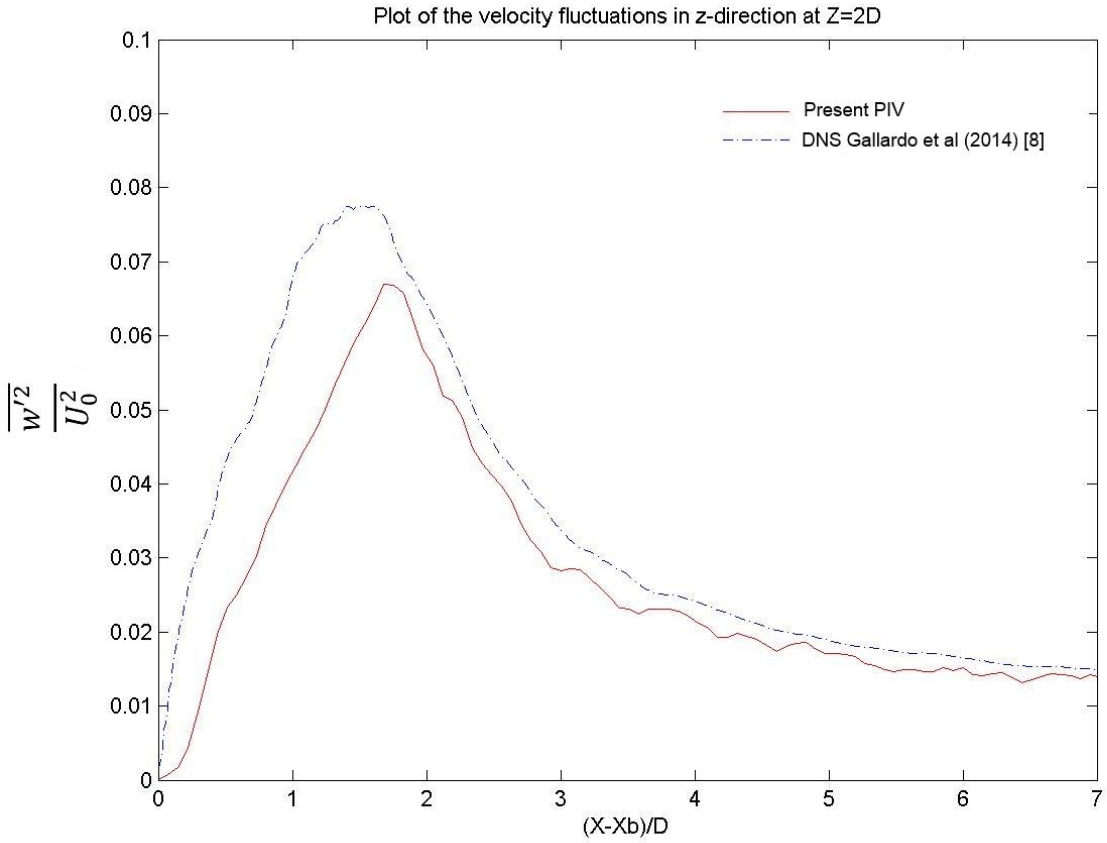

Figure 34: Lineplot of the mean square of the velocity fluctuations in z-direction downstream of the cylinder at the centreline at Z=2D. The measurements are compared with data from Gallardo et al (2014) [6] with similar flow conditions. w' represent the velocity fluctuations.

8.5 Strouhal number

From the spectral plots of the speed in y direction we can see that the vortex shedding frequency is stronger as you approach the vertical part of the pipe This is in good agreement to the findings of Gallardo et al (2014) [6], corresponding to the plots Z/D=8,12 and 16 in Figure 8. The shedding frequency is also slightly higher as the depth is increased. This is in agreement with the results found from Gallardo et al (2014) [6]. The measured St Increases with the smallest increment it can increase, so there are some uncertainties regarding this measurement. There can be observed a small spectral density peak around the third harmonic as Gallardo et al (2014) [6] observed. This spectral density peak cannot be seen at Z=2D, this is also in agreement with the numerical results of Gallardo et al (2014) [6]. The spectral plots of the frequencies at Z=10D and Z=6D are taken from the measurements at the upper centreline, and the spectral plot at Z=2D was taken from the measurements at the lower centreline. Table 1 shows the different measured peak frequencies and St. The measured frequencies show a slight increase as the depth increases, and a second peak of the frequency spectra similar to the peak Gallardo et al (2014) [6] found at $3f_{St}$. The amplitude of the spectral peaks decreases as the depth increases. This implies a loss of periodicity of the wake and is in agreement with Gallardo et al (2014) [6]. The slight change in frequency suggests vortex dislocations in the wake as already observed.

Table 1: Strouhal frequencies, Strouhal numbers and frequency of second peak in the Frequency spectra at 5D behind the cylinder wall in the centre plane at Z=10D, Z=6D and Z=2D.

Position	Frequency [s^{-1}]	Measured St	St from [6]	Frequency of second peak [s^{-1}]
Z=10D	1,348	0,2152	0,218	4,043
Z=6D	1,348	0,2152	0,22	4,071
Z=2D	1,406	0,2244	0,222	No second peak

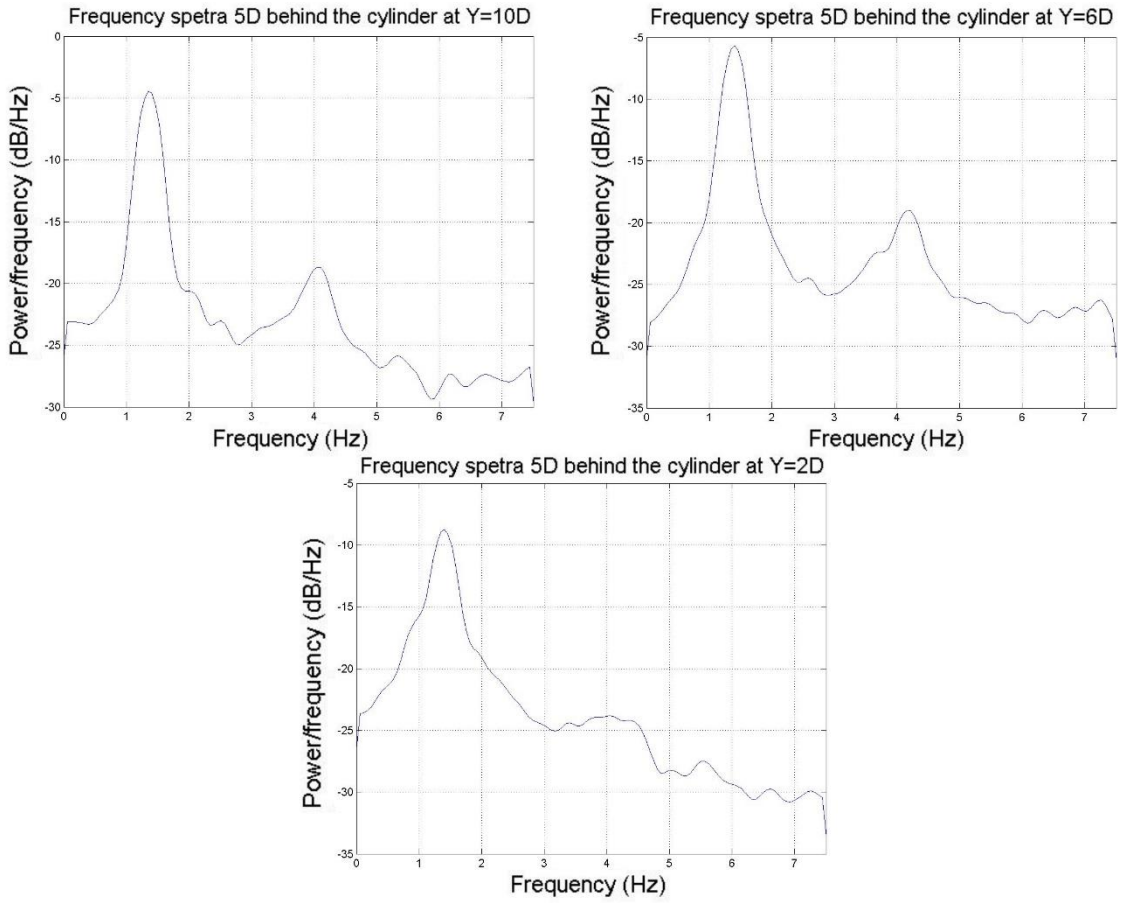

Figure 35: Measured frequency spectra for the cross flow velocity 5D behind the cylinder wall at Z=10D (upper left), Z=6D (upper right) and Z=2D (lower).

As seen in Figure 35 the spectral peaks become broader and less distinct as the inclination of the cylinder increases. This is in agreement with Wang et al (2011) [18] for inclinations of straight circular cylinders, and Figure 8 from Gallardo et al (2014) [6].

8.6 Instantaneous flow fields

Instantaneous velocity fields were plotted for the whole time series for all views. These pictures show some phenomena occurring in the wake after the cylinder. Figure 36 show the y-component of the flow behind the cylinder at the center plane. The vortices shown are not parallel to the cylinder surface as they propagate downstream, but are approximately parallel to the cylinder surface as they are shed. This is in agreement with Gallardo et al (2014) [6]. The vortices also start to break down and lose strength as they propagate downstream.

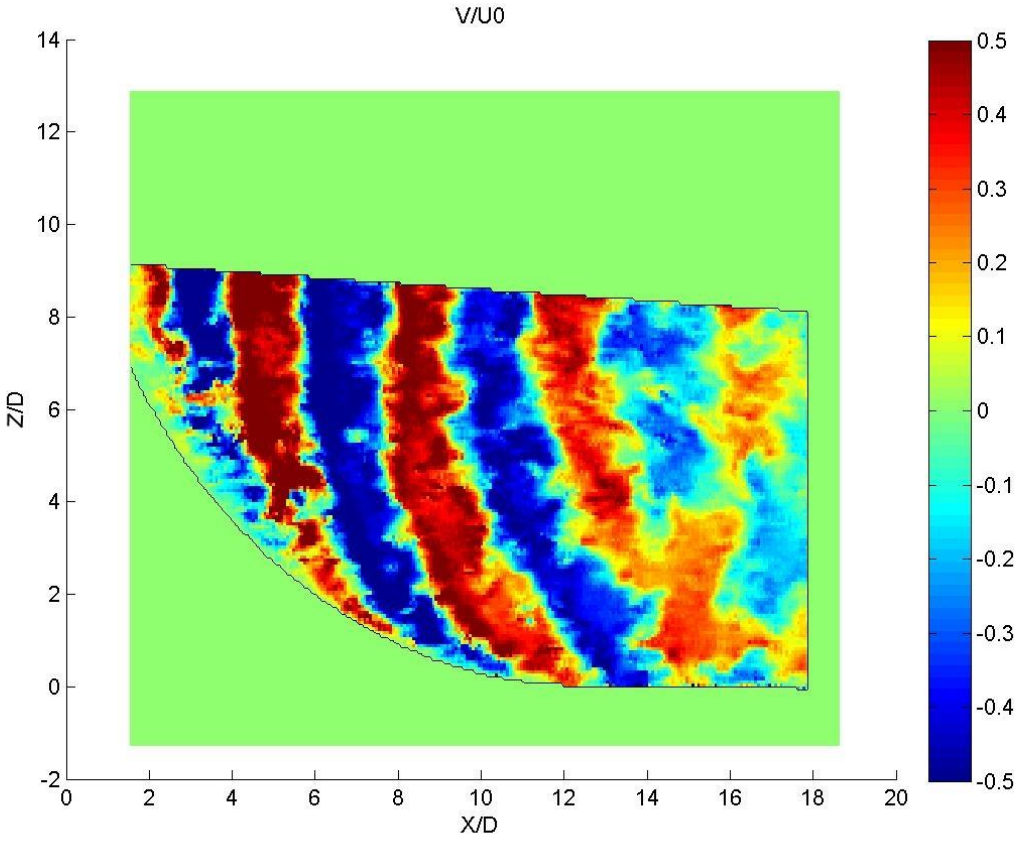

Figure 36: V plotted at the lower centreplane in the wake behind a cylinder. The vortex cells are shed parallel to the cylinder wall, and changes shape as it propagates downstream.

From the instantaneous flow fields in the y-direction vortex dislocations are present. These dislocations occur both in the upper and the lower part of the flow field as shown in Figure 37. The vortex dislocations are both shifted, so the vortex cells are split in two with a slight shift in the streamwise position, and ended so that the vortex in one direction ends and the two vortices at either side merges into one. Gallardo et al (2014) [6] observed vortex dislocations in a similar numerical experiment, but Gallardo et al (2011) [7] did not get a vortex dislocation without the vertical extension. This indicates that the vertical extension is important for the vortex dislocations in the wake. The ending of vortices is observed by e.g Mansy et al (1994) [8] on straight circular cylinders. The vortex dislocations are associated with the different shedding frequencies at different depths.

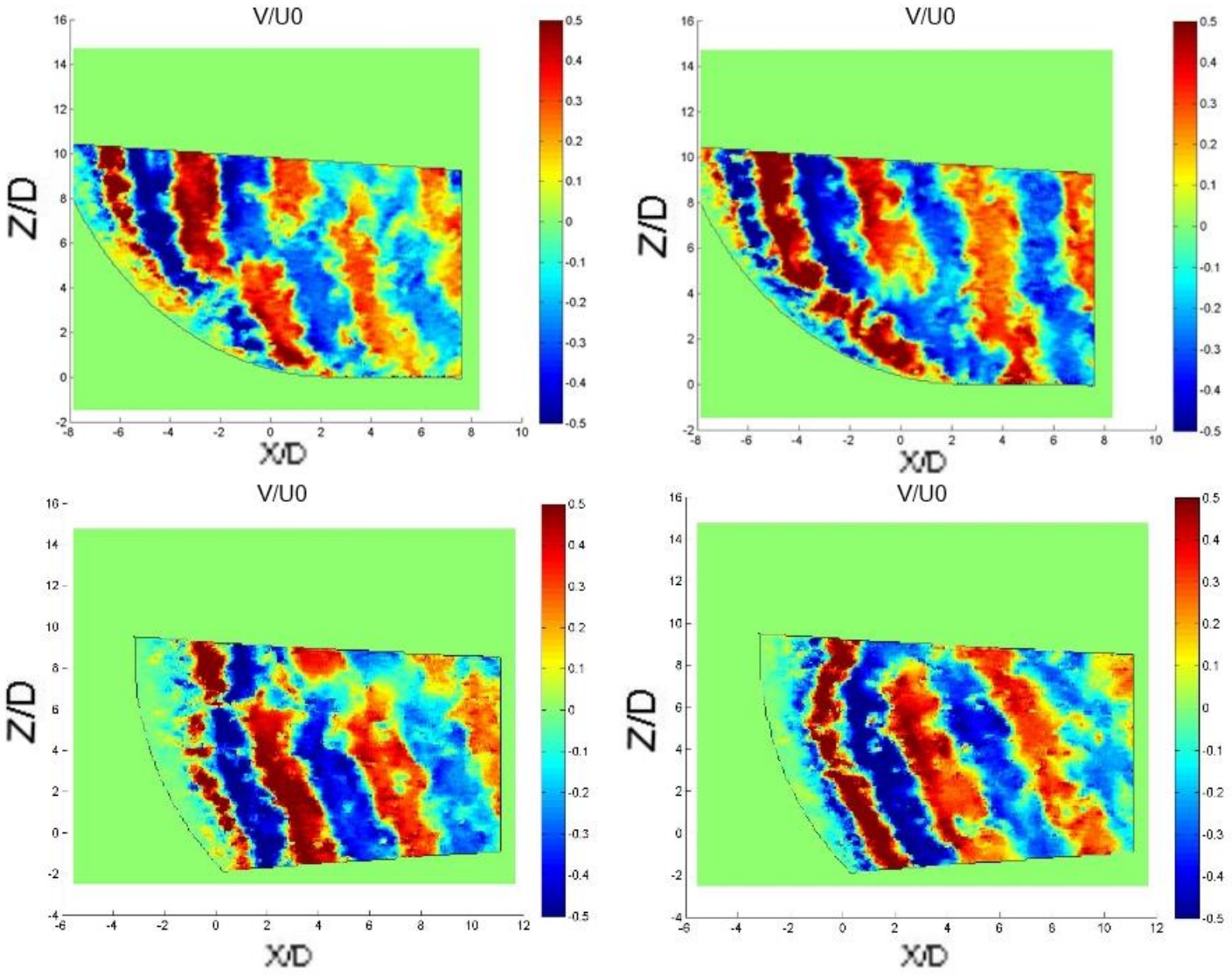

Figure 37: Vortex dislocations. Upper left: Lower part of the centreline measurements, a shift in the vortex cells. Upper right: Lower part of the centreline measurements, a vortex cell ends and the two neighbouring vortices merge. Lower left: Upper part of the centreline measurements, a shift in the vortex cells are also appearing here. Lower right: Upper part of the centreline measurements. A vortex cell ends and the neighbouring vortex cells merge.

8.7 Free shear layer

To investigate the length of the free shear layer the same definition was used as in Prasad et al (1997) [12]. The average vorticity was plotted for all the cross-sectional measurements, and the line where the vorticity was 8% of the maximum measured vorticity marked the end of the free shear layer.

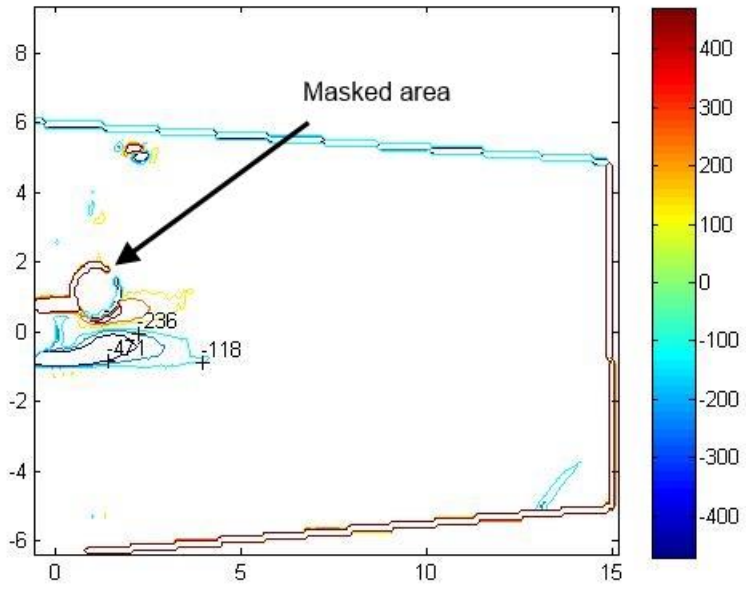

Figure 38: Average vorticity in the flow field at Z=2D. The contours are at 4%, 8% and 16% of the maximum measured vorticity in this plot. The mask has been applied due to brightness in the background image.

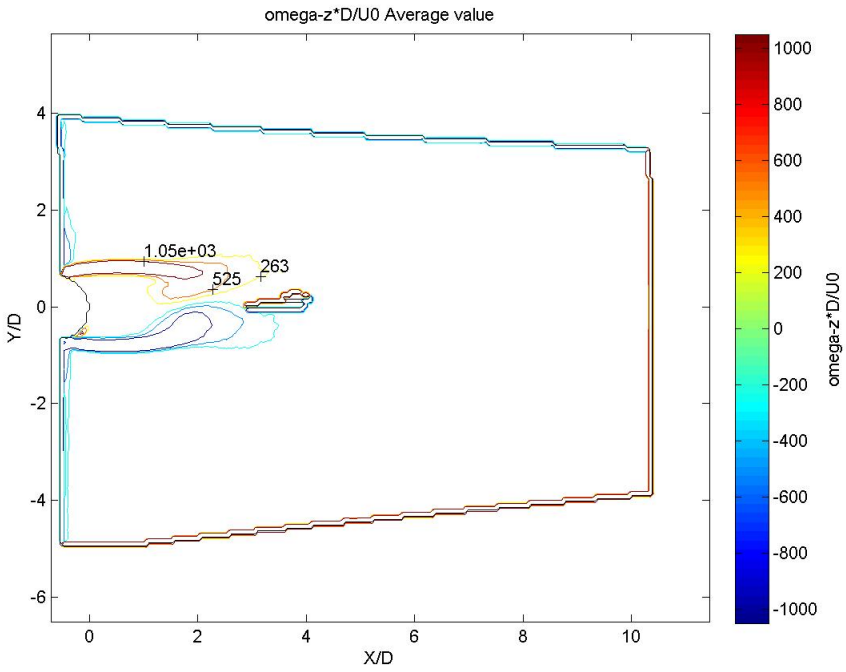

Figure 39: Average vorticity in the flow field at Z=6D. The contours are at 4%, 8% and 16% of the maximum measured vorticity in this plot.

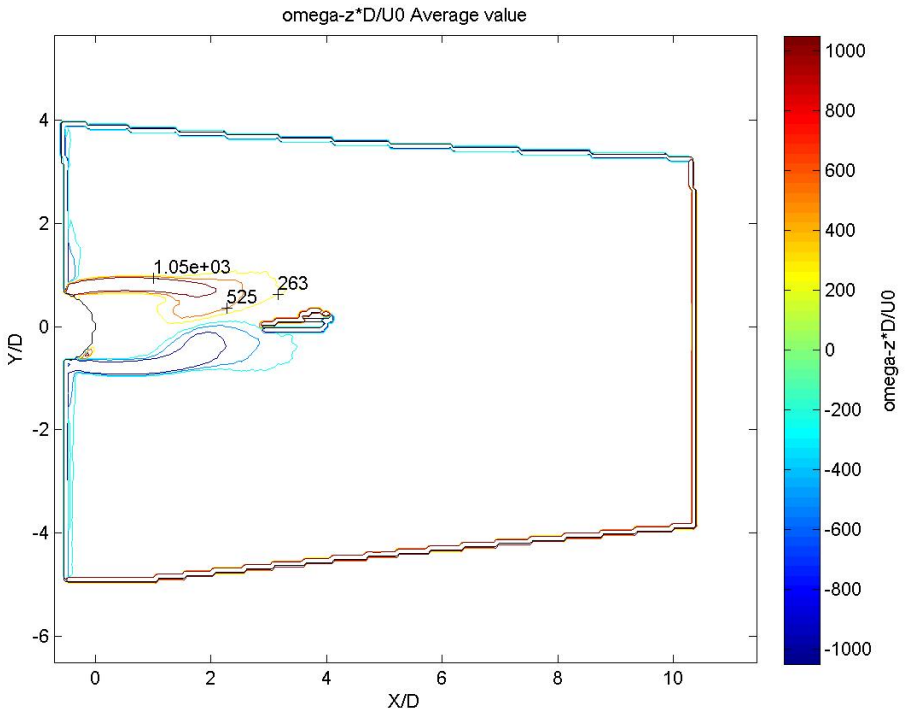

Figure 40: Average vorticity in the flow field at Z=10D. The contours are at 4%, 8% and 16% of the maximum measured vorticity in this plot.

Table 2: Measured max vorticity and shear layer length at the depths Z=2D, Z=6D and Z=10D. Taken from Figure 38, Figure 39 and Figure 40.

	Max [$\omega_z D/U_0$]	Free shear layer length [D]
Z=10D	6565	2,572
Z=6D	6378	2,46
Z=2D	2944	2,901

The maximum value used here is the absolute maxima. The free shear layer has a much lower maxima at Z=2D compared with the other two maxima, and a longer free shear layer length. The increase in free shear layer length may come from a loss in interaction between the free shear layers due to the downdraft downstream of the wake acting in the same manner as a splitter plate. The resolution of the PIV images may give a generally lower max vorticity than the real one. This comes from the definition of vorticity:
$\omega_z = \frac{dV}{dx} - \frac{dU}{dy}$. The vorticity is averaged over one cell size, and if Δx or Δy is large, the maximum vorticity may be lost. This may lead to a shorter free shear layer in reality, and deviations on the free shear layer length due to different resolution in space. The plot of the 8% of average vorticity in Figure 38, Figure 39 and Figure 40 has a distinct difference in shape compared to Figure 5, although the 4% contour line has a similar shape. This indicates that the definition of the free shear layer length made by Dong et al (2006) [5] are not suited to calculate free shear layer length for PIV experiments. The free shear layer length is in some agreement with the results Ramberg (1983) [14] presents, the part of the cylinder with the highest inclination angle has the largest free shear layer length, but the part of the cylinder with the smallest inclination angle do not have the smallest free shear layer length.

8.8 Line profiles LDV

Measurements were taken with LDV to compare with the PIV measurements. The measurements were taken as mean values for U velocities and W velocities with a 60 second measurement at each point in a line at Z=8D. Figure 41 shows a lineplot of the U velocities measured by the LDV. A recirculation region is present at X/D=1 with an amplitude of $0.1U_0$. This is about half the amplitude of the recirculation region measured with PIV. The recovery to the free stream value in good agreement with Gallardo et al (2014) [6], and this implies that the LDV has some difficulties regarding measurements of small velocities. The mean W velocities shown in Figure 42 looks erroneous with high and irregular amplitudes. The plots in Figure 41 and Figure 42 are not validated with respect to SNR (Signal to Noise Ratio). Table 3 show the measured velocity and SNR for a single measurement point at Z=8D and X=3,5D. The measured speed had some peaks with a velocity up to $17U_0$ and a SNR over 4. Figure 43 and Figure 44 are validated by removing all measurements for each point that has a SNR less than 4. For the lineplot of the U velocity there is not much difference except a slightly less retarded wake and a slightly larger backflow. For the lineplots on the W velocity the plot has changed drastically in the range 0<x<4. Large irregular amplitudes are present, but only for negative flow.

Table 3: Measurements of the W velocity at Z=8D and X=3,5D with origin on the lee side of the straight part of the cylinder. Measured in a single point over 60 seconds.

Time [ms]	Speed [m/s]	SNR
0	0,031	5,76
2304	-2,547	3,58
7978	0,099	14,29
8343	-0,038	7,22
8762	0,026	12,34
12279	0,073	8,65
16226	-2,764	4,36
22382	0,002	10,31
23387	-2,914	2,96
25684	-2,828	1,63
31543	-1,782	1,16
31707	-2,579	4,00
34425	-2,753	3,81
37683	-0,027	9,66
39526	-2,631	4,53
42288	-0,888	1,00

Table 3 show measurements with amplitudes of more than -1m/s and a SNR higher than 4. This shows that you need to take caution when using the LDV at the CWT with regards to the signal to noise ratio. The minimum SNR was then increased to 5 in Figure 45. It is evident here that many measurement points had no measurements with SNR>5 giving a significant loss of data points. An examination of the limiting speeds of the LDV when the velocity can be both positive and negative and experience regarding The LDV equipment might give better results.

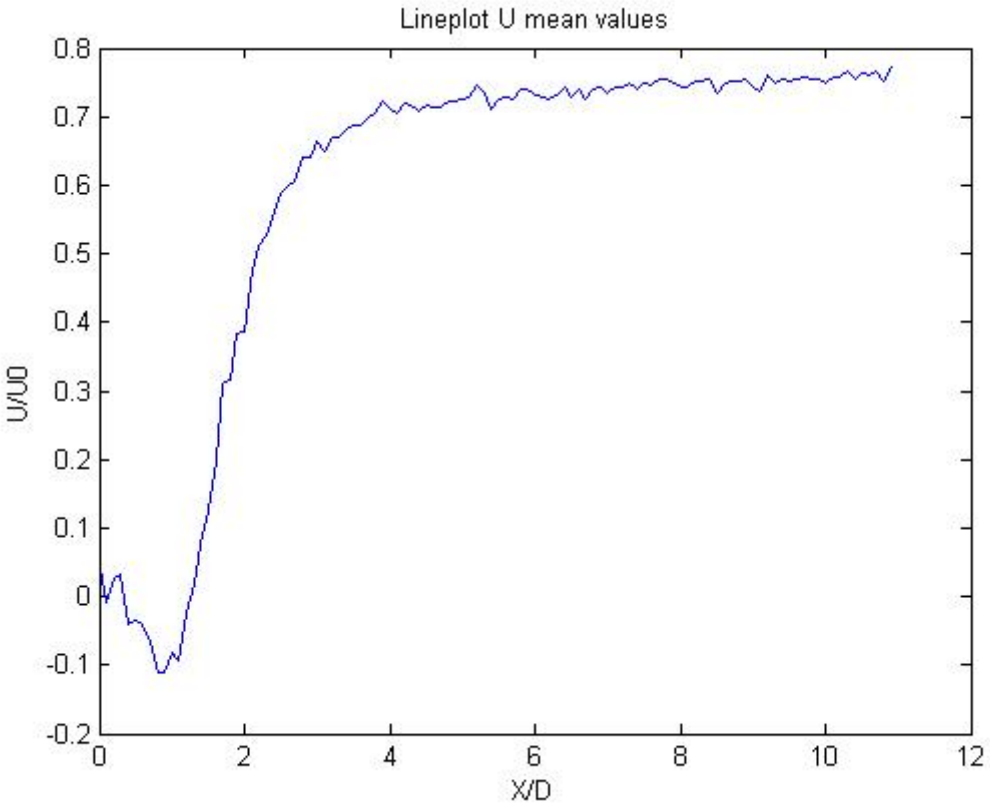

Figure 41: Lineplot of LDV measurements of the U velocity at Z=8D with 60 seconds measurement in each point. Measurements for all SNR ratios are included.

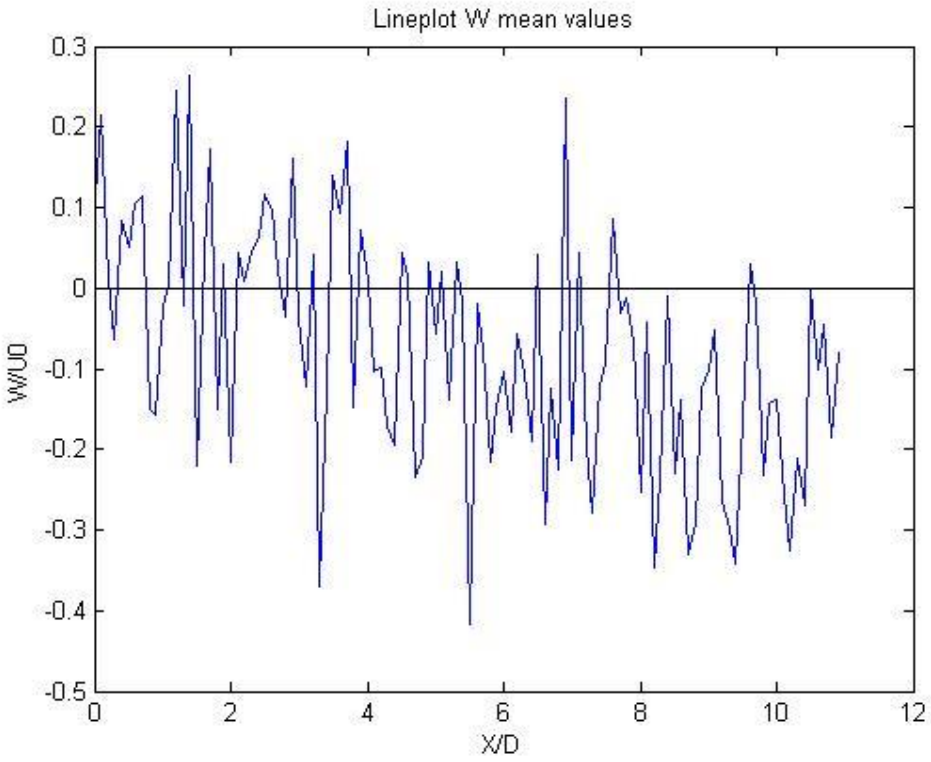

Figure 42: Lineplot of LDV measurements of the W velocity at Z=8D with 60 seconds measurement in each point. Measurements for all SNR ratios are included.

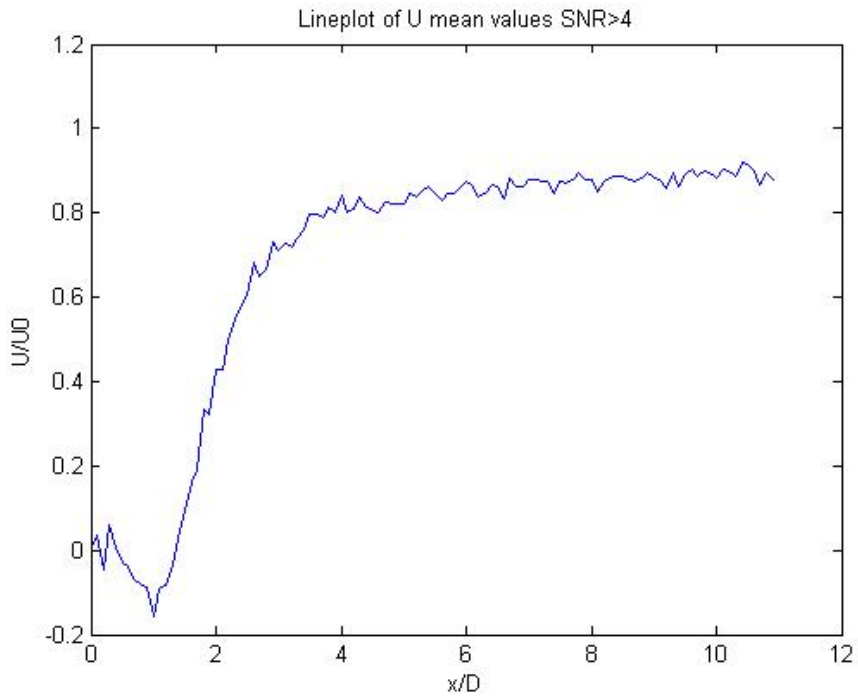

Figure 43: Lineplot of LDV measurements of the U velocity at Z=8D with 60 seconds measurement in each point. All measurement values with a SNR ratio below 4 has been deleted.

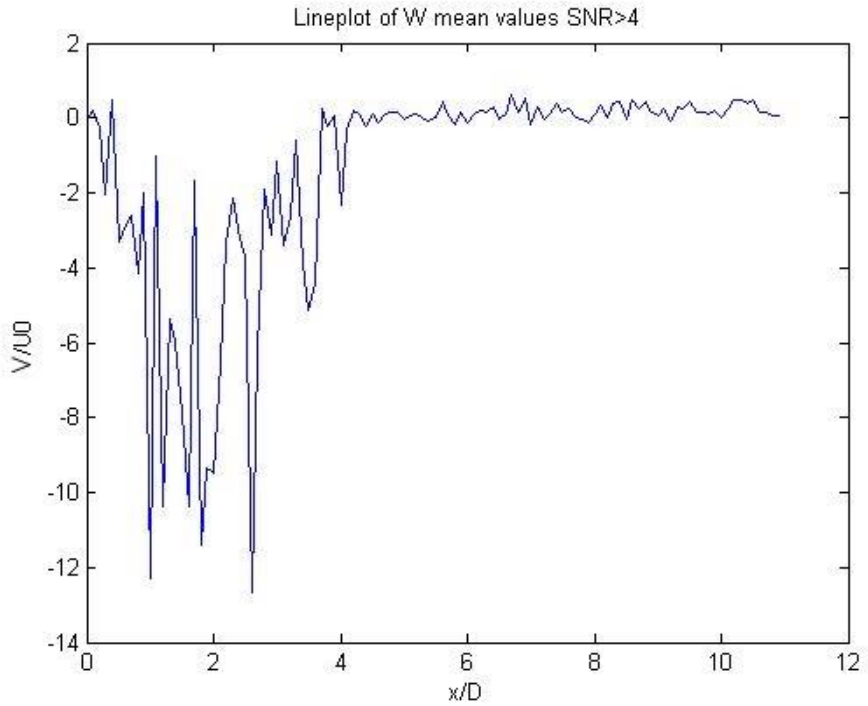

Figure 44: Lineplot of LDV measurements of the W velocity at Z=8D with 60 seconds measurement in each point. All measurements with a SNR ratio below 4 has been deleted.

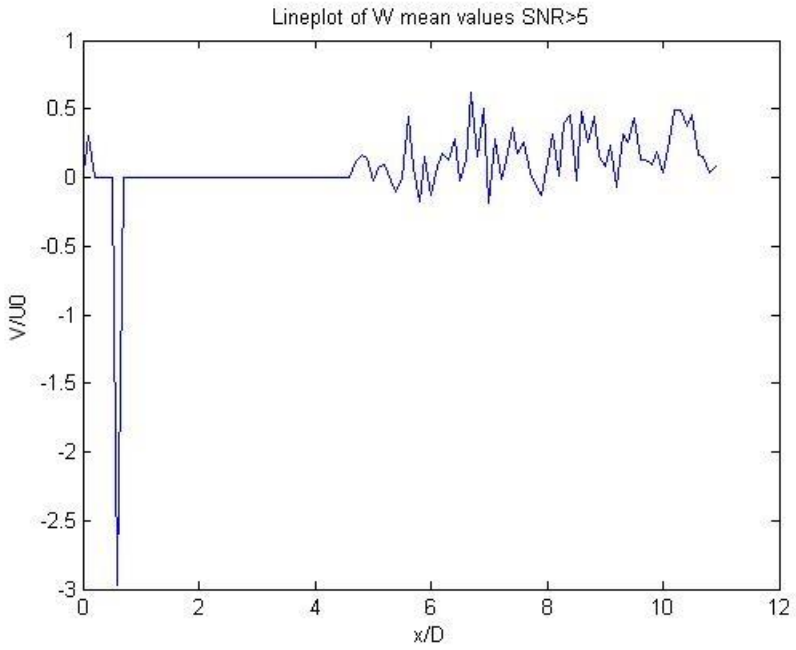

Figure 45: Lineplot of LDV measurements of the W velocity at Z=8D with 60 seconds measurement in each point. All measurements with a SNR ratio below 5 has been deleted. Measurement points in space without measurements are plotted as 0.

9 Error sources and uncertainty

Adrian and Westerweel (2010) [1] list the ultimate measures of quality for a PIV experiment. These are the fraction of the valid interrogation data, the bias error, or pixel locking and the accuracy of the data.

9.1 LDV

The LDV has a measurement range from $1^{mm}/_{S}$ to $300^{m}/_{S}$. According to the PIV measurements the vertical velocities in the tank are between -$38^{mm}/_{S}$ and $1{,}6^{mm}/_{S}$. This indicates that the measurements of vertical velocity behind the cylinder are within the limits of what the LDV are able to measure, and that measurement difficulties may occur. Reflection from the tank wall, damages on the tank wall and other reflective obstacles encountered by the laser beam may also influence the measurements and induce noise.

9.2 Accuracy (PIV)

Figure 46 shows a plot of the rms of the uncertainty in the placement of each vector compared to the actual particle displacement in each interrogation window, with respect to the number of particles in each interrogation cell for the lower centreline plot. The figure shows that even with a small number of particles within each cell the uncertainty regarding vector placement is small, the maximum uncertainty of the vector placement is 0,02D. This is due to the high resolution of vectors in the plots. An estimation of the number of particles in each interrogation window is ~7. This gives an rms value of the uncertainty of each vector placement of ~0.008D. This uncertainty has an influence of on the measured velocity gradients and the measured vorticity.

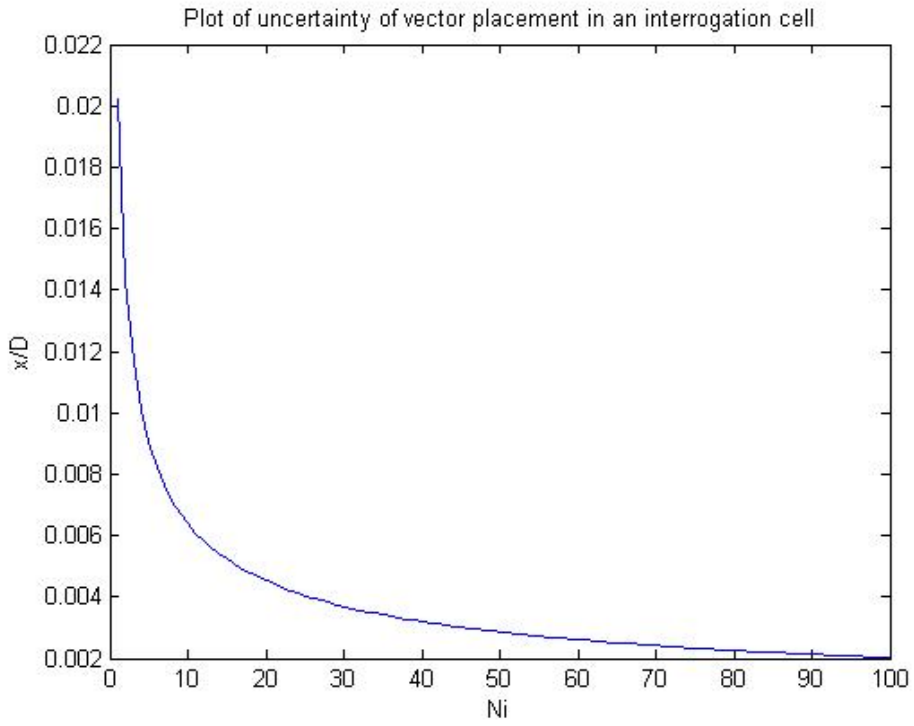

Figure 46: Rms values of the uncertainty of vector placement for each vector measured in diameters. For the lower centreline plot. Based on $\frac{D_I}{\sqrt{12N_I}}$ from [1].N_i is the number of particles within each interrogation cell, and D_i is the length scale of the interrogation cell.

9.3 Fraction of valid vectors (PIV)

Valid vectors are vectors not interpolated or calculated from other correlation peaks than the highest. The fraction of the valid vectors should be greater than 95% if possible. A reason for valid vector rate to be so high is to make it easy to compare neighboring vectors to replace unphysical vectors, and interpolate non-existing vectors. Figure 55 shows an instantaneous field with the different values of validity for the vectors for the cross-section at Z=10D. An observation is made in Figure 55 that the interpolated and replaced vectors in the flow field are positioned near each other, and Figure 53 and Figure 54 shows a similarity in the average of the interpolated vectors and the average rms of the out of plane component of the flow. This indicates that it is the velocity fluctuations of the out of plane component that causes erroneous vectors, and that loss of out of plane correlation is the main reason for invalid vectors. When the invalid vectors are positioned close to each other, it raises a question if the 95% valid vector rate is good enough, or if it should be calculated in a different manner.

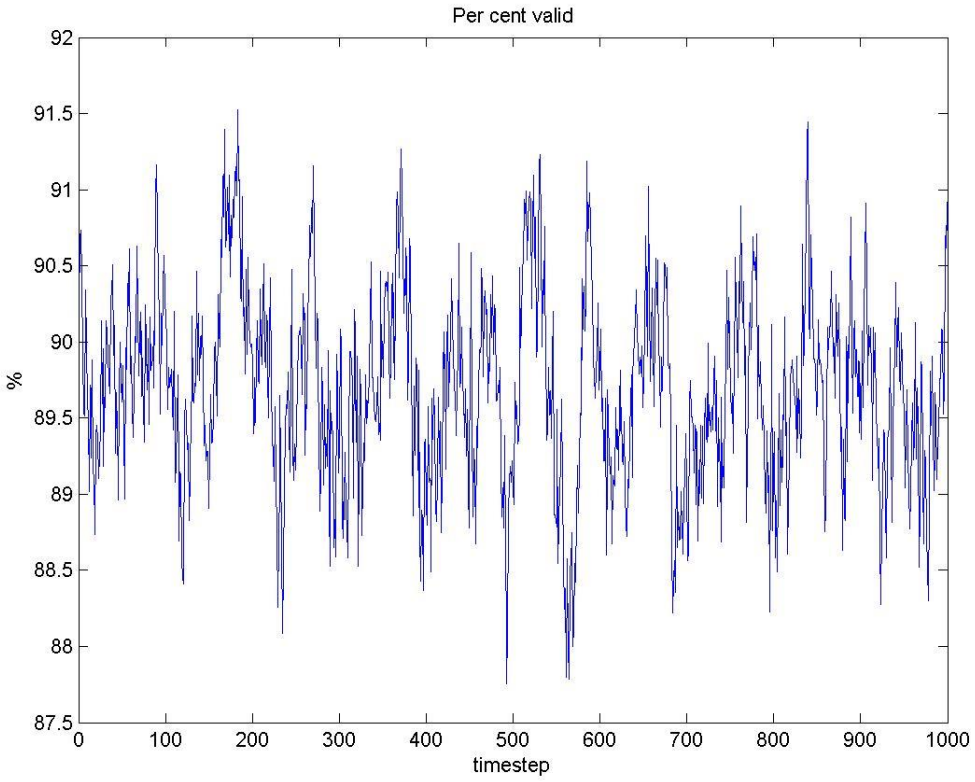

Figure 47: Percentage of valid vectors for each time step. Upper centreline.

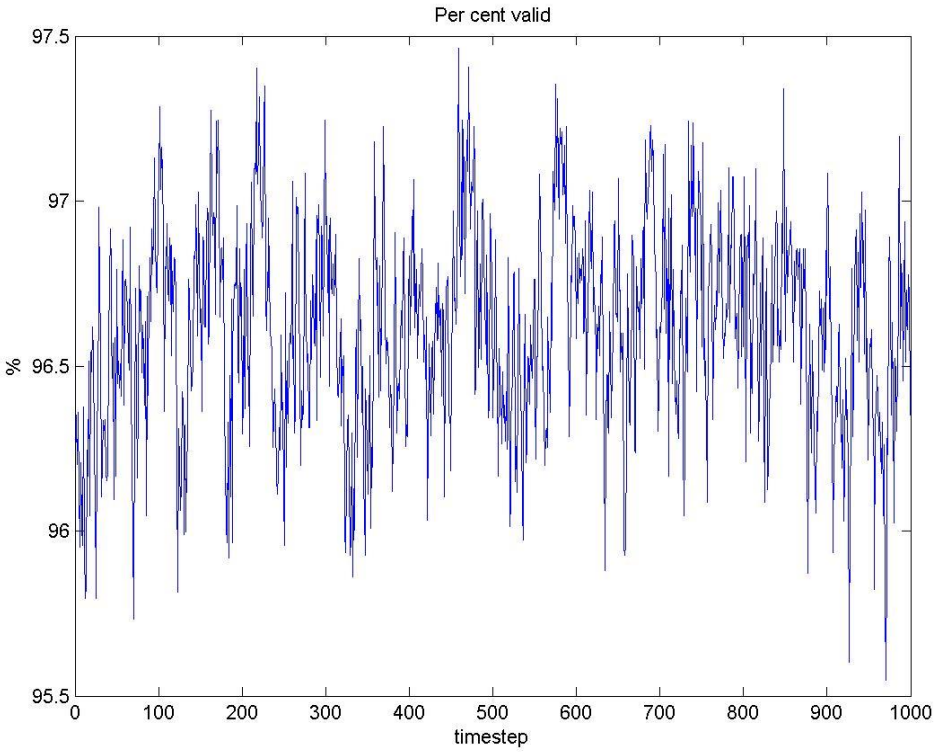

Figure 48: Percentage of valid vectors for each time step. Lower centreline.

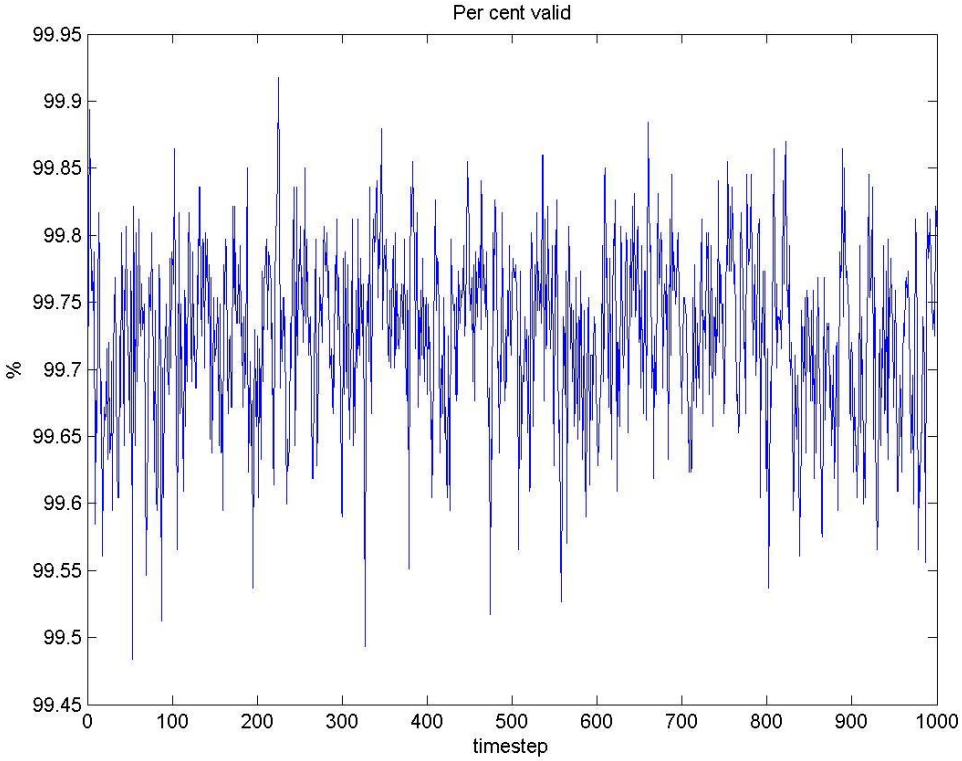

Figure 49: Percentage of valid vectors for each time step. Taken at Z=2D.

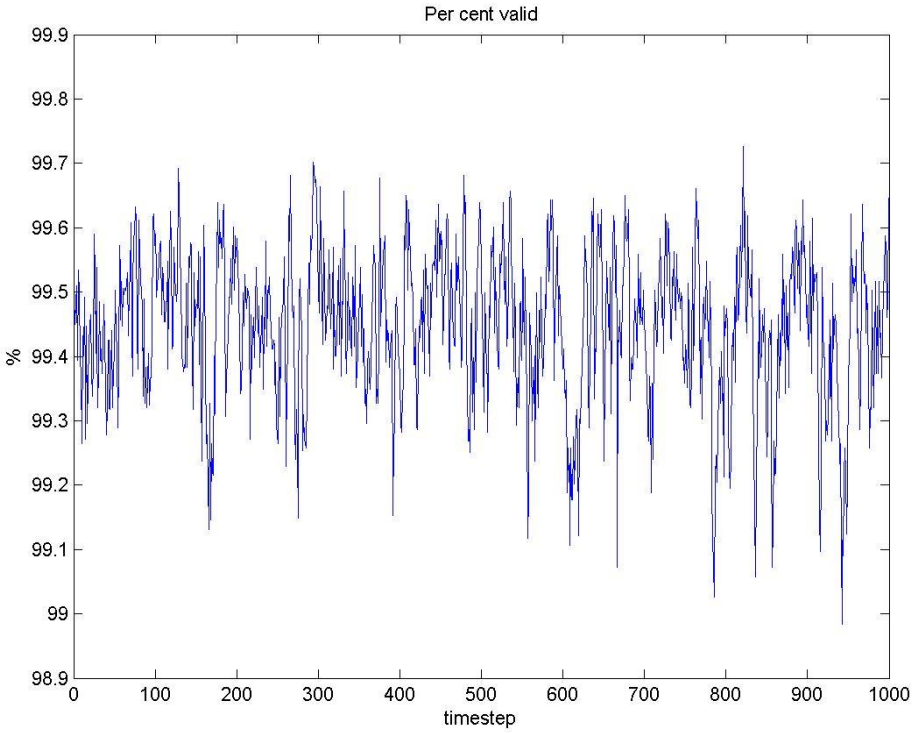

Figure 50: Percentage of valid vectors for each time step. Taken at Z=6D.

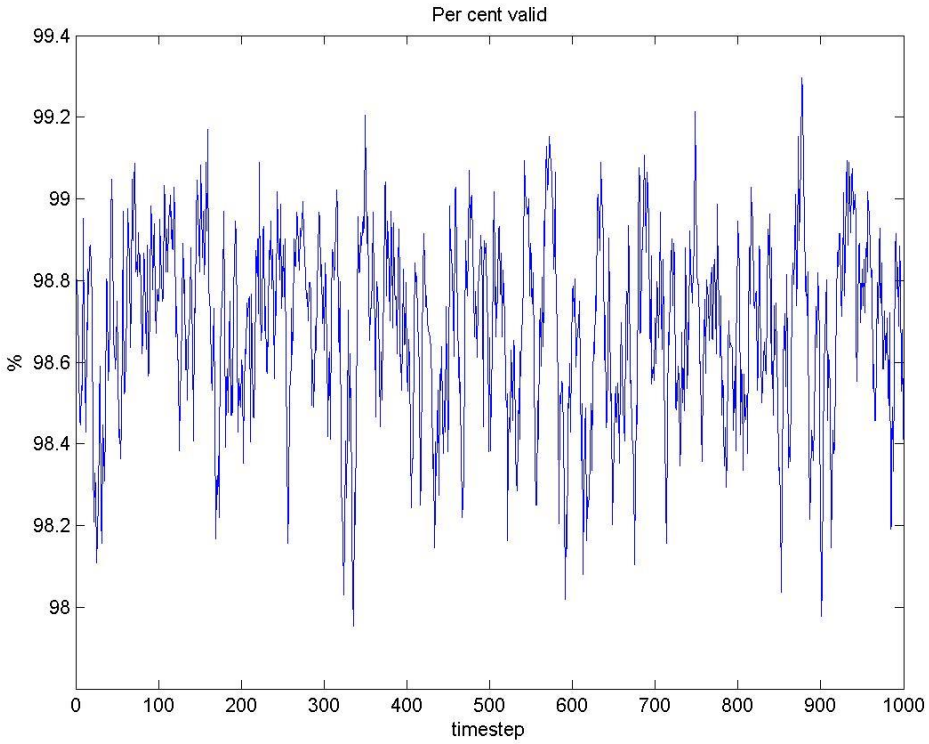

Figure 51: Percentage of valid vectors for each time step. Taken at Z=10D.

Figure 47, Figure 48, Figure 49, Figure 50 and Figure 51 show the fraction of the active vectors that are valid for each timestep in the experiments. In Figure 47 for the upper centreline the fraction of valid vectors is under 95%. The loss of out of plane correlation due to vortex shedding and high out of plane fluctuations in this region are the reason for this. The replaced and the interpolated vectors are calculated from the neighboring vectors. The result of the high fraction of invalid vectors is that the peak of the out of plane velocities and fluctuations are locked to the largest speed measured as seen in Figure 27. The same is also seen for the lower centreline plot in Figure 48, but on a smaller scale due to weaker vortex shedding strength. It is clear from Figure 47, Figure 48, Figure 49, Figure 50 and Figure 51 that the cross-sectional plots have a significantly higher validation rate than the centreline plots. In the cross-sectional plots the out of plane component of velocity is mainly the slight up or downdraft and in the centre plane plots the vortex shedding is the reason for the out of plane velocity. The out of plane velocity and field from vortex shedding is much larger than the downdraft and this leads to a smaller fraction of valid vectors in the centreline plots and especially for the upper centreline plot due to the strong vortex shedding close to the vertical part of the cylinder. The out of plane velocity may lead to an out of plane loss of correlation. From the plots of average interpolated vectors and vectors using a peak different from the highest correlation peak, it is evident from Figure 56 and Figure 57 that the regions in the centreline plots with the lowest validation rate is in the region with the highest mean square values of the cross flow velocities, which is in the vortex shedding region. It is also logical that the upper centreline plot has a lower validation rate compared to the lower centreline due to the stronger vortices. When comparing Figure 52 and Figure 53 with Figure 54 one can see an indication of coherence between the fluctuations out of plane and the interpolated and replaced vectors. This indicates that the out of plane loss of correlation is a main reason for invalid vectors even for a cross-sectional plot at Z=10D

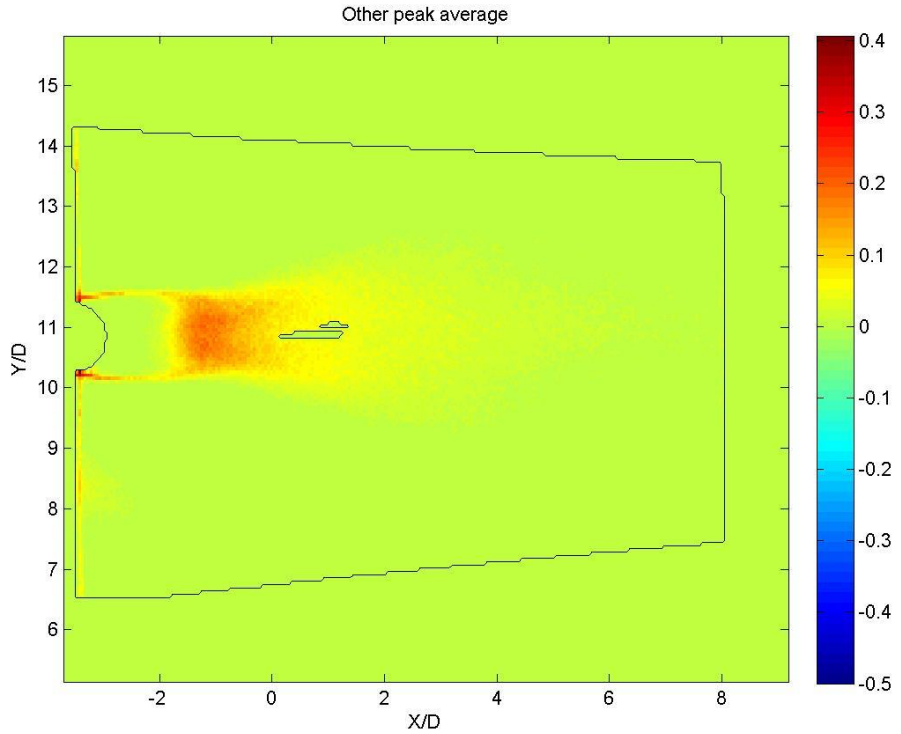

Figure 52: Average non valid vectors where the vectors are replaced by a different peak than the highest correlation peak. Taken at the cross-section Z=10D and averaged over all timeteps.

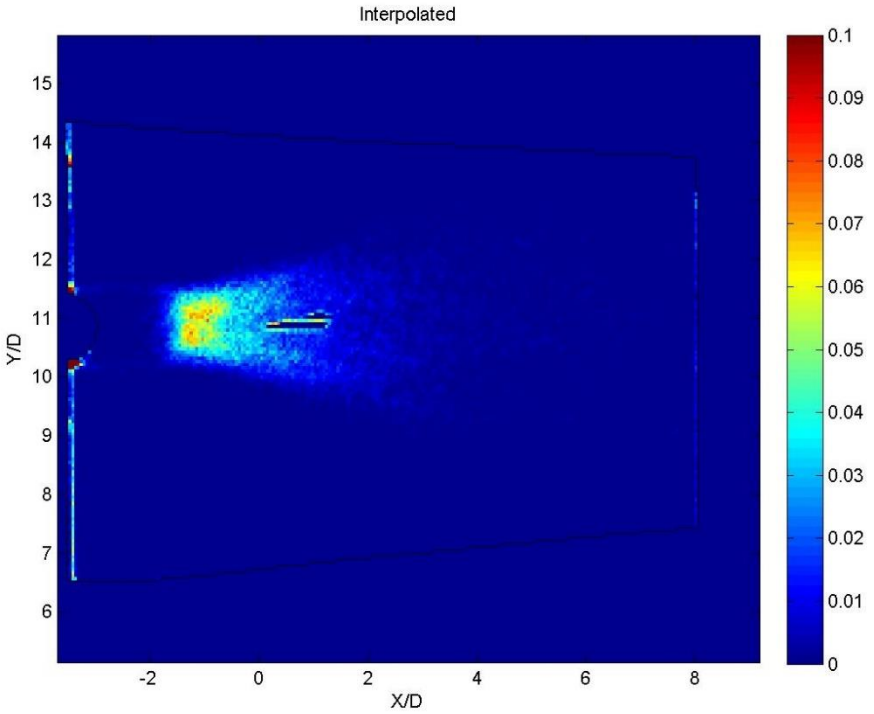

Figure 53: Average non valid vectors where the vectors are interpolated. Taken at the cross-section Z=10D and averaged over all timesteps.

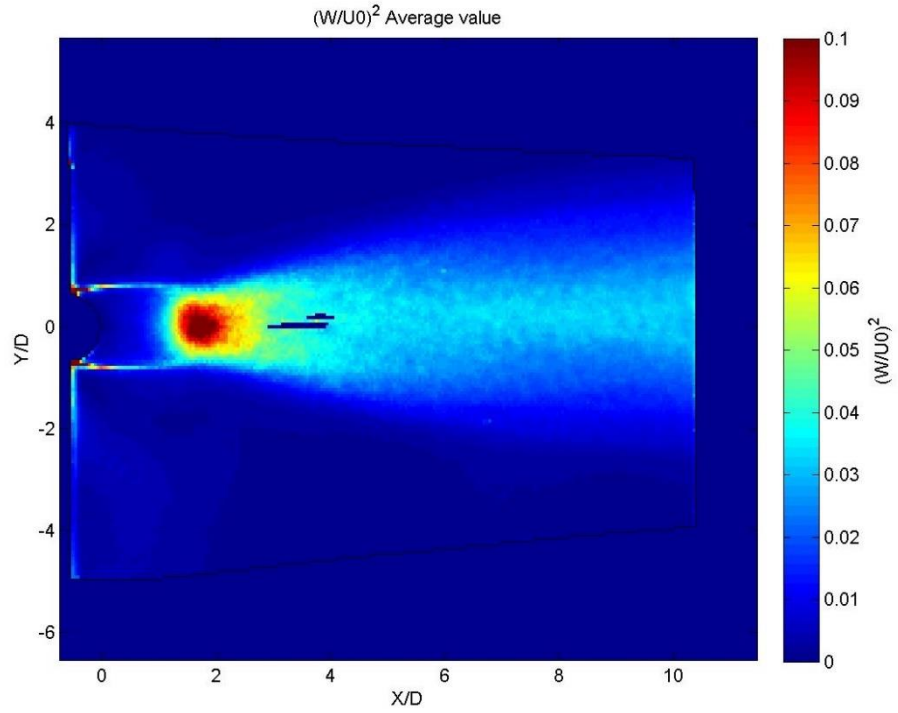

Figure 54: Mean square of the velocity fluctuations in z-direction. Taken at the cross-section Z=10D.

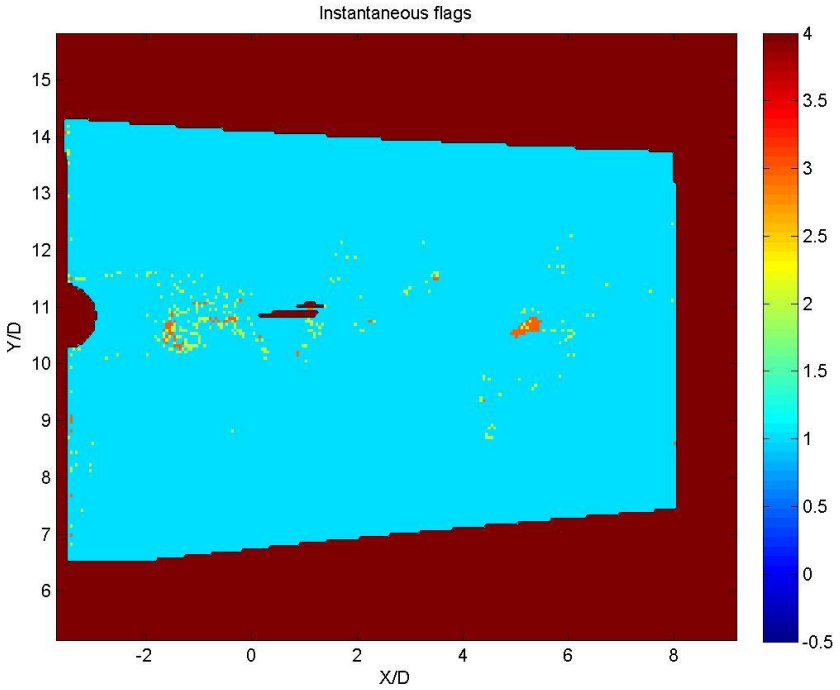

Figure 55: Instantaneous field of the flags of the vectors. The value 1(or turquoise) represents valid measurements, the value 2(or green) represents vectors not taken from the highest correlation peaks. The value 3(or orange) represents vectors interpolated from adjacent vectors. The value 4(or deep red) represents masked vectors. The interpolated vectors often appear in groups as seen around 6D downstream of the cylinder. Taken at the cross-section Z=10D.

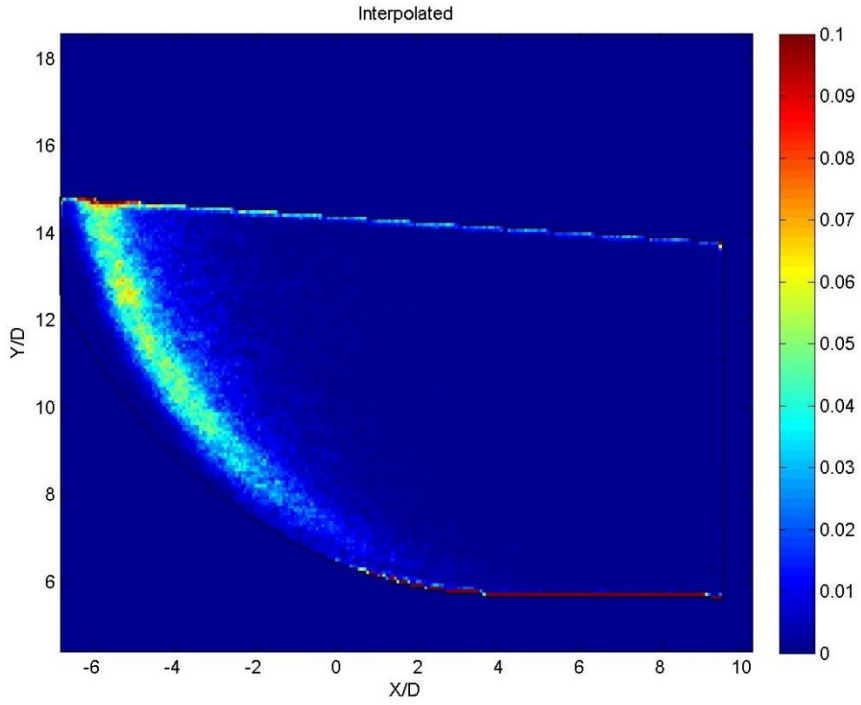

Figure 56: Average non valid vectors where the vectors are interpolated. Taken at the cross-section Z=10D and averaged over all timesteps.

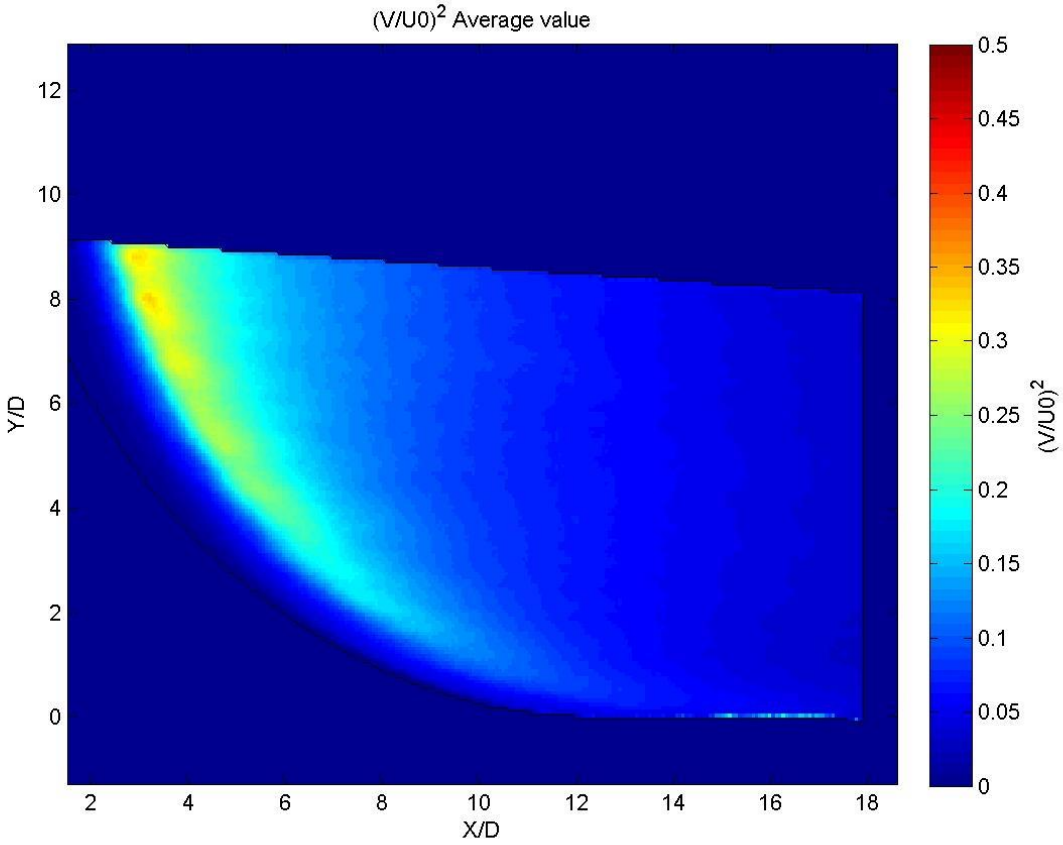

Figure 57: Mean square values of the cross flow velocity V for the lower centreline.

9.4 Pixel locking (PIV)

Figure 58 and Figure 59 show histograms of the horizontal and vertical displacement by pixels for all vectors in one time instant for the upper centreline, lower centreline and the sub-pixel displacement for all vectors for the same views. The histograms of the horizontal and vertical displacement by pixels for Z=10D, Z=6D and Z=2D can be seen in the appendix under pixel locking. The experiments appears not to suffer from pixel locking for any views, even though the particle image diameter was small, about 1-2 pixels and the interrogation region was 16x16 pixels. The reason for this is probably the number of particles within each interrogation region being sufficient to average the speed within each interrogation window in an efficient manner.

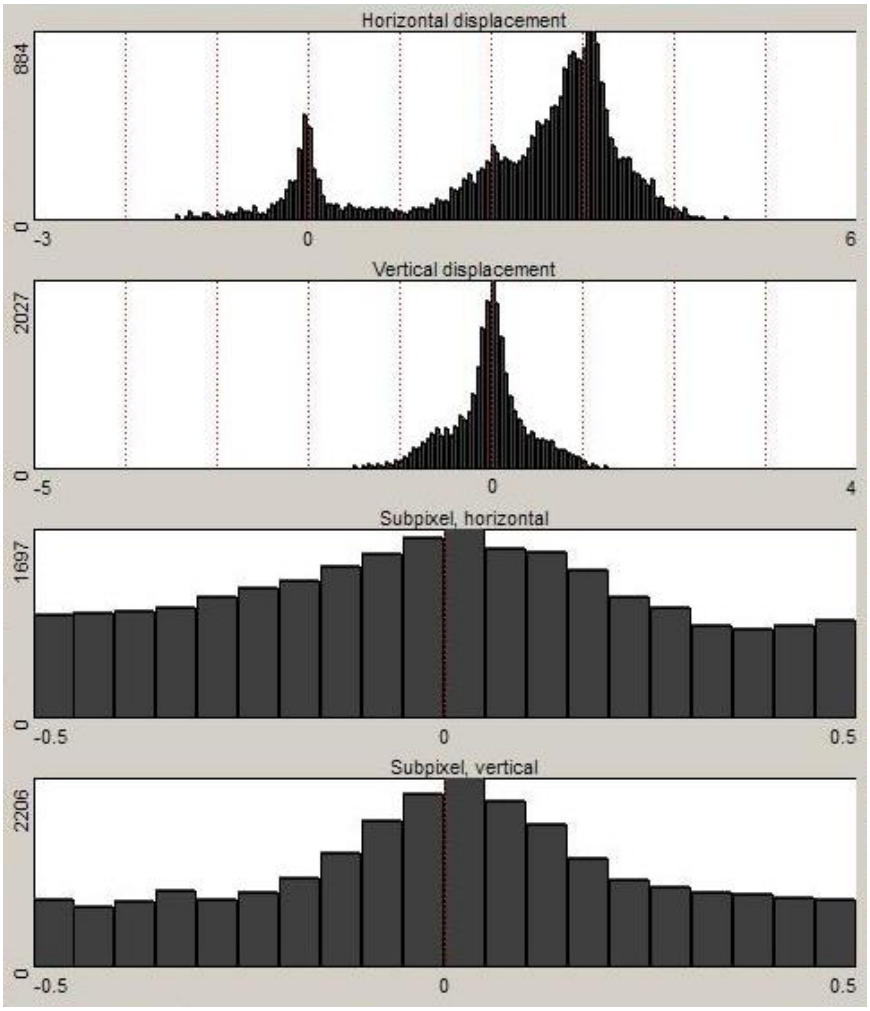

Figure 58: Measurements of pixel displacement in number of pixels and sub-pixels. Pixel displacement are measured in vertical and horizontal direction. Upper centreline.

In Figure 58 the first signs of pixel locking appears. A peak can be seen at the horizontal displacement of 2 and three pixels in an otherwise steady trend of a bell curve. This peak is small and is within the acceptable limits of pixel locking. A peak around 0 pixel displacement for horizontal and vertical speed are expected since some parts of the flow field will experience zero velocity behind parts of the nearly vertical cylinder.

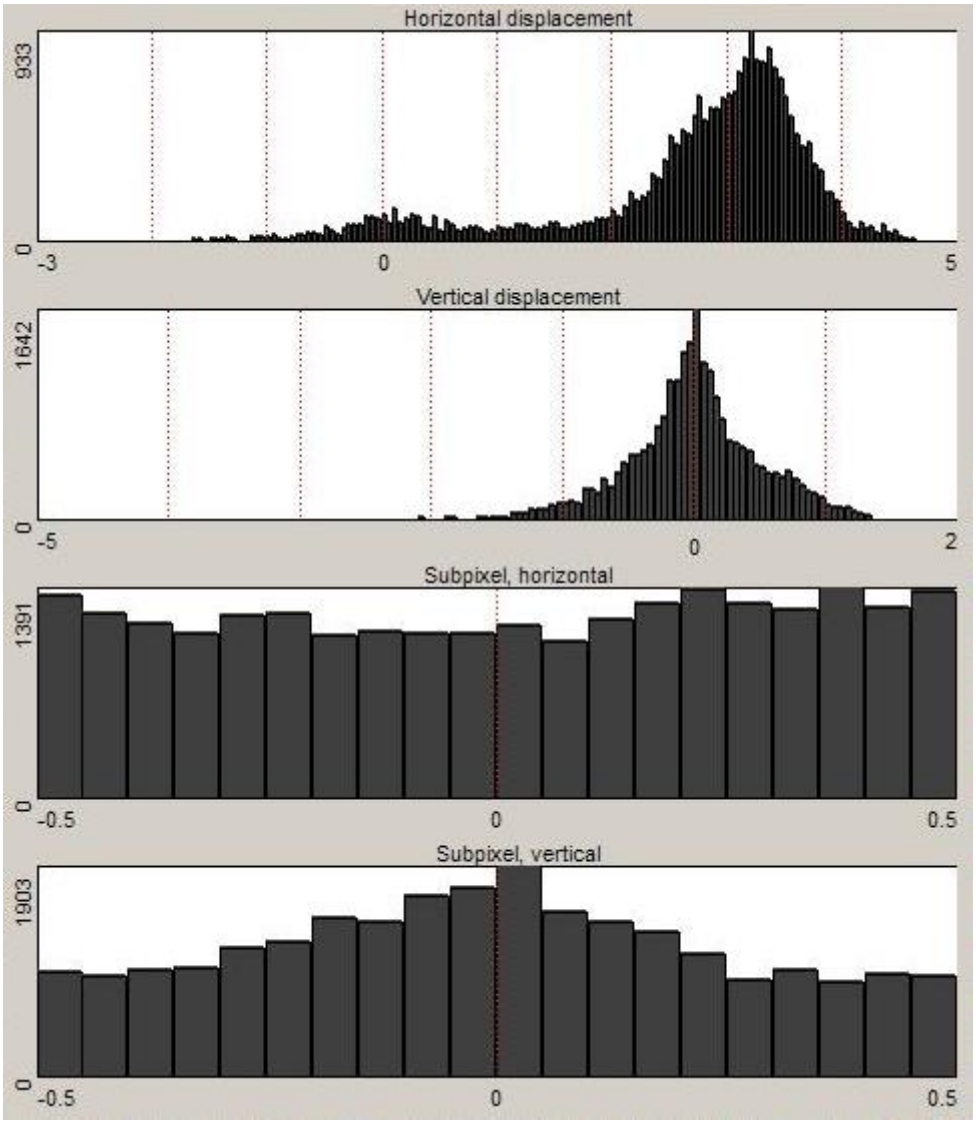

Figure 59: Measurements of pixel displacement in number of pixels and sub-pixels. Pixel displacement are measured in vertical and horizontal direction. Lower centreline.

In Figure 59 no signs of pixel locking occur, the peak at 0 pixel displacement in horizontal direction has nearly vanished compared to Figure 58, but that is also expected since the recirculation region is smaller for the lower part of the cylinder.

9.5 Position of the laser sheet (PIV)

The average out of plane velocity of the center plane plots is a good indicator of where the laser sheet is positioned. Figure 60 show the average out of plane velocity at the upper centreline. This flow field has a trend of a recirculation bubble. This indicates that the measurement is not taken in the absolute center of the cylinder. The trend of the recirculation bubble is somewhat broken and with low strength, so it is assumed that the deviation from the absolute center of the cylinder wake has small influence on the results. Figure 61 shows the lower centreline out of plane average velocity, which shows a flow field with very small amplitudes and with no trends of a recirculation region. This indicates that it is taken at the absolute center of the cylinder wake. With a sampling rate of 11 pictures per vortex shedding cycle and an averaging window of 90 vortex shedding cycles, the influence of the sampling and time window on the average flow field are assumed negligible.

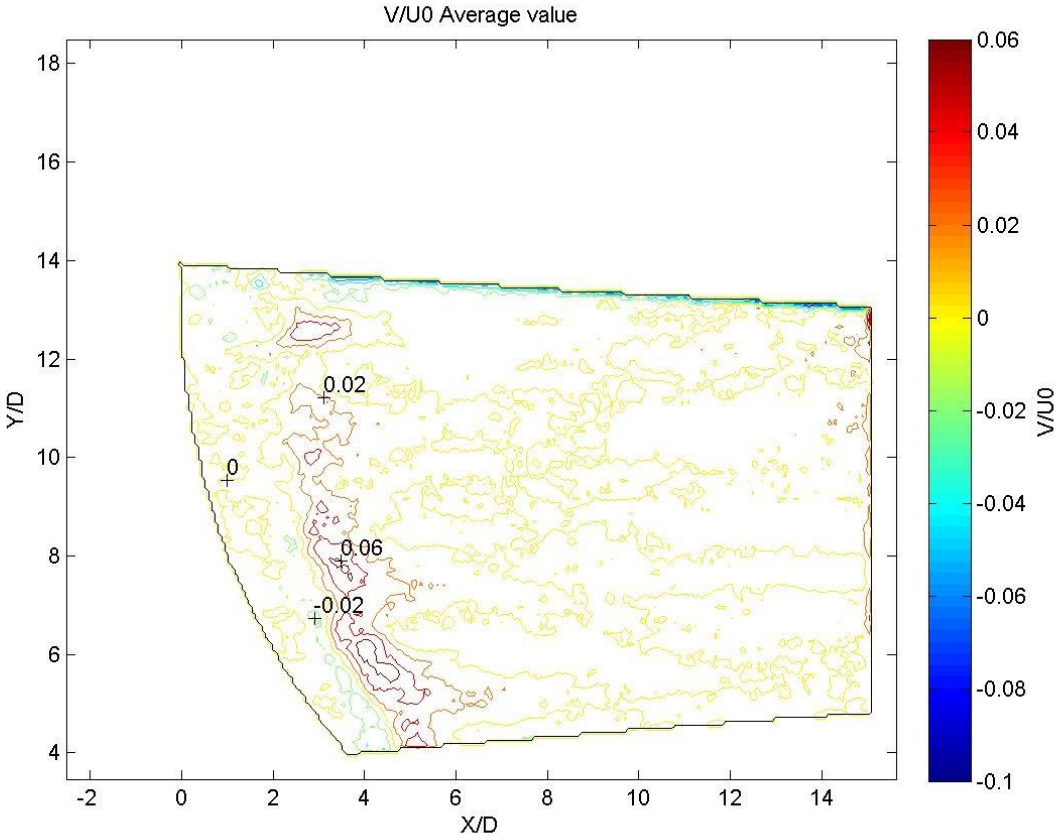

Figure 60: Average flow out of plane for the upper centreline plot.

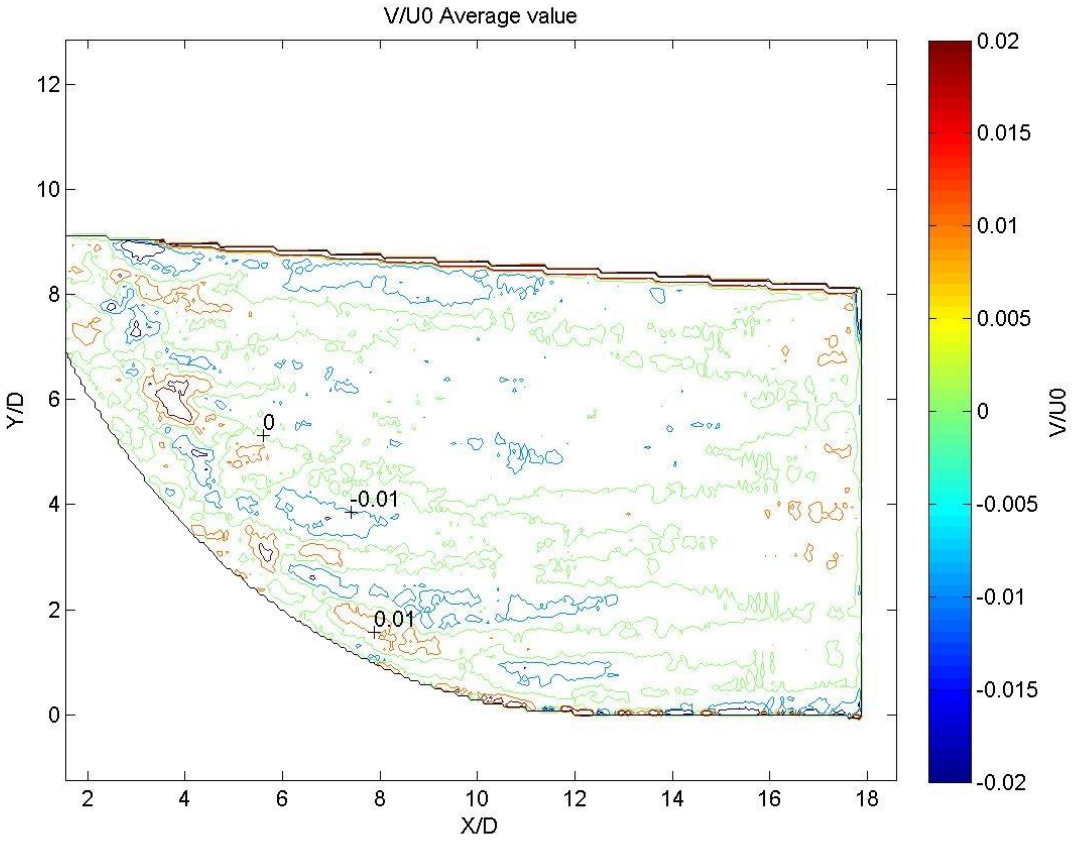

Figure 61: Average out of plane flow for the lower centreline plot.

10 Conclusion

In this thesis there has been conducted experiments with similar flow configurations as Gallardo et al (2014) [6] used in his DNS study. Measurements were taken with PIV in five different planes, and some measurements were done using LDV. The measurements done with LDV measurement gave unrealistic results, probably due to limitations of the equipment. The measurements done with PIV gave realistic results, and many of the trends of the flow were similar to what Gallardo et al (2014) [6] found in his experiment. Vortex dislocations were measured in the center plane of the wake behind the cylinder at different heights and different shapes. The velocity fluctuations show mostly the same trends as in Gallardo et al (2014) [6] with slightly lower maxima and level of details. The average velocity fields show similar trends as in Gallardo et al (2014) [6], but with a recirculation length ~0,4D downstream compared to the results from Gallardo et al (2014) [6]. This may be an effect of the difference in boundary condition and the boundary layer in the tank. The updraft close to the cylinder wall at the center plane downstream of the cylinder was measured, but with a smaller amplitude and area compared to Gallardo et al (2014) [6]. This is probably due to experimental limitations. The downdraft downstream of the cylinder in the center plane had the same amplitudes as for Gallardo et al (2014) [6].

For a different experimental setup, Gallardo et al (2011) [7] did not find the vortex dislocations in the wake. The difference in setup was without the vertical extension. Further work could then include a new experimental setup without the vertical extension to investigate eventual dislocations in the cylinder wake. New equipment could also be put to good use, such as SPIV cameras with higher resolution and undamaged tank walls. The resolution of the camera may help with reducing the timestep between the two picture frames, and reducing the loss of out-of-plane correlation for the centreline plots. Competence in using the LDV as a flow measurement technique for flow in all directions should also be encouraged. An examination of the operational limits of the LDV when measuring positive and negative velocities is recommended.

11 Bibliography

[1] Adrian, R. J. and J. Westerweel (2010). Particle image velocimetry, Cambridge University Press.

[2] Assi, G. R. S., et al. (2014). "Experimental investigation of the flow-induced vibration of a curved cylinder in convex and concave configurations." Journal of Fluids and Structures **44**(0): 52-66.

[3] Bearman, P. (1965). "Investigation of the flow behind a two-dimensional model with a blunt trailing edge and fitted with splitter plates." Journal of Fluid Mechanics **21**(02): 241-255.

[4] Boutier, A. and J.-M. Most (2012). Laser Doppler Velocimetry. Laser Velocimetry in Fluid Mechanics, John Wiley & Sons, Inc.**:** 33-138.

[5] Dong, S., et al. (2006). "A combined direct numerical simulation–particle image velocimetry study of the turbulent near wake." Journal of Fluid Mechanics **569**: 185-207.

[6] Gallardo, J. P., et al. (2014). "Turbulent wake behind a curved circular cylinder." Journal of Fluid Mechanics **742**: 192-229.

[7] Gallardo, J. P., et al. (2011). "Dynamics in the turbulent wake of a curved circular cylinder." Journal of Physics: Conference Series **318**(6): 062008.

[8] Mansy, H., et al. (1994). "Quantitative measurements of three-dim ensional structures in the wake of a circular cylinder." Journal of Fluid Mechanics **270**: 277-296.

[9] Miliou, A., et al. (2007). "Wake dynamics of external flow past a curved circular cylinder with the free stream aligned with the plane of curvature." Journal of Fluid Mechanics **592**: 89-115.

[10] Parnaudeau, P., et al. (2008). "Experimental and numerical studies of the flow over a circular cylinder at Reynolds number 3900." Physics of Fluids (1994-present) **20**(8): -.

[11] Perry, A., et al. (1982). "The vortex-shedding process behind two-dimensional bluff bodies." Journal of Fluid Mechanics **116**: 77-90.

[12] Prasad, A. and C. H. Williamson (1997). "The instability of the shear layer separating from a bluff body." Journal of Fluid Mechanics **333**: 375-402.

[13] Prasad, A. and C. H. Williamson (1997). "Three-dimensional effects in turbulent bluff-body wakes." Journal of Fluid Mechanics **343**: 235-265.

[14] Ramberg, S. (1983). "The effects of yaw and finite length upon the vortex wakes of stationary and vibrating circular cylinders." Journal of Fluid Mechanics **128**: 81-107.

[15] Roshko, A. (1954). "On the development of turbulent wakes from vortex streets."

[16] Strouhal, V. (1878). "Ueber eine besondere Art der Tonerregung." Annalen der Physik **241**(10): 216-251.

[17] Sumer, B. M. and J. Fredsøe (1997). Hydrodynamics around cylindrical structures, World Scientific.

[18] Wang, H., et al. (2011). "Streamwise evolution of an inclined cylinder wake." Experiments in fluids **51**(2): 553-570.

[19] White, F. M. and I. Corfield (1991). Viscous fluid flow, McGraw-Hill New York.

12 List of Figures

13 List of tables

Appendix

Pixel locking

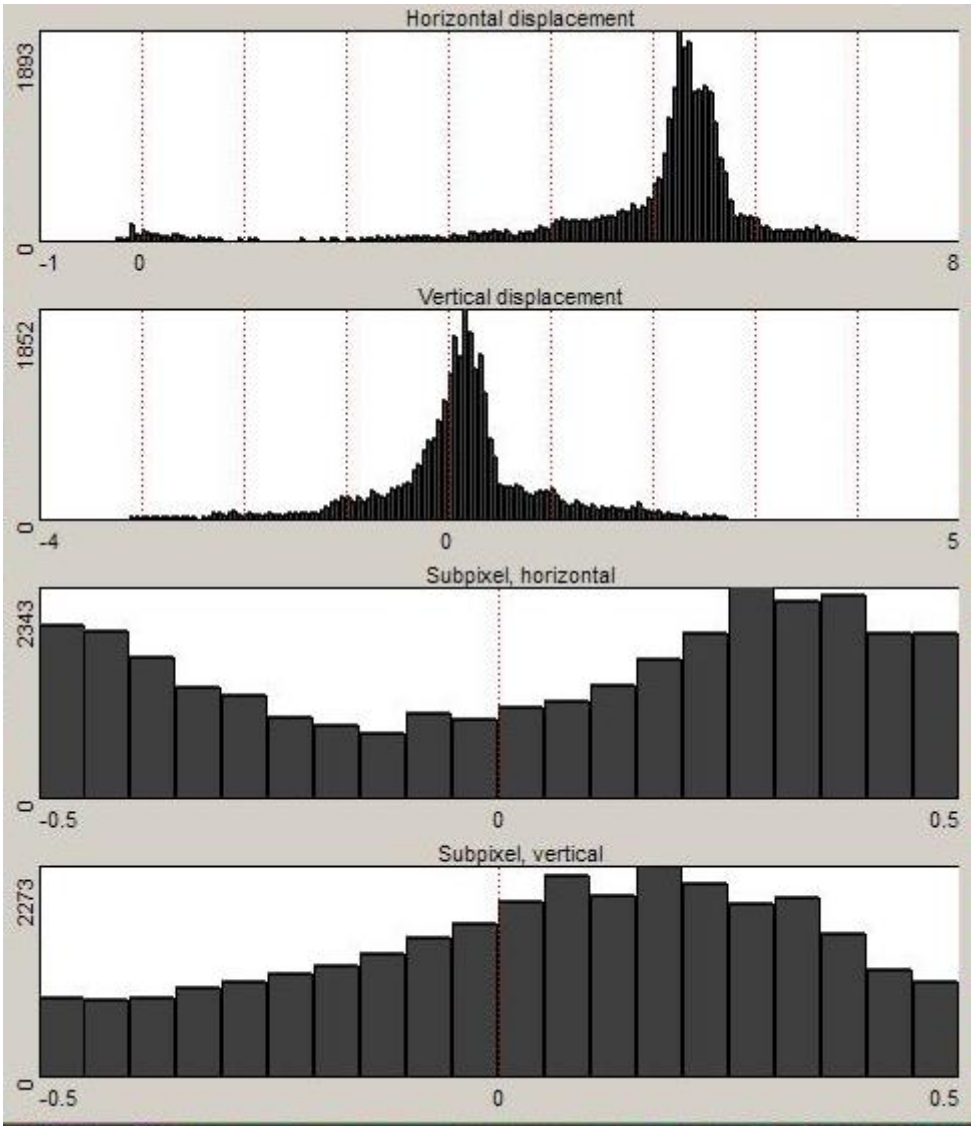

Figure 62: Measurements of pixel displacement in number of pixels and sub-pixels. Pixel displacement are measured in vertical and horizontal direction. Z=10D.

In Figure 62 there is no signs of pixel locking, a bell curve appears in the histogram for horizontal displacement between two pixel displacements. The vertical displacement histogram show that there is a slight overweight of pixel displacement upwards. This may come from the calibration images not being completely horizontal, or the vortex shedding giving a net velocity upwards at this specific time instant.

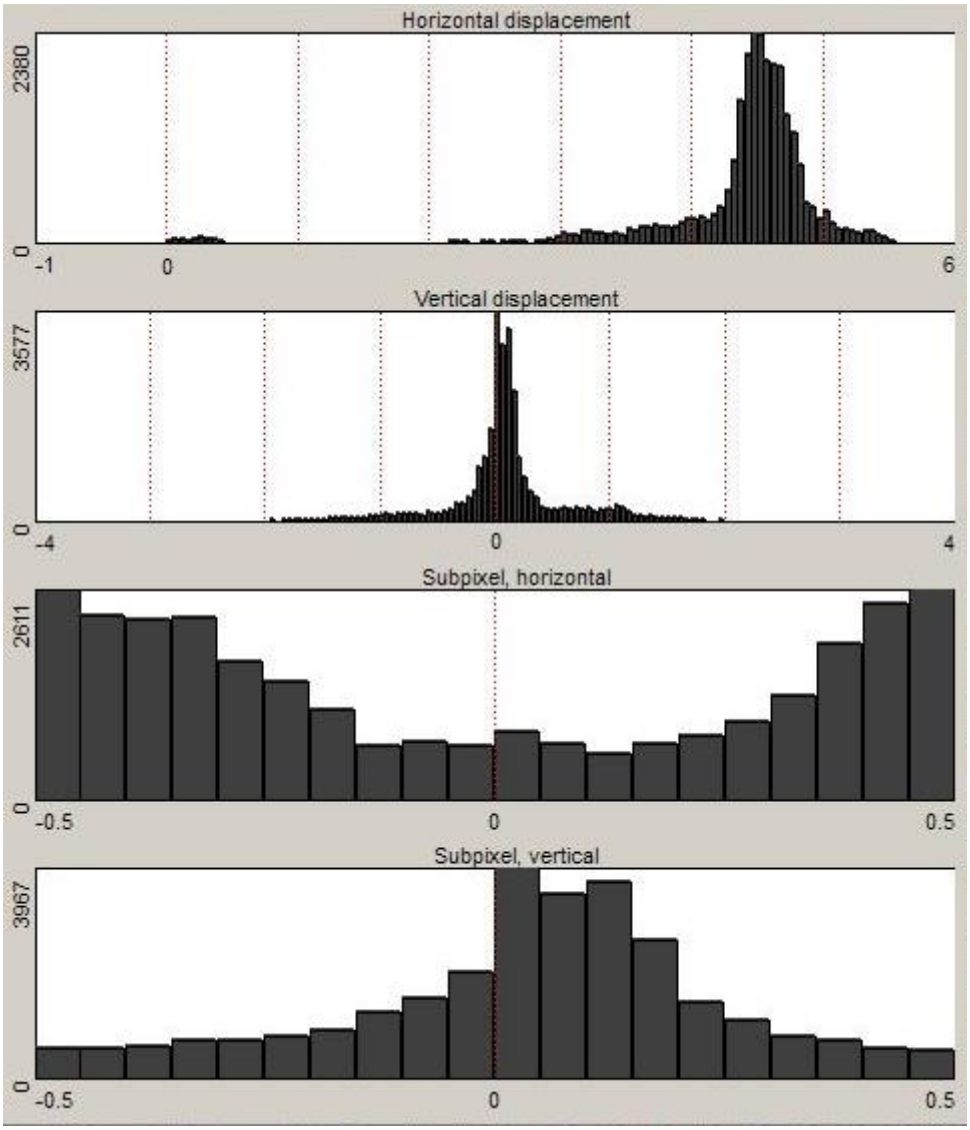

Figure 63: Measurements of pixel displacement in number of pixels and sub-pixels. Pixel displacement are measured in vertical and horizontal direction. Z=6D.

In Figure 63 there is no sign of pixel locking

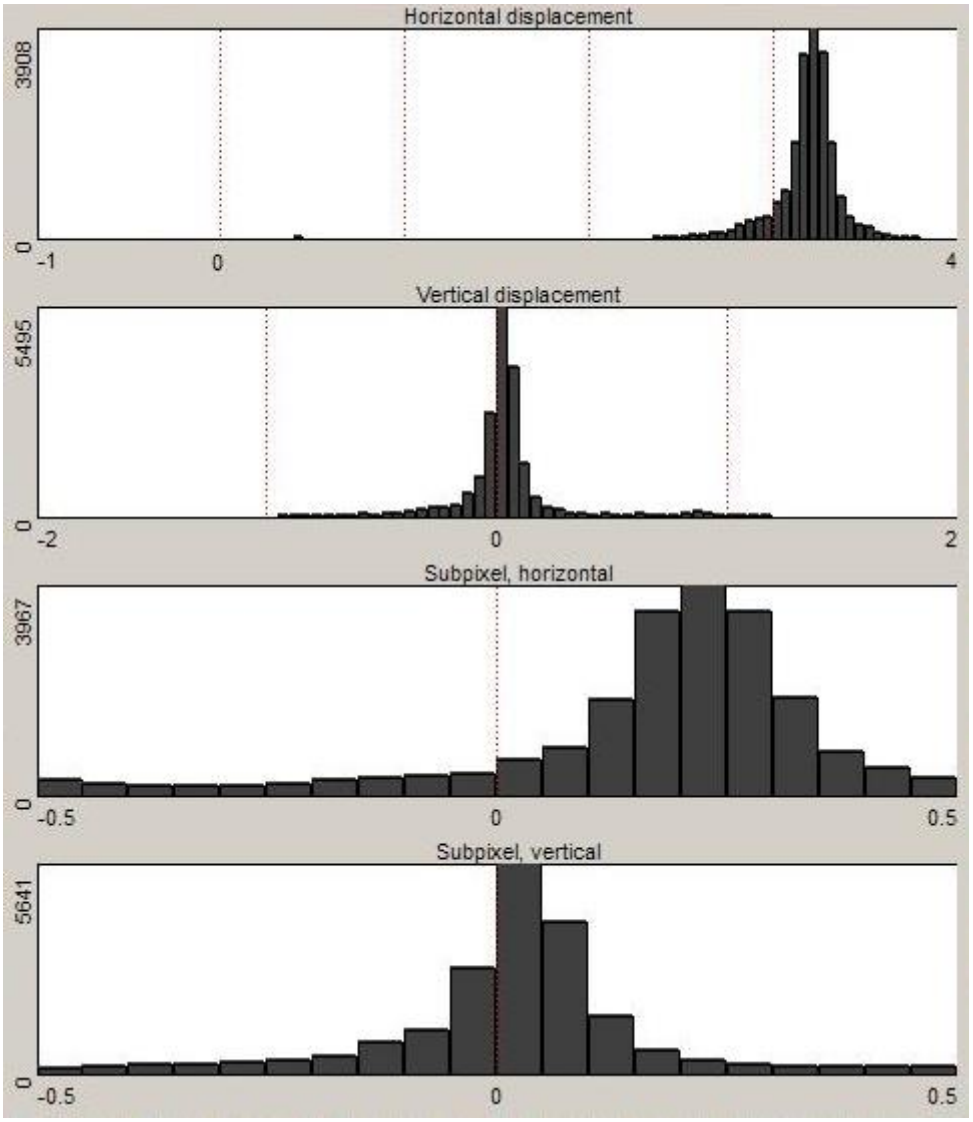

Figure 64: Measurements of pixel displacement in number of pixels and sub-pixels. Pixel displacement are measured in vertical and horizontal direction. Z=2D.

In Figure 64 there is no sign of pixel locking, since the sharp peaks observed in horizontal displacement are not locked to a single pixel displacement.

Other plots

See attached files